Prediction of Energy, Force and Response Properties of Metal Nanoclusters Using Machine Learning Techniques

Ph.D. THESIS

By

ABHISHEK OJHA

DEPARTMENT OF CHEMISTRY

INDIAN INSTITUTE OF TECHNOLOGY INDORE
DECEMBER 2024

Prediction of Energy, Force and Response Properties of Metal Nanoclusters Using Machine Learning Techniques

A THESIS

Submitted in partial fulfillment of the

requirements for the award of the degree

of

DOCTOR OF PHILOSOPHY

by

ABHISHEK OJHA

DEPARTMENT OF CHEMISTRY

INDIAN INSTITUTE OF TECHNOLOGY INDORE

DECEMBER 2024

INDIAN INSTITUTE OF TECHNOLOGY INDORE

CANDIDATE'S DECLARATION

I hereby certify that the work which is presented in the thesis entitled **PREDICTION OF ENERGY, FORCE AND RESPONSE PROPERTIES OF METAL NANOCLUSTERS USING MACHINE LEARNING TECHNIQUES** in the partial fulfilment of the requirements for the award of the degree of **DOCTOR OF PHILOSOPHY** and submitted in the **DEPARTMENT OF CHEMISTRY, Indian Institute of Technology Indore**, is an authentic record of my own work carried out during the time period from July, 2019 to December, 2024 under the supervision of Prof. SATYA S. BULUSU, Professor, Department of CHEMISTRY, Indian Institute of Technology Indore.

The matter presented in this thesis has not been submitted by me for the award of any other degree of this or any other institute.

Abhishek Ojha
11/06/25

Signature of student with date

ABHISHEK OJHA

- -

This is to certify that the above statement made by the candidate is correct to the best of my/our knowledge.

28/ 12 / 2024
Signature of Thesis Supervisor with date

Prof. SATYA S. BULUSU

- -

ABHISHEK OJHA, has successfully given his Ph.D. Oral Examination held on

Signature of Thesis Supervisor
11/06/2025
Date:

- -

Acknowledgements

First and foremost, I would like to express my sincere gratitude to my thesis supervisor, Prof. Satya S. Bulusu, for his inspiration and encouragement throughout my Ph.D. journey. His constant guidance, meticulous suggestions, and constructive criticism have been invaluable in shaping my academic growth. It has been an honor and a privilege to work under his mentorship, and I am deeply grateful for his trust and belief in me.

I extend my heartfelt thanks to my doctoral committee members, Prof. Sanjay Kumar Singh and Prof. Antony Vijesh, for their insightful suggestions, thoughtful feedback, and the time they devoted to reviewing my work. Their guidance has significantly enhanced the quality of my research. My sincere appreciation also goes to Dr. Umesh A. Kshirsagar, DPGC convener, for his unwavering support and assistance. I am immensely grateful to Prof. Arup Banerjee from RRCAT Indore for his valuable support and insightful discussions, which greatly contributed to my understanding and research progress.

I would like to acknowledge the Ministry of Education, Government of India, for providing financial support through a fellowship that enabled me to pursue this research. My deepest gratitude goes to the Head of the Department, as well as the faculty members and staff of the Department of Chemistry at the Indian Institute of Technology (IIT) Indore, for their assistance and support. I am thankful to IIT Indore for providing the computational server facilities that were integral to my research. Special thanks to my senior labmate, Dr. Shweta Jindal, for generously sharing her programming expertise, offering mentorship, and providing constant motivation, which made my initial days as a Ph.D. student much smoother. I am also grateful to Dr. Megha Sharma for her valuable discussions and insights during my research.

I sincerely appreciate my lab members—Aparna Gangwar, Ankit Patel, Harshit Verma, Habit Tatin, Amit Singh, Suvirn Upadhyay, and Ashutosh Patel for their unwavering support and cheerful cooperation. My heartfelt thanks also go to my colleagues and friends—Deepak Kumar, Alok Shukla, Mayank Singh, Vivek Singh, Justine Josh, Dilip Pandey, Rahul Yadav, Anshu Sahu, Anupma Sharma, Kulbhushan Mishra, Vikas Sahoo Ashwini Malik, Swapnesh Khade, Amit Baghel, Arpit Singh, and Sneha Shukla for their intellectual and emotional support throughout this journey. Their camaraderie and care have been a source of strength during this period. Special mention goes to my friend Vidhi Shukla for her unwavering support during some of the most challenging phases of my PhD journey.

Finally, I express my deepest gratitude to my family—my father, Mr. Subash Chandra Ojha, and my mother, Mrs. Meena Ojha—for their blessings, unconditional love, sacrifices, and constant support, which made this achievement possible. I am also deeply thankful to my brother, Vishal Gaurav, for his encouragement and for inspiring me to pursue this PhD journey. My heartfelt thanks go to my bade papa, Mr. Ramesh Chandra Ojha, and my badi mummy, Mrs. Kalindi Ojha, whose blessings and unwavering support have always guided me. I also gratefully acknowledge my brothers, Vivek Ojha and Shashank Ojha, and my sister-in-law, Shanta Devi, for their constant love, motivation, and encouragement throughout this journey.

This thesis would not have been possible without the support, guidance, and encouragement of many individuals. I am truly thankful to everyone who has been a part of this journey.

(ABHISHEK OJHA)

ABSTRACT

Calculating potential energy using density functional theory (DFT) is computationally very expensive. The complexity escalates significantly when determining the first-order derivative of energy with respect to cartesian coordinates and the second-order derivatives of the energy with respect to the external electric field, which is essential for predicting forces and polarizability in metallic nanoclusters. Since force calculations are essential for running molecular simulations, such as molecular dynamics (MD) simulations, the use of DFT-based methods becomes impractical for studying larger metallic nanoclusters. Empirical and semi-empirical methods are widely used for modeling atomic systems. However, they often lack the accuracy needed for complex systems, failing to capture intricate electronic interactions.

We develop a machine learning (ML) framework that efficiently models energy and these derivatives while maintaining high accuracy. This approach will facilitate the construction of an interatomic potential that combines the precision of DFT with the computational efficiency of empirical methods. In this thesis, we employ an artificial neural network (ANN)-based method to construct the interatomic potential, capture the complex relationships between atomic configurations, and predict the energy, forces and polarizabilities of the metal nanoclusters. In this study, the ANN interatomic potential is constructed for Ag-Pt nanoalloys. In ANN-based interatomic potential, we use higher-order invariants like Power Spectrum and Bispectrum, along with a modified atomic environment density, to describe the atomic environments. This study investigates the structural and energetic properties of Ag-Pt nanoalloys and finds that the lowest energy isomers exhibit a core-shell structure, with Pt atoms in the core and Ag atoms on the surface, while also examining the probability of Pt atoms on the surface at finite temperatures through MD trajectories. Additionally, we investigate the adsorption of CO and O_2 molecules on Ag-Pt nanoalloys using DFT and find that Pt doping enhances the adsorption strength of both molecules compared to pure Ag nanoclusters. Our results show that Pt atoms on the surface have a greater impact on adsorption than those in the core. Furthermore, our study also explores the response of gold nanoclusters to electric fields by predicting isotropic and anisotropic polarizabilities using various ML methods. We find that ANN-based models outperform Gaussian process regression and kernel ridge regression models, offering superior accuracy in polarizability predictions. This study aims to enhance the understanding of structure, dynamics and response to external fields in metal nanoclusters, facilitating the design of effective nanocatalysts and materials through accurate modeling.

Dedicated to

my family

LIST OF PUBLICATIONS

From peer-reviewed journals:

1. Structure and dynamics of 38-atom Ag-Pt nanoalloys using ANN-based interatomic potential,

   A. Ojha, Megha, S. S. Bulusu, A. Banerjee, *Comput. Theor. Chem.*, **(1220)**, 113985 (2023), **doi.org/10.1016/j.comptc.2022.113985**.

2. ANN and DFT investigation of 55-atom icosahedral Ag-Pt nanoalloys: Understanding structure, dynamics, and O_2 activation,

   A. Ojha, Megha, S. S. Bulusu, A. Banerjee, *Comput. Theor. Chem.*, **(1238)**, 114691 (2024), **doi.org/10.1016/j.comptc.2024.114691**.

3. Machine Learning Approaches for Modeling of Molecular Polarizability in Gold Nanoclusters,

   A. Ojha, S. S. Bulusu, A. Banerjee, *Artificial Intelligence Chemistry*, **(2)**, 100080 (2024), **doi.org/10.1016/j.aichem.2024.100080**.

Presentation at conferences/meetings:

1. Oral presentation on “Prediction of Ab-Initio Level Accuracy of Silver-Platinum Nanoalloys Using Machine Learning Techniques, Symposium on Materials Science Towards New Horizons-2023 organized by the Department of Chemistry, IIT Indore, in 2023.
2. Poster presentation on “Development of Computationally Efficient Machine Learning Potential for Ag-Pt Nanoalloys and Their Reaction with Small Gaseous Molecules” Abhishek Ojha, Satya S. Bulusu, Indo-German Sustainable Chemistry Conference II, Goa, organized by IIT Indore in February 2024.
3. Poster presentation on “Accelerating QM Calculations: Machine Learning Predictions of Metal Nanocluster Properties and Enhanced Adsorption in Ag-Pt Nanoalloys” Abhishek Ojha, Satya S. Bulusu, 2^{nd} Society of Physical Chemistry Symposium, 2024 (SoPhyC2024), organized by IIT Bombay in October 2024.

List of Abbreviations/Acronyms

ADF atomic density function.
ANN artificial neural network.

BH basin hopping.

CC coupled cluster.
CI configuration interaction.
CNNs convolutional neural networks.

DFPT density functional perturbation theory.
DFT density functional theory.
DOS density of states.

FCC face-centered cubic.

GEKF global extended Kalman filter.
GGA generalized gradient approximation.
GM global minimum.
GNNs graph neural networks.
GPR Gaussian process regression.

HF Hatree-Fock.
HOMO highest occupied molecular orbital.

IAP interatomic potential.
Ih icosahedral.
IR infrared.

KRR kernel ridge regression.

L-BFGS limited memory Broyden–Fletcher Goldfarb–Shanno.
LDA local density approximation.
LUMO lowest unoccupied molecular orbital.
LYP Lee–Yang–Parr.

MAE mean absolute error.
MAPE mean absolute percentage error.
MC Monte Carlo.
MD molecular dynamics.
ML machine learning.
MLP multilayer perceptron.
MOs molecular orbitals.
MSE mean square error.

NN neural network.

Oh octahedral.
ORR oxygen reduction reactions.

PAW projector augmented wave.
PBE Perdew-Burke-Ernzerho.
PDOS partial density of states.
PES potential energy surface.

RBF radial basis function.
RKHS reproducing kernel Hilbert space.
RMSE root mean square error.
RMSProp root mean square propagation.
RNNs recurrent neural networks.

SE squared errors.
SOAP smooth overlap of atomic positions.
SVM support vector machine.

TO truncated octahedron.

VAEs	Variational Autoencoders.
VASP	Vienna Ab initio Simulation Package.
VWN	Vosko-Wilk-Nusair.

Contents

List of Figures

List of Tables

Chapter 1

Introduction

1.1 Metal Nanoclusters

In recent years, nanomaterials have gained significant attention due to their versatile applications across multiple disciplines, connecting various branches of science and technology. This interdisciplinary field addresses challenges ranging from fundamental scientific understanding to practical applications [1]. Nanomaterials are characterized by structures typically less than a few hundred nanometers in size. Nanomaterials possess unique properties that differ from both atomic and bulk forms, and the properties often vary depending on size [2]. By precisely controlling the size of nanoparticles, the properties can be fine-tuned. In nanomaterials, metal nanoclusters are defined as clusters of metal atoms, typically ranging from two to a few hundred atoms (see Figure 1.1) [3, 4]. Metal nanoclusters can contain one or more types of metal atoms. Based on the number of different types of metal atoms, metal nanoclusters are classified as single-component and multi-component metal nanoclusters (nanoalloys) [3]. Metal nanoclusters have attracted particular interest for their distinctive physical and chemical properties. The properties of metal nanoclusters are influenced by various factors, including their size, shape, and composition. The unique properties of metal nanoclusters primarily arise from two factors: quantum confinement effects [5] and high surface-to-volume ratio [6, 7]. Quantum

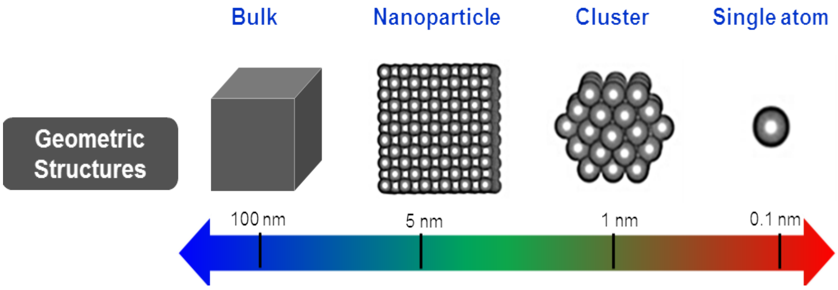

Figure 1.1: Evolution of material structures: From single atom to bulk across nanoscale dimensions.

confinement is a restriction on the motion of randomly moving electrons present in a material to specific discrete energy levels rather than to a continuum of energy bands. In bulk materials, atoms are closely packed, resulting in continuous energy bands and valence electrons behaving like a free electron gas. Due to the large size, the quantum confinement effects are negligible. However, in metal nanoclusters, these effects become significant because the clusters are small enough for electronic states to become discrete. As a result, the valence electrons no longer behave like a free electron gas and directly influence the cluster's properties. This quantum size effect creates a gap between the HOMO and LUMO levels, significantly affecting their optical, electronic, and chemical properties. Additionally, the high surface-to-volume ratio becomes more significant in smaller clusters due to the increased proportion of atoms located at the surface. As the cluster size decreases, the number of surface atoms rises relative to the total atom count, leading to a higher surface-to-volume ratio compared to larger clusters, where the majority of atoms reside in the bulk. This increased surface-to-volume ratio enhances the reactivity of the metal nanoclusters. Together, these factors contribute to the distinctive characteristics of metal nanoclusters, differentiating them from bulk materials. The unique properties of metal nanoclusters make them valuable in applications like catalysis [8–11], storage [12], nanoelectronics [4, 12] and biomedical applications [13].

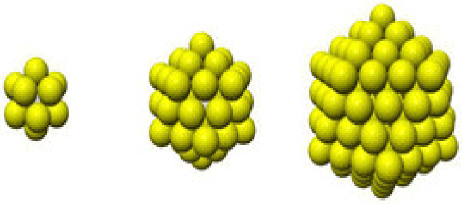

Figure 1.2: Geometrical shell-closing in icosahedral metal nanoclusters: Magic number configurations with 13, 55, and 147 atoms, respectively.

1.1.1 Stability of Metal Nanoclusters

Certain sizes of metal nanoclusters, known as magic clusters, are particularly stable due to electronic shell and atomic shell closing [14]. A closed-shell metal nanocluster refers to a cluster where both the atomic and electronic shells are closed. It has a quasispherical shape with a small surface area, making it more stable. The electronic structure follows a shell model, where the electron count corresponds to stable configurations like those in atoms (e.g., 2, 8, 18 electrons). This closed-shell configuration leads to high thermodynamic and kinetic stability [15]. Closed-shell metal nanoclusters are stable due to both atomic and electronic shell closure. Atomic shell closure [16] occurs in highly symmetrical and close-packed structures like icosahedral (Ih) and octahedral (Oh) forms, which lower surface energy and strain. Clusters with magic numbers of atoms (e.g., 13, 38, 55, 147) exhibit this geometric stability, commonly seen in structures of noble gases and metals like gold, silver or platinum (see Figure 1.2 [17]). Electronic shell closure is explained by models such as the spherical jellium and ellipsoidal jellium models, where delocalized electrons fill energy levels similar to atomic orbitals [18–20]. Clusters reaching certain electron configurations (e.g., 2, 8, 18) achieve electronic stability, making closed-shell nanoclusters thermodynamically favourable. Among all metal nanoclusters, gold nanoclusters have gained significant interest due to their unique physical and chemical properties [21]. Unlike bulk gold, which is inert due to the relativistic effect, gold nanoclusters are highly reactive and exhibit catalytic activity [22]. Gold nanocluster display a wide range of structural forms [23–27], including planar [28], cage-like [29], pyramidal [30], and amorphous core-shell structures [23, 26, 27, 31]. Gold nanoclusters exhibit remarkable electronic, chemical, and optical properties, making them highly valuable in nano-photonics and optoelectronics [32–35].

1.2 Metal Nanoalloys

In the case of multicomponent metal nanoclusters (called as nanoalloys), the properties vary with respect to size and also composition [3]. The combination of two or more noble metals leads to an enhancement of these properties. Although the use of nanoalloys was first reported in the 19^{th} century with Michael Faraday's study of optically active Au-Ag nanoparticles [36], the underlying physics and chemistry were not well understood at that time. With advancements in experimental techniques, such as spectroscopy, microscopy, and chemical analysis, alongside computational techniques like quantum mechanical methods, contemporary research has made significant progress. These approaches have enabled the exploration of the diverse compositions of nanoalloys and the influence of their chemical ordering on their properties. Nanoalloys are classified into homotops and composomers. Homotops are structures with the same composition but varied arrangements, while composomers have the same atomic composition but differ in geometry. Nanoalloys are classified based on their mixing patterns, geometric structures, and chemical ordering. The four main mixing patterns in nanoalloys are core-shell, multi-shell, subcluster segregated, and mixed nanoalloys. These are crucial for understanding and predicting the physical and chemical properties of nanoalloys. In core-shell nanoalloys, one type of atom occupies the core site, while a different type of atom is found at the surface site, forming a distinct core-shell structure. Multi-shell nanoalloys have multiple layers of alternating shells creating an onion-like structure. Subcluster-segregated nanoalloys consist of distinct groups of atoms called subclusters, made up of different elements. These subclusters may either have some degree of mixing at their interface or have only

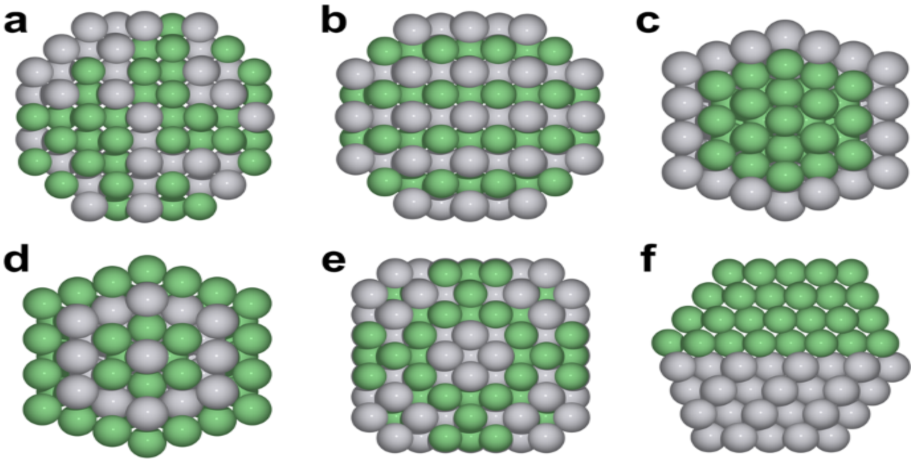

Figure 1.3: Mixing pattern of the nanoalloys.

limited bonding between the different types of atoms. Mixed nanoalloys can be either ordered or random in their atomic arrangement. In addition to these mixing patterns, nanoalloys can adopt various crystalline and non-crystalline structures. Crystalline structures have a periodic atomic arrangement with common forms including octahedra, truncated octahedra, and dodecahedra. Non-crystalline structures lack periodicity but tend to be more compact, like Ih or polyicosahedral shapes.

There are several factors that influence the structural and segregation preferences of nanoalloys. 1) Atomic sizes, where the size of the atoms plays a key role in determining their position in the nanoalloy. Smaller atoms prefer to be located in the core of the nanocluster, while larger atoms are often found at the surface. 2) Surface energy is another important factor in which atoms with lower surface energy tend to occupy the surface of the nanoalloy, as this positioning minimizes the overall energy of the system by reducing strain and maximizing stability. 3) Cohesive energy affects segregation in nanoalloys, with atoms of similar cohesive energy aggregating together, while large differences in cohesive energy lead to the separation of elements into different regions. 4) Bond strength influences the arrangement of atoms, where stronger bonds between different types of atoms encourage mixing and uniform distribution, while weaker bonds promote segregation, leading to phase separation. 5) Charge transfer affects the electronic interactions within the alloy, influencing the stability and structure of the nanoalloy as atoms adjust to balance their charge distribution. 6) Binding energy plays a significant role, with atoms that have higher binding energy being more stable in the core, contributing to the structural integrity of the cluster, while those with lower binding energy tend to occupy the surface, where they are less bound to neighboring atoms. 7) Electronic and magnetic effects significantly impact the stability and functionality of the nanoalloy. Additionally, experimental conditions and synthesis methods can impact the mixing and ordering of nanoalloys. These factors are important for determining the stability and reactivity of nanoalloys, which directly impact their potential for various applications [37]. Among the extensively studied nanoalloys, Pt-based nanoalloys have gained considerable interest due to their applications as heterogeneous catalysts in important reactions like the oxidation of CO to CO_2 [38, 39], the hydrogenation of C=O, C=C, and N=O bonds, and the dehydrogenation of C-H and N-H bonds for fuel production and the synthesis of valuable chemicals [40]. Among the most extensively studied Pt-based nanoalloys are combinations like Pt-Au [41–43], Pt-Rh [42], Pt-Cu [44], Pt-Co [42, 44], Pt-Ni [44], and Pt-Ag [45–53], each offering unique catalytic properties that make them essential in these processes.

1.2.1 Ag-Pt Nanoalloys

Among nanoalloys, Ag-Pt nanoalloys have gained significant attention in catalysis due to their distinctive properties and potential applications. Silver and platinum create a broad miscibility gap, suggesting that alloying between these metals in bulk form is unlikely [54, 55]. In Ag-Pt nanoalloys, it has been found that silver and platinum are likely to form only core-shell structures, where the core can consist of either metal depending on specific reaction conditions [47, 56, 57]. The reactivity of Ag-Pt nanoalloys is highly dependent on the structure and composition. Therefore, understanding their atomic-level geometrical and electronic structures of Ag-Pt nanoalloys is essential for gaining deeper insights into their catalytic properties.

In the last decade, the Ag-Pt nanoalloys have been the subject of numerous theoretical and experimental investigations. The structure and electronic properties of small-sized Ag_mPt_n (n = 1–7) clusters have been extensively studied using DFT [45]. For medium- to large-sized nanoalloys, studies on 13-atom $Ag_{13-n}Pt_n$ and 54-atom $Ag_{54}Pt_1$ clusters using Ih and (111) surface slab models have shown that Pt tends to occupy core positions, with increased Pt concentration leading to decreased cluster stability [46]. Studies on 55-atom $Ag_{42}Pt_{13}$ nanoalloys revealed an Ih structure, with Pt at the core and Ag on the surface [47]. Global minimum searches for 33-atom $Ag_{20}Pt_{13}$ -based nanoalloys showed that these clusters form dodecahedral core-shell structures [48]. In this context, it has been established that the alloying of Pt atoms in Ag nanoclusters increases stability and reactivity in Ag-Pt nanoalloys. Therefore, it is important to understand their structure and reactivity, particularly their interactions with gaseous molecules.

1.2.2 Adsorption of Small Gaseous Molecules

The adsorption of small gaseous molecules on metal nanoalloys is a key area of interest, particularly in catalytic applications [3, 52, 58]. Due to the high surface-to-volume ratio and unique electronic properties of nanoalloys, their surface interactions with gases are significantly enhanced compared to bulk materials. The structure and composition of the nanoalloy can influence the adsorption properties, such as the strength and selectivity of the binding. For example, in metal nanoalloys, the different metals on the surface can create distinct active sites for molecule adsorption. One metal may attract molecules more strongly, while the other metal influences the strength of the binding. This tunability makes nanoalloys highly efficient for applications like gas sensing, catalysis, and energy conversion, where selective adsorption and activation of small molecules are crucial [38, 39, 59]. In particular, the alloying of Pt atoms in large-sized nanoalloys has increased stability and reactivity. Additionally, the catalytic activity of such bimetallic nanoclusters shows selectivity in various chemical reactions. Their reactions with gaseous molecules like CO and O_2 have been thoroughly studied with the purpose of analyzing their role as nanocatalysts in CO oxidation reactions [8, 38, 39, 52, 60–63]. Significant efforts have been made to develop highly effective catalysts for removing toxic CO gas from automobile exhaust and hydrogen gases used in fuel cells [64], with a critical focus on the adsorption and activation of CO and O_2 molecules on catalytic surfaces. Size-selected Ag-Pt nanoalloys used as catalysts for the CO to CO_2 oxidation reaction have shown remarkable activity [45, 52]. Apart from the CO oxidation reaction, Ag–Pt nanoalloys have also proven effective in catalyzing the electrooxidation of methanol [65, 66], the catalytic oxidation of o-phenylenediamine by hydrogen peroxide [66], and the hydrogen evolution reaction [67].

Given the extensive applications of metal nanoclusters or nanoalloys, conducting detailed structural and geometrical analyses is important for understanding their reactivity and stability. This can be achieved by exploring the potential energy surface (PES) to find the most stable structures of metal nanoclusters. This enables the identification of stable structures of metal nanoclusters, which is essential for designing more effective nanocatalysts.

1.3 Potential Energy Surface of Metal Nanoclusters

Understanding atomic interactions is fundamental to exploring the PES for metal nanoclusters. These interactions govern how metal atoms bind, how clusters form, and how chemical reactions occur on the nanoscale [68]. A precise and comprehensive depiction of atomic interactions is essential not only for gaining insights into the properties of metal nanoclusters but also for performing reliable molecular simulations. The reflection of atomic interactions in metal nanoclusters is seen through the total energy of the nanoclusters and the atomic forces. The structural configurations of a nan-

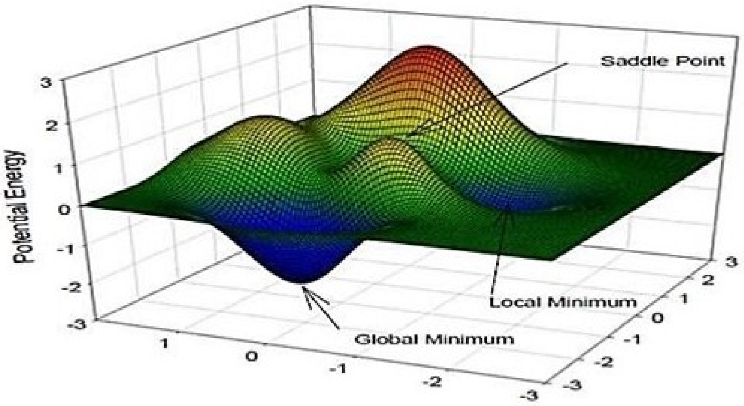

Figure 1.4: Schematic presentation of the PES of metal nanoclusters.

ocluster with a given size and composition are determined by the stability points, represented as the minima on its PES as shown in Figure 1.4. The PES is a multidimensional surface denoted as E(r), which represents the energy of a system as a function of the positions of its constituent atoms. Here, E refers to the potential energy, and r represents the atomic positions, showing how the energy changes with different atomic arrangements. For metal nanoclusters, the PES provides crucial insights for investigating their structural stability, reactivity, and dynamic properties. The global minimum on the PES corresponds to the most stable configuration, where the system achieves its lowest potential energy, representing the optimal arrangement of atoms. On the other hand, local minima represent metastable states that are energetically higher than the global minimum but may still play a significant role under specific thermodynamic or kinetic conditions. Saddle points, also known as transition states, represent the energy barriers along reaction pathways connecting different minima. These points are fundamental for understanding the mechanisms and activation energies associated with structural transformations. The search for the lowest minimum on the PES is usually known as the global optimization of the PES. In order to explore the PES, accurate energy and atomic forces are essential to get the stable structure of metal nanoclusters.

In practical cases, the potential energy is determined by the first principle method or ab initio method. It can accurately describe the interactions between atoms by solving the Schrödinger equation, which is fundamental in quantum mechanics for determining the wave function of a particle. The solution of the Schrödinger equation provides the energy for a given configuration of atoms. However, each electronic structure calculation only provides the energy for a single, specific point on the multidimensional PES. For molecular simulations such as molecular dynamics (MD) or Monte Carlo (MC) simulation, millions of such calculations have to be performed, each corresponding to a different configuration of atomic positions to explore the entire PES. This requirement poses a significant computational challenge. The ab initio methods, such as Hartree-Fock (HF) [69] and density functional theory (DFT) [70], are inherently computationally expensive. The complexity arises from the need to solve the Schrödinger equation to obtain the wave function and, subsequently, the energy for each configuration. As the size of the system increases—whether in terms of the number of atoms or electrons—the computational cost escalates rapidly. The time required for these calculations scales as the order of O(N_e^3)- O(N_e^4), where N_e is the number of electrons.

Moreover, the calculation of atomic forces adds more challenge to this because forces are obtained by taking the first derivative of energy with respect to atomic positions. Since energy calculations are already computationally intensive, determining the forces introduces even more complexity. For PES generation, force calculations are required to run MD simulations of metal nanoclusters. Therefore, to minimize computational expenses and lengthy simulations over extended time scales, it is essential to adopt a classical approach for the precise mapping of the PES of metal nanoclusters. In this context, ab initio methods may be substituted with classical or empirical methods. In classical methods, numerous functional forms have been proposed to calculate the energy and forces of metal nanoclusters. These include both semiempirical and empirical potentials. Different empirical potentials are used to model metal nanoclusters ranging from simple pairwise models like the Lennard-Jones [71] and Morse [72] potentials to more advanced many-body potentials that better describe metallic bonding, such as the Gupta potential [73]. Other widely used empirical potentials include the Murrell–Mottram potential [74], the embedded atom method (EAM) [75, 76], the Finnis–Sinclair potential [77], ReaxFF [78, 79], and force fields [80–82] have been developed. The central idea of classical force fields is the decomposition of the total energy into low-dimensional terms that represent bonding interactions. These force fields describe the potential energy of a system as a combination of bonded interactions (such as bond stretching, angle bending, and torsional rotations) and non-bonded interactions (including van der Waals and electrostatic forces). These methods rely on fixed functional forms and depend heavily on the chosen parameters. The functional forms contain a limited number of parameters which are fitted to ab initio or experimental data. Due to their fixed functional form, these methods are insufficient to accurately capture the complex PES of metal nanoclusters. Consequently, obtaining energy and force calculations for metal nanoclusters that match the accuracy of ab initio methods remains a significant challenge.

1.4 Response Properties

Besides energy calculations, it is essential to understand how metal nanoclusters respond to external stimuli, such as electric or magnetic fields. The properties of clusters with and without an external electric field differ. The interaction of metal nanoclusters with these fields defines their response properties, which include polarization, charge redistribution, and magnetic susceptibility. These properties are important for understanding the behaviour of metal nanoclusters under applied fields. One of the key response properties is molecular polarizability, which reflects how the electric dipole moment of a molecule responds to an external electric field. Specifically, polarizability represents the first-order response of the electronic charge distribution to the external electric field. It plays a fundamental role in various chemical phenomena, including electron scattering [83], electronegativity [84], and the concepts of chemical softness and hardness [85].

It also plays a crucial role in IR [86] and Raman spectroscopy [87], respectively. For example, a molecule is IR active if its dipole moment changes during vibration, while it is Raman active if its polarizability changes during the vibration [88]. Other response properties such as hyperpolarizability, which is a second-order response to an electric field. These properties are vital for second-harmonic generation spectroscopy [89] and play a key role in evaluating materials for nonlinear optical applications [90]. These spectroscopic characteristics offer valuable insights into the structural and electronic properties of metal nanoclusters [91]. Additionally, chiroptical properties constitute another category of response properties with a wide range of applications in the pharmaceutical industry [92]. These molecular attributes are critical for various applications where precise predictions of response properties are necessary for material design and functionality.

To calculate polarizability or other response properties, ab initio methods are very accurate but computationally expensive, making them best for smaller systems. On the other hand, semiempirical methods such as AM1 [93] and PM3 [94] methods are computationally inexpensive but less accurate.

To overcome the challenge of high computational cost, I am looking for new ways to keep calculations accurate while making them faster. One promising approach is using machine learning (ML), which aims to combine the accuracy of ab initio methods with the efficiency of semiempirical methods. In this thesis, I have used ML-based interatomic potential (IAP) to predict energy and its derivatives of metal nanoclusters. In this context, I have used ML to predict total energy, atomic force and polarizability for metal nanoclusters.

1.5 Machine Learning

Throughout history, humans have been inspired to create machines with human-like intelligence capable of automatically performing complex tasks.

This aspiration has come closer to reality in the past decade, marked by the rapid application of ML techniques and artificial intelligence systems across diverse fields. The integration of ML in chemistry has led to significant advancements in the field of science as a whole. By harnessing the power of data-driven models and algorithms, valuable information can be extracted from vast amounts of experimental and computational data. This enables a deeper understanding of chemical phenomena and molecular interactions. The utilization of ML techniques as IAP has garnered considerable attention because these methods effectively overcome the discussed challenges in creating PES. Several challenges must be addressed while developing IAP. 1) The accuracy of these potentials hinges on their ability to predict the energy and forces of unknown atomic configurations, closely matching reference values. 2) Additionally, the potential should be efficient enough to enable long-time MD simulations by providing faster calculations of energy and forces, in contrast to the time-consuming ab initio methods. 3) The potential must allow for the approximation of complex functions with high accuracy even if it involves a non-physical functional form. 4) Furthermore, it should be versatile enough to handle all types of bonds—covalent, ionic, and metallic—facilitating bond formation and breaking. 5) The potential should be applicable to systems of any size and dimension and their construction should be automated. 6) It is also important that analytic derivatives can be calculated easily, and there should be a systematic approach for both constructing and improving PES [95]. ML techniques are especially adept in tackling all these challenges.

As mentioned earlier, ML techniques do not rely on a fixed physical relationship between input and output. Instead, they analyze data to identify patterns that describe interactions, such as how atoms interact within a molecular system. Once trained, the ML model can predict outputs based on these learned patterns. Figure 1.5 highlights the workflow of the ML technique for constructing IAP. The process can be divided into four key components:

1)Training Data: The process begins with generating an input dataset

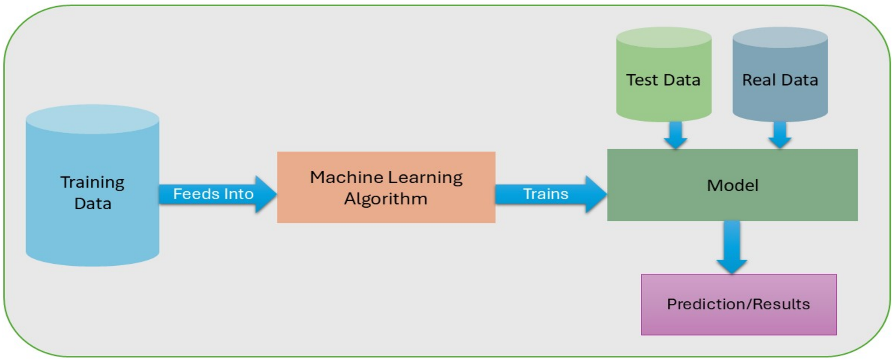

Figure 1.5: Flowchart depicting the ML model training process to predict the output.

that consists of various atomic configurations, which serve as training data. These datasets represent local atomic environments.

2) ML Algorithm: The training data feeds into the ML algorithm. The algorithm learns patterns from the input data and adjusts its parameters iteratively during training.

3) Model: Once the ML algorithm has been trained, it creates a model. The model is then validated using test data.

4) Prediction/Result: The trained model is used to make predictions. In the case of metal nanoclusters, it can predict energy, forces, or other response properties for metal nanoclusters.

The history of ML began in the 1940s when McCulloch and Pitts [96] developed a mathematical model to understand neural activity in the human brain, marking the first concept of a neural network. This foundational work laid the groundwork for applying neural networks to real-world problems. Rosenblatt's introduction of the perceptron in 1958 was one of the earliest neural network models and set the stage for subsequent developments [97]. This was followed in 1975 by Werbos's creation of the multilayer perceptron (MLP) [98]. In 1982, Hopfield introduced the Hopfield network, a recurrent neural network used for associative memory, which was influential in advancing neural network theory [99]. Quinlan introduced decision trees in 1986 [100], and shortly after, Cortes and Vapnik developed support vector machines (SVM) [101]. In 2024, John Hopfield and Geoffrey Hinton were awarded the Nobel Prize in Physics for their foundational work.

As the field evolved, ensemble techniques like AdaBoost [102] and Random Forests [103] enhanced the performance of weak learners by combining them into stronger predictors. In parallel, kernel-based methods and probabilistic models like Gaussian processes [104] and ridge regression [105] were introduced to model uncertainty in predictions. The field of deep learning, a subfield of ML that focuses on training large-scale neural networks, has expanded significantly in the last decade. convolutional neural networks (CNNs) [106], and recurrent neural networks (RNNs) [107] have been successfully applied to image classification, time-series prediction, and natural language processing. CNNs and graph neural networks (GNNs) [108] have gained popularity due to their ability to capture local chemical environments and structural patterns. Furthermore, generative models—which learn the data distribution and can generate new data instances—have become increasingly important. These include Variational Autoencoders (VAEs) [109], Generative Adversarial Networks (GANs) [110], and more recently, Diffusion Models [111]. VAEs have been used for the inverse design of molecules and crystals by encoding and decoding structural features in latent space. GANs, though more complex to train, have shown promise in generating synthetic data for underrepresented systems.

In addition to choosing the model architecture, hyperparameter optimization is essential for achieving reliable performance. Hyperparameters were tuned manually and through trial-and-error to find the best performing values. These include learning rate, batch size, number of hidden layers, activation functions, and dropout rate. Model parameters are tuned using optimization algorithms that reduce the error between predicted and actual values by adjusting weights. Common methods include L-BFGS [112], Kalman Filter [113], Levenberg–Marquardt [114], backpropagation [115], gradient descent [116], and the widely used Adam optimizer [117]. These methods update weights step by step until the error becomes small enough. Once optimized, the model can make accurate predictions on new data.

Training stability and generalization were improved through techniques such as early stopping, dropout regularization, and cross-validation. Where applicable, data augmentation and noise-injection were used to enhance model robustness, particularly in the low-data regime.

1.5.1 Neural Network Model

In recent decades, ML methods have become increasingly prominent in constructing the PES and predicting the response properties. Among these, neural network (NN)-based techniques have emerged particularly effective, demonstrating their ability to model highly non-linear problems. One of the earliest NN-based PES models was introduced by Sumpter and Noid in 1992 [118]. A significant advancement in this field came with the work of Behler and Parrinello, who proposed a general approach to construct the PES [95, 119, 120]. They modelled the total energy as a sum of atomic contributions, using element-specific atomic neural networks with atom-centred symmetry function descriptors as inputs. This method was further extended by Artrith et al. to incorporate long-range electrostatic interactions [121]. In recent years, the field has advanced with the adoption of deep neural network architectures, where the construction of invariant representations is integrated into the model and optimized during training. Notable examples of this include the deep tensor neural networks [122] and SchNet models [123] developed by the Tkatchenko and Müller group, as well as the deep potential molecular dynamics model by Zhang et al. [124]. Many neural network potentials have been developed using diverse architectures, including message-passing neural networks [125], graph neural networks [126], and graph convolutional networks [127].

While NNs are the primary focus, kernel-based methods also offer a compelling alternative for constructing PES [128, 129]. These methods leverage various atomic descriptors, such as Coulomb Matrices [130], Bag of Bonds [131], Histograms of Distances Angles and Dihedrals [132], Faber–Christensen–Huang–von Lilienfeld [133], and smooth overlap of atomic positions (SOAP) [134]. Kernel methods, such as Gaussian processes [135], which utilize a Bayesian or probabilistic approach, and the reproducing kernel Hilbert space (RKHS) method, which employs polynomials as support functions, have been thoroughly studied in the literature [136, 137]. Like the Behler-Parrinello atomic neural networks [95], the Gaussian approximation potentials developed by Bartók et al. [138] decompose the total energy into a sum of atomic energies. These atomic contributions are modelled using Gaussian process regression, employing a squared exponential kernel function. In addition to neural network and kernel-based methods, other interpolation and representation techniques for PES construction are also widely utilized. These include modified Shepard interpolation [139], interpolating moving least-squares [140–142], and permutationally invariant polynomial [143]. These alternative methods provide diverse and complementary strategies for constructing accurate and reliable PES.

Despite the growing interest in ML, significantly fewer studies have concentrated using ML methods for molecular response properties such as dipole moment [144–147], polarizability [148, 149], and hyperpolarizability [150, 151]. These properties present a greater challenge for learning due to their multiple coordinate-dependent components, which change in a covariant manner when the system undergoes rotation. Recent advancements in ML for response properties have focused on approaches that respect the rotational symmetry of tensorial properties. For instance, Grisafi and their colleagues introduced covariant kernels in kernel-based regression to preserve this symmetry [152, 153], while Christensen et al. applied response operators directly to kernel functions to mimic the tensorial response to electric fields [154]. Although traditional neural networks often disrupt covariant symmetry due to their nonlinearity, specialized models like symmetry-adapted regression have proven effective [152, 155]. These models have been successfully applied to various tasks, such as predicting properties like dipole moment [147], polarizability [148] and Raman spectra [156], highlighting the growing potential of ML in accurately modeling complex tensorial properties.

The way in which the structures of metal nanoclusters or nanoalloys influence their physicochemical properties is quite intriguing. Among these properties, catalytic and electrical properties are particularly important due to their relevance in technological applications. Metal nanocluster is highly size-dependent, making it a challenging and fascinating topic, especially when considering the interplay between energetic, thermodynamic, and dynamic effects in these clusters. ML methods provide an effective way to tackle these challenges by accurately predicting properties and uncovering structure-property relationships.

1.6 Objective of the Thesis

1. To predict the energy and its first-order derivatives (forces) by constructing the PES of Ag-Pt nanoalloys using an ANN-based IAP while designing an IAP that is both computationally efficient and scalable for accurate simulations.
2. To investigate the adsorption activation of small gas molecules, such as CO and O_2, on Ag-Pt nanoalloys. This study aims to provide insights into the reactivity of CO and O_2 on Ag-Pt nanoalloys in the context of the CO oxidation reaction.
3. Developing machine learning models to predict the second-order derivatives of energy with respect to the electric field (polarizability) of gold nanoclusters.

1.7 Organization of the Thesis

- **Chapter 1. Introduction:**

  The first chapter begins with an introduction to metal nanoclusters, emphasizing their stability, unique properties, and diverse applications. This is followed by a discussion on the stability and physicochemical properties of metal nanoalloys, with a special focus on Ag-Pt nanoalloys and their potential for catalytic and advanced applications. The chapter also explores the adsorption of small gaseous molecules in these systems, providing insight into their reactivity. Additionally, it addresses the construction of PES for metal nanoclusters, highlighting the challenges and limitations associated with accurately modeling their complex energy landscapes. A section is dedicated to the introduction of ML techniques, particularly neural networks, showcasing their advantages in constructing PES and response properties. Finally, the chapter outlines the objectives and organization of the thesis, setting the foundation for subsequent discussions.

- **Chapter 2. Theoretical Methodology:** The second chapter provides an overview of the theoretical foundations underlying this thesis. It begins with a brief introduction to ab initio methods used to generate data for the ANN model, including the basics of the DFT-based approach. The chapter then introduces empirical potentials, which provide simplified models for atomic interactions based on parameterized equations, followed by an in-depth discussion of ANN. The application of ANN in constructing the PES of nanoclusters is thoroughly examined, with a focus on the ANN architecture and the calculations for energy and force. Following this, weight optimization methodologies are discussed, including the global extended Kalman filter (GEKF), which is used to optimize ANN weights for accurate predictions of energy and force. The chapter then continues with a discussion on the techniques used for exploring the PES, focusing on MD simulations. I then discuss the input to the ANN, where I utilize a descriptor function that incorporates both radial and angular atomic environments. The angular environment is represented using power spectrum and bispectrum-based functions, which are derived from the modeling of the atomic density function to accurately capture the atomic surroundings. Additionally, the chapter covers the theory and mathematical formulation of polarizability, including isotropic polarizability (α_{iso}) and anisotropy in polarizability ($\Delta\alpha$).

- **Chapter 3. Structure and Dynamics of Ag-Pt Nanoalloys:** In this chapter, I have predicted the energy and its first-order derivative with respect to cartesian coordinates (force) by constructing a PES for Ag-Pt nanoalloys using an ANN model. Using ANN-based interatomic potential, I systematically carried out structural and energetic analysis of $Ag_{38-n}Pt_n$ (n = 1 - 8) nanoalloys. I performed MD simulations and global optimizations to search the global minimum structures and investigate the effect of temperature on the structures of Ag-Pt nanoalloys. I found that the lowest energy isomers of $Ag_{38-n}Pt_n$ nanoalloys are a core-shell structure in which the Pt atoms occupy the core region while the Ag atoms are located in the surface region. Furthermore, the probability of the presence of a Pt atom on the surface sites in $Ag_{38-n}Pt_n$ nanoalloys has been calculated at finite temperatures. I found that at 360K, at least one Pt atom moves from the core to the surface region of the $Ag_{38-n}Pt_n$ nanoalloys, which may serve as the reactive sites for the reactions to occur.
- **Chapter 4. Small Gaseous Molecules Adsorption on Ag-Pt Nanoalloys:** In this chapter, ANN-based interatomic potential has been constructed to examine the structural properties of 55-atom Ih Ag-Pt nanoalloys. I conducted an MD simulation to find the minimum energy isomers of $Ag_{55-n}Pt_n$ nanoalloys, where n= 0-14. Additionally, I studied the adsorption of O_2 and CO molecules on $Ag_{55-n}Pt_n$ nanoalloys using the first-principles based DFT method. The presence of Pt doping has been found to increase the adsorption strength of O_2 and CO on the $Ag_{55-n}Pt_n$ nanoalloys compared to the pure Ag_{55} nanocluster. Our investigation suggests that the presence of Pt atoms in the core of the nanoalloy has a relatively minor effect on the adsorption of O_2 and CO in comparison to Pt atoms present

on the surface. The adsorption of O_2 and CO on $Ag_{41}Pt_{14}$ nanoalloy, in which one of the Pt atoms is present at the surface of the nanoalloy, shows strongest adsorption among all the compositions of $Ag_{55-n}Pt_n$ nanoalloys.

- **Chapter 5. Prediction of Polarizability of Gold Nanocluster:** In this chapter, I have predicted the second-order energy derivative with respect to the electric field using ML models. Specifically, I investigated the isotropic polarizability (α_{iso}) and anisotropy in polarizability ($\Delta\alpha$) of gold nanoclusters with various ML algorithms. Our approach utilized high-order invariant descriptors based on spherical harmonics integrated with ML models such as ANN, Gaussian process regression (GPR), and kernel ridge regression (KRR). The ANN models, enhanced with bispectrum and power spectrum descriptors, showed superior predictive performance, with the global extended Kalman filter (GEKF) optimizer outperforming the Adam optimizer across multiple metrics. The validation of ANN weights against a local minimum structure of gold nanoclusters confirmed the model's accuracy in predicting polarizabilities, with outcomes closely resembling those obtained from DFT. These findings highlight the effectiveness of ML in accurately predicting second-order energy derivatives with respect to the electric field (polarizability) of gold nanoclusters, with ANN-based models outperforming other ML models.
- **Chapter 6. Conclusion and Future Scope:** The last chapter of the thesis includes the major findings of our results and the possible future scope of the current research work.

.

Chapter 2

Theoretical Methodology

2.1 Quantum Mechanical Methods

In quantum mechanical methods, it is often convenient to separate the motions of the atomic nuclei and the electrons. This is achieved using the Born-Oppenheimer (BO) approximation [157], which assumes that the nuclei are much heavier and move much slower than the electrons. As a result, the electronic wave function can be solved independently for fixed nuclear positions, while the nuclear motion is treated separately. This approximation simplifies the Schrödinger equation and forms the basis for many quantum mechanical methods used in electronic structure calculations. In quantum mechanics, the stationary states of atomic systems can be described by the wave function (ψ). The wave function provides a complete picture of the physical system, which depends on both the electronic coordinates ($\vec{r}$) and the nuclear coordinates ($\vec{R}$). To determine the wave function, it must be calculated at each spatial point $\vec{r}$ within the region of interest, which involves the solution of the Schrödinger equation. When focusing on stationary electronic states, the time-independent form of the Schrödinger equation is expressed as:

$$(\widehat{T} + \widehat{V})\psi(\vec{r}, \vec{R}) = \widehat{E}(R)\psi(\vec{r}, \vec{R}), \tag{2.1}$$

where $\widehat{T}$ is the kinetic energy operator, $\widehat{V}$ is the potential energy operator, and $\widehat{E}(R)$ represents the energy eigenvalue that may depend on the nuclear coordinates $\vec{R}$. According to the BO approximation, the total wave function $\psi(\vec{r}, \vec{R})$ is treated as a product of the electronic and nuclear wave functions, and the Schrödinger equation is solved for the electronic degrees of freedom while treating the nuclear positions as fixed. The equation for the total Hamiltonian acting on the wave function is given by:

$$\widehat{H}\psi(\vec{r}; \vec{R}) = \widehat{E}(R)\psi(\vec{r}; \vec{R}) \tag{2.2}$$

In atomic systems which involve multiple electrons and nuclei, rather than a single-electron model, a many-body wave function is defined $\psi(\vec{r}, \vec{R})$, which depends on the positions of all electrons and nuclei in the system.

$$\psi(\vec{r}, \vec{R}) = \psi(r_1, r_2, r_3 ...., r_N; R_1, R_2, R_3, ...R_A) \tag{2.3}$$

In this context, $r_1, r_2, r_3 ...., r_N$ are the coordinates of the N electrons and $R_1, R_2, R_3, ...R_A$ are the coordinates of the A nuclei within the system. Therefore, there are three types of coulombic interactions: (i) the repulsion between nuclei, (ii) the repulsion between electron-electrons, and (iii) the attraction between the nucleus and electrons. Thus, for a system consisting of electrons and nuclei, the potential energy terms ($\widehat{V} = \widehat{V_{ee}} + \widehat{V_{nn}} + \widehat{V_{ne}}$) in the Schrödinger equation can be expressed mathematically as:

$$V_{ee} = \sum_{i}^{N_e}\sum_{j}^{N_e} \frac{e^2}{4\pi\epsilon_0|r_i - r_j|} \tag{2.4}$$

$$V_{nn} = \sum_{A}^{N_n}\sum_{B}^{N_n} \frac{Z_A Z_B e^2}{4\pi\epsilon_0|R_A - R_B|} \tag{2.5}$$

$$V_{ne} = \sum_{A}^{N_n}\sum_{i}^{N_e} - \frac{Z_A e^2}{4\pi\epsilon_0|r_i - R_A|} \tag{2.6}$$

and the kinetic energy term ($\widehat{T} = \widehat{T_e} + \widehat{T_n}$) is

$$= -\sum_{i}^{N_e} \frac{\hbar}{2m_e}\nabla_i^2 - \sum_{A}^{N_n} \frac{\hbar}{2M_A}\nabla_A^2 \tag{2.7}$$

where M_A and m_e are the mass of the nucleus and electrons, respectively. Z_A and e are charges of the nucleus and electrons, respectively. $|R_A - R_B|$ is the internuclear distance, $|r_i - R_A|$ is the distance between the nucleus and electron and $|r_i - r_j|$ is the distance between electrons. Therefore, the Hamiltonian operator can be written as the sum of the kinetic energy operator$(\widehat{T})$ and the potential energy operator $(\widehat{V})$ of the given system:

$$\Bigg(-\sum_{i}^{N_e} \frac{\hbar}{2m_e}\nabla_i^2 - \sum_{A}^{N_n} \frac{\hbar}{2M_A}\nabla_A^2 + \sum_{A}^{N_n}\sum_{B}^{N_n} \frac{Z_A Z_B e^2}{4\pi\epsilon_0|R_A - R_B|} + \sum_{i}^{N_e}\sum_{j}^{N_e} \frac{e^2}{4\pi\epsilon_0|r_i - r_j|} - \sum_{A}^{N_n}\sum_{i}^{N_e} \frac{Z_A e^2}{4\pi\epsilon_0|r_i - R_A|} \Bigg)\psi(r,R) = E\psi(r,R) \tag{2.8}$$

Due to the significant mass difference between the nucleus and the electron (BO approximation), the positions of the nuclei can be considered fixed. Hence, the kinetic energy of the nuclei can be neglected, and their potential energy can be treated as constant. Therefore, only the electronic component needs to be solved in the Schrödinger equation. Consequently, Eq. 2.8 simplifies to the following in atomic units:

$$(-\sum_{i}^{N_e} \frac{\nabla_i^2}{2} + \sum_{i}^{N_e}\sum_{j}^{N_e} \frac{1}{|r_i - r_j|} - \sum_{A}^{N_n}\sum_{i}^{N_e} \frac{Z_A}{|r_i - R_A|})\psi_e \quad = \quad E\psi_e \tag{2.9}$$

An exact solution to the Schrödinger equation is unattainable for multi-electron systems because of the inter-electronic repulsion term. Solving Eq. 2.9 is a challenging task, and simplifications are often required. The electronic Hamiltonian depends only on the spatial coordinates of the electron. However, to describe an electron completely, it is necessary to specify its spin. Therefore, approximation methods such as Hartree-Fock (HF) ensure that the wave function follows the antisymmetry principle using a Slater determinant. However, HF still treats electron-electron interactions in a mean-field manner, neglecting electron correlation. The HF equation for $i = 1, 2, .., N$ electrons is given as:

$$f_i\phi_i = \epsilon_i\phi_i \tag{2.10}$$

where ϕ_i are spatial orbitals and the Lagrangian multipliers ϵ_i are the eigenvalues of the Fock operator f_i. The ϵ_i has the physical interpretation of orbital energies. The f_i is an effective one-electron operator of i^{th} electron given by:

$$f_i = -\frac{1}{2}\nabla_i^2 - \sum_{A}^{N_n} \frac{Z_A}{|r_i - R_A|} + V_{\text{HF}}(i) \tag{2.11}$$

In Eq. 2.11 the first two terms are the kinetic energy and the potential energy due to the electron-nucleus attraction. $V_{HF}(i)$ is the HF potential which is the average repulsive potential experienced by the i^{th} electron due to the remaining $N-1$ electrons. It is expressed as:

$$V_{HF}(i) = \sum_{j}^{N} (J_j(i) - K_j(i)) \tag{2.12}$$

where J_j is the coulomb operator and K_j is the exchange operator. As previously discussed, the HF approximation describes the system using a single Slater determinant. This simplification, however, fails to capture the intricate interactions between electrons, which are especially important in processes such as bond formation and bond breaking. While the HF method provides a useful starting point for understanding electronic systems, its inherent limitations arise from the neglect of electron correlation. However, correlation effects play a crucial role in many systems of interest, and thus, it becomes necessary to go beyond the HF approximation to achieve a more accurate description. To overcome the limitations of the HF method, two important approaches are Configuration Interaction (CI) and Coupled Cluster (CC) methods. However, these methods still face challenges in computational efficiency and scalability for larger systems. To address these limitations and include correlation effects, the many-body problem can be mapped onto an effective single-particle framework. DFT effectively captures electron correlation, providing an accurate method for describing electronic systems. A brief overview of DFT is provided in the next section, and all electronic structure calculations in this work are performed using DFT.

2.1.1 Density Functional Theory

The foundation of the DFT was laid by Hohenberg and Kohn, who demonstrated [70] that electron density can be treated as the fundamental variable in place of the wavefunction for treating many-electron systems quantum mechanically. In principle, the total energy can be expressed as a functional of the electron density. The ground-state density can be determined by finding the minimum of a total energy functional with respect to the density, which is shown in the following form:

$$E[n(r)] = T[n(\mathbf{r})] + V_{ee}[n(\mathbf{r})] + V_{ne}[n(\mathbf{r})] \tag{2.13}$$

where $T[n(\mathbf{r})]$, $V_{ee}[n(\mathbf{r})]$ and $V_{ne}[n(\mathbf{r})]$, representing the kinetic energy, electron-electron repulsion energy, and interaction energy of the electron density with the external potential, respectively. The above energy expression can be divided into two parts: one that depends on the specific system, such as the potential energy from the attraction between nuclei and electrons, and another that is universal and remains the same regardless of the number of electrons (N_e), the positions of the nuclei (R_A), or their charges (Z_A). The system-independent components are grouped into a new term called the Hohenberg-Kohn functional, $F_{HK}[n(\mathbf{r})]$ shown as:

$$F_{HK}[n(\mathbf{r})] = T[n(\mathbf{r})] + V_{ee}[n(\mathbf{r})] \tag{2.14}$$

The functional $F_{HK}[n(\mathbf{r})]$ is the holy grail of DFT. If it were known exactly, it would allow us to solve the Schrödinger equation, not just approximately but exactly. The explicit form of both these functionals as the functional of density is not known. However, it is possible to further decompose the $T[n(\mathbf{r})]$ and ($V_{ee}[n(\mathbf{r})]$) into meaningful parts. The electron-electron repulsion, $V_{ee}[n(\mathbf{r})]$ is typically divided into two parts: the classical Coulomb contribution, $E_H[n(r)]$, and the non-classical component, $E_{ncl}[n(r)]$. The non-classical term accounts for effects such as self-interaction correction, exchange, and Coulomb correlation. Kohn and Sham introduced the concept of decomposition of the kinetic energy into a non-interacting and interacting system. The exact expression of the non-interacting kinetic energy T_s is derived from a set of N non-interacting occupied orbitals expressed as:

$$T_s[n(\mathbf{r})] = -\sum_{i=1}^{N} \frac{1}{2} \langle \psi_i | \nabla^2 | \psi_i \rangle \tag{2.15}$$

By introducing the decompose form of $T[n(\mathbf{r})]$ and $V_{ee}[n(\mathbf{r})]$ the Eq. 2.13 can be reformulated as

$$E[n(\mathbf{r})] = T_s[n(\mathbf{r})] + V_{ne}[n(\mathbf{r})] + E_H[n(\mathbf{r})] + E_{\mathrm{xc}}[n(\mathbf{r})] \tag{2.16}$$

In Eq. 2.16 the last term $E_{\mathrm{xc}}[n(\mathbf{r})]$ is referred to as the exchange-correlation energy functional, which can be written as:

$$E_{\mathrm{xc}}[n(\mathbf{r})] = (T[n(\mathbf{r})] - T_s[n(\mathbf{r})]) + (V_{ee}[n(\mathbf{r})] - E_H[n(\mathbf{r})]) \tag{2.17}$$

Now, on applying the variational principle to minimize the total ground-state energy, subject to the constraint that the orbitals are orthonormal $(<\psi_i \psi_j>= \delta_{ij})$. The resulting Schrodinger equation using the Kohn-Sham approach is expressed as:

$$\left(\frac{-\nabla^2}{2} + v_{\mathrm{KS}}[n(\mathbf{r})] \right) \psi_i(\mathbf{r}) = \epsilon_i \psi_i(\mathbf{r}) \tag{2.18}$$

$$v_{\mathrm{KS}}(\mathbf{r}) = v_{\mathrm{ext}}(n(\mathbf{r})) + \int \frac{n(\mathbf{r})}{|r_i - r_j|} d^3 r + v_{xc} \tag{2.19}$$

Therefore, the density is obtained by summing the squared of the Kohn Sham orbitals ψ exactly equals the ground state density of our real target system of interacting electrons.

$$n(\mathbf{r}) = \sum_{i}^{N_e} |\psi_i|^2 \tag{2.20}$$

In DFT, the exchange-correlation energy combines the residual kinetic energy and non-classical electrostatic interactions between electrons. This energy is described by the exchange-correlation functional, which contains all unknown factors related to electron-electron interactions. While Kohn-Sham DFT is exact in principle, the approximation arises when defining an explicit form for the exchange-correlation functional.

2.1.2 Exchange-Correlation Functionals

There are several methods for calculating the exchange-correlation energy E_{xc} within DFT. The simplest method is the local density approximation (LDA) [158, 159], where the exchange-correlation functional at each spatial point is approximated by the value for a homogeneous electron gas:

$$E_{\mathrm{xc}}[n(\mathbf{r})] = \int \epsilon_{\mathrm{xc}}(n)\, n(\mathbf{r})\, d^3r + E_{\mathrm{c}}^{\mathrm{LDA}}[n(\mathbf{r})] \tag{2.21}$$

An improvement over LDA is the generalized gradient approximation (GGA) [160, 161], which accounts for the gradient of the electron density in the functional. This allows for a more accurate description of the exchange-correlation energy by considering variations in the electron density:

$$E_{\mathrm{xc}}[n(\mathbf{r})] = \int \epsilon_{\mathrm{xc}}^{\mathrm{GGA}}(n(\mathbf{r}), \nabla_{\mathbf{r}} n(\mathbf{r})), d^3r \tag{2.22}$$

Here, $\epsilon_{\mathrm{xc}}^{\mathrm{GGA}}$ is the exchange-correlation potential, which depends on both the density $n(\mathbf{r})$ and its gradient $\nabla_{\mathbf{r}} n(\mathbf{r})$. One of the most commonly used GGA functionals is the Perdew-Burke-Ernzerhof (PBE) [160] functional. The PBE functional refines the exchange-correlation energy by introducing additional terms derived from physical constraints and principles of the uniform electron gas. The PBE functional is particularly effective for metallic systems and has been validated in numerous studies, showing good agreement with experimental data. Its selection is based on the need for a reliable and computationally efficient method to describe the electron exchange-correlation in the systems under study. A further refinement to GGA is the meta-GGA, which improves accuracy by incorporating higher-order derivatives of the density. However, the improvement from GGA to meta-GGA is typically smaller than the gain achieved by moving from LDA to GGA.

The major advancement in DFT came with the introduction of hybrid functionals, which combine a fraction of the HF exchange energy with the DFT exchange-correlation functional. One of the most successful and widely used hybrid functionals is B3LYP [162, 163], which includes Becke's three-parameter exchange functional and the Lee–Yang–Parr (LYP) correlation functional:

$$E_{\mathrm{xc}}^{\mathrm{B3LYP}} = aE_{\mathrm{x}}^{\mathrm{HF}} + (1-a)E_{\mathrm{x}}^{\mathrm{LDA}} + bE_{\mathrm{x}}^{\mathrm{B88}} + cE_{\mathrm{c}}^{\mathrm{LYP}} + (1-c)E_{\mathrm{c}}^{\mathrm{VWN}} \tag{2.23}$$

where $a = 0.20$, $b = 0.72$, and $c = 0.81$ are empirically derived parameters, and $E_{\mathrm{x}}^{\mathrm{B88}}$ and $E_{\mathrm{c}}^{\mathrm{VWN}}$ are the Becke88 exchange functional (GGA) and the Vosko-Wilk-Nusair (VWN) local spin density approximation to the correlation functional, respectively. These parameters were optimized by fitting to the experimental G1 dataset [164].

2.1.3 Basis Sets

The concept of one-electron wave functions, i.e., molecular orbitals (MOs), lies at the core of all electronic structure theories. However, the exact functional form of MOs is unknown, so electronic structure calculations rely on linear combinations of known functions to represent these unknown MOs. These known functions are referred to as basis functions and a set of them forms a basis set [165]. The basic idea behind selecting an appropriate function is that it should accurately represent the system's physical properties and facilitate the straightforward calculation of the integrals involved in the method. The minimal necessary functions for a given atom form a minimal basis set. For hydrogen and helium, a single s-function suffices; for first-row elements, two s-functions and one set of p-functions are required; for second-row elements, three s-functions and two sets of p-functions form a minimal basis set. Basis sets that use multiples of these functions are termed double-zeta (DZ), triple-zeta (TZ), and quadruple-zeta (QZ), depending on whether they include two, three, or four times as many functions as the minimal set. The LANL2DZ basis set, widely used for heavy elements, incorporates an effective core potential for core electrons, reducing computational cost while providing a double-zeta description for valence electrons.

In this study, I use two different basis sets to generate data for predicting the energy, force, and polarizability of metal nanoclusters. For energy and force calculations, utilize the plane-wave basis set within the VASP package [166–169], where electron orbitals are represented by plane waves, and the full electron wave function is efficiently treated using the Projector Augmented-Wave (PAW) [170] method. use the PBE [160] functional within the GGA for accurate approximations of metallic clusters. However, for polarizability calculations, I use the LANL2DZ [171] basis set with the B3LYP [162, 163] functional in the Gaussian 09 [172] package.

2.2 Empirical Potentials

Empirical potentials are simplified mathematical models used to describe interactions between atoms in an N-atom system. They approximate the potential energy of a system using predefined mathematical functions. However, their accuracy is constrained by their reliance on parametrization, which is typically derived from atomic experimental data. Empirical potentials often represent the total energy of a system as a sum of contributions from individual atomic interactions as shown in the following Eq. 2.24:

$$E = \sum_{i}^{N} V(\mathbf{z_i}) \tag{2.24}$$

where

$$\mathbf{z_i} = \{\mathrm{r_{ij}} \mid j \in \text{neighbors of } i\}.$$

Here, E represents the total energy of the N-atom system, and $V(\mathbf{z_i})$ denotes the potential energy contribution from each atom i. Here, $\mathbf{z_i}$ represents the atomic environment of the i^{th} atom, where each $\mathrm{r_{ij}}$ corresponds to the vector from the i^{th} atom to the j^{th} atom in its immediate vicinity. This neighbourhood is used to calculate the interaction energies in empirical potential methods, which depend on the relative distances and configurations between atoms. Some of the most commonly used empirical potentials are pair potentials, three-body potentials, and many-body potentials.

Pair potential: Pair potentials inherently account for only two-body interactions, meaning the total energy of a configuration can be expressed as the sum of all two-body contributions.

$$E = \sum_{i} \sum_{j>i} \varphi(r_i, r_j) \tag{2.25}$$

where the function $\varphi(r_i, r_j)$ is called a pairwise potential. For example, Lenard-Jones's potential [71], Morse's potential [72], etc. It is important to note that Lennard-Jones and Morse potentials can also be used as non-local potentials. However, they are commonly applied with a cutoff radius to account for the screening of interatomic interactions, which typically makes them local in practice.

Three body potential: Three-body potentials take into account interactions involving three bodies:

$$E = \sum_{i} \sum_{j>i} \varphi(r_i, r_j) + \sum_{i} \sum_{j \neq i} \sum_{k \neq i} P(r_i, r_j, r_k). \tag{2.26}$$

These potentials include the Tersoff [173] and Stillinger-Weber [174] models. While two-body terms are often related to bond lengths, three-body terms are typically associated with the angles between bonds.

Many-body potential: Many-body potentials capture the complexity of atomic interactions by considering the simultaneous effects of multiple atoms, unlike pair potentials that focus only on two-atom interactions. This approach provides a more accurate depiction of complex interactions within materials, particularly when an atom's behaviour is significantly influenced by its surrounding neighbours in a non-trivial manner. For example, Gupta potential [73], EAM potential [75, 76], etc.

The Gupta potential is a widely used many-body potential designed to model the interactions between atoms in metallic systems, particularly transition metals. It is generally expressed as the sum of two components: a repulsive term and an attractive many-body term. The equation is written as:

$$E_{\text{total}} = \sum_i \left(\sum_{j \neq i} A \exp\left(-p \left(\frac{r_{ij}}{r_0} - 1 \right) \right) - \sqrt{\sum_{j \neq i} \xi^2 \exp\left(-2q \left(\frac{r_{ij}}{r_0} - 1 \right) \right)} \right) \tag{2.27}$$

The Gupta potential is derived from the tight-binding model [175, 176], where the system's total energy includes a repulsive term dependent on interatomic distances and an attractive term that accounts for many-body interactions. The attractive component is often represented as a function of the combined interactions between an atom and all its neighbours, highlighting the collective nature of metallic bonding. In this study, the Gupta potential is used to generate an initial dataset for constructing the PES for Ag-Pt nanoalloys.

2.3 Machine Learning Potential

ML-based potentials are a type of many-body IAP used in atomistic simulations. Unlike traditional potentials, which rely on an approximate representation of physical atomic interactions, ML potentials take a different approach. Rather than using fixed analytical functions, ML potentials aim to learn the underlying patterns of atomic bonding and interactions from data. This learning-based approach allows the potential to model complex relationships between atomic configurations and their contributions to the system's energy. By capturing these patterns, ML potentials offer a more flexible and accurate method for representing interatomic interactions without relying solely on predefined energy contributions.

ML includes different ways of learning. One common approach is supervised learning, where the goal is to create a model f that connects input values (features) x_i with their corresponding outputs (targets) y_i in a dataset $\{(x_i, y_i)\}_{i=1}^{N}$. Here, N represents the number of observations. When the output values y_i are linked to classes, this process is known as a classification problem. Different ML algorithms, such as SVM [101], can be employed to address classification problems.

Regression is another widely used form of supervised learning, where the objective is to fit the inputs to a continuous function. Generally, in an ML method, if x represents input features or independent variables and y denotes the target or dependent variable, then the objective is to find an optimal function (f_x^*) that minimizes the expected loss, denoted as $\mathbf{E}[L]$,

$$f_x^* = \underset{f_x}{\arg\min}\, \mathbf{E}[L] = \underset{f_x}{\arg\min}\, \frac{1}{N} \sum_{i=1}^{N} L(y_i^{\text{target}}, f(x_i)) \tag{2.28}$$

where N represents the number of data points and y_i^{target} denotes the target values corresponding to the input feature vector x_i. A common choice of loss function is a squared loss function given by

$$\mathbf{E}[L] = \sum_{i=1}^{N} (y_i^{target} - f(x_i))^2 \tag{2.29}$$

In ML methods, the loss function is represented as

$$E(a) = \frac{1}{N} (y_i^{target} - f(x_i, a))^2 \tag{2.30}$$

where a represents weight parameters. I can minimize the expected loss function by choosing the a for which $E(a)$ is as small as possible. In this work, I have used regression algorithms, specifically an artificial neural network (ANN), to predict the energy, forces, and response properties of metal nanoclusters.

2.3.1 Artificial Neural Network

ANN refers to a branch of artificial intelligence that takes inspiration from the brain's structure. These networks are computational models that mimic the structure and organization of biological neural networks. They function similarly to how the human brain is organized. Just like the interconnected neurons in the brain, ANNs consist of nodes (or neurons) that are interconnected across different layers shown in Figure 2.1. The artificial neuron is the basic unit of an ANN. It works in three simple steps: multiplication, addition, and activation. First, each input is multiplied by a weight. Then, all these weighted inputs are added together along with a bias value. Finally, the result goes through an activation function, which introduces non-linearity and determines the neuron's output, which is expressed below in Eq. 2.31

$$y = f\left(\sum_{i=1}^{n} a_i x_i + b\right) \tag{2.31}$$

The activation function plays an important role in how an artificial neuron processes information. For example, non-linear functions like the sigmoid are used to introduce the necessary non-linearity into the network, allowing it to learn complex patterns. The sigmoid function is defined as:

$$f(x) = \frac{1}{1 + e^{-x}} \tag{2.32}$$

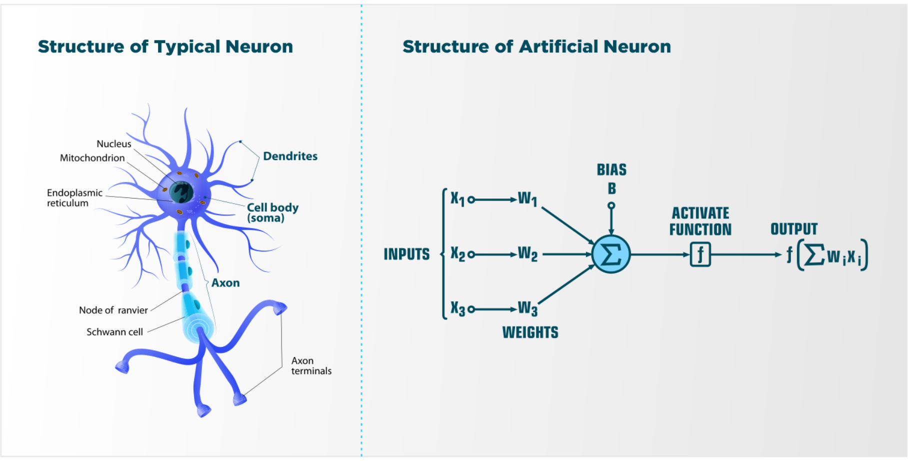

Figure 2.1: Human brain and artificial neural network.

In ANN, the weight parameters (a) are adjusted during the training phase to reduce the discrepancy between predicted and actual outputs. This optimization process is essential for enhancing the ML model's performance, as it significantly influences both the accuracy and generalization of the model.

For constructing the PES of metal nanoclusters, ANN predict energy and force from atomic environments. ANN is especially useful when the connection between input and output isn't clear, as it learns this connection by adjusting the parameters. The number of parameters depends on the complexity of the system. In our case, the energy of a nanocluster depends on the positions of its atoms. A single-layer neural network can establish a relationship between atomic positions and energy. However, this network has limitations when it comes to handling structural transformations such as translations and rotations. In these cases, even though the positions of the atoms change, the overall energy of the system remains the same, causing the network to struggle with accurate predictions. To address this, interatomic distances are invariant to translation and rotation and are used as inputs. This improves the model's ability to predict energy, but using only interatomic distances doesn't capture the relative arrangement of atoms. To overcome this, the interatomic distances within a cutoff radius are summed to create a density around each atom, which is then weighted by a Gaussian function. This representation allows the ANN to learn more complex relationships between atomic configurations and energy. To further improve the model, a second hidden layer is added to capture more detailed features of the atomic density, following the approach proposed by Behler and Parrinello [95, 177]. This two-hidden-layer neural network provides a more accurate representation of the PES, helping to predict energy and forces with precision.

In this work, I used an ANN architecture to create the IAP. Our network has an input layer with descriptor functions, two hidden layers with neurons, and an output layer with a single neuron that gives the energy value of an atom. So the network is as follows,

$$E_N = \sum_{m=1}^{Hn_2} a_{m1}^{23} \cdot f_m^2 \left[b_m^2 + \sum_{j=1}^{Hn_1} a_{jm}^{12} \cdot f_j^1 \left(b_j^1 + \sum_{k=1}^{input} a_{kj}^{01} \cdot G_{N,k}^{\mu} \right) \right] \tag{2.33}$$

In this Eq. 2.33, the input function $G_{N,k}^{\mu}$ contains the input coefficient for the N^{th} atom. a_{kj}^{01}, a_{jm}^{12} and a_{m1}^{23} are weights connected to the input layer with the first hidden layer, the first hidden layer connected to the second hidden layer, and the second hidden layer to the output layer, respectively. Hn_1 and Hn_2 are the hidden layers. The bias weights for the first and second hidden layers are represented by b_j^1 and b_m^2, respectively. To make the network's output nonlinear, sigmoid functions (f_j^1 and f_m^2) are applied to the output of the first and second hidden layers, respectively.

The network is built for each atom of the cluster, and the total energy ($E_{cluster}$) of the cluster is obtained by summing up all the atomic energies E_N,

$$E_{\text{cluster}} = \sum_{N=1}^{natoms} E_N \tag{2.34}$$

Furthermore, in accordance with our primary aim to obtain PES using ANN, I calculated the force acting on the system by using the following expression for the α^{th} component ($\alpha = x, y, z$) of the force in terms of the derivative of energy with respect to the input descriptor:

$$F_\alpha = -\frac{\partial E'_{cluster}}{\partial \alpha} = -\sum_{N=1}^{natoms} \frac{\partial E'_N}{\partial \alpha} = -\sum_{N=1}^{natoms} \sum_{k=1}^{input} \frac{\partial E'_N}{\partial G^{\mu}_{N,k}} \left(\frac{\partial G^{\mu}_{N,k}}{\partial \alpha} \right) \tag{2.35}$$

2.3.2 Weights Optimization Methods

The ML models are trained by optimizing the weights to reduce the error between the predicted and actual outputs. Optimization techniques for adjusting weights in ML models are typically classified into two categories: first-order and second-order methods. First-order methods, such as gradient descent [116], backpropagation [115], and Adam [117], utilize the gradient of the loss function concerning the weights to implement incremental updates. These methods are typically more straightforward. Conversely, second-order methods, including the quasi-Newton method [178], Kalman filter [113], etc, consider the curvature of the loss function by employing second-order derivatives (Hessian matrix), which can lead to faster convergence but involve greater computational demands. The selection of an optimization technique is contingent upon the specific needs of the task, including dataset size and model complexity. In this work, I utilized two optimization techniques, Adam and the Global Extended Kalman Filter (GEKF), to update the weights and improve the model's efficiency.

2.3.2.1 Adam Optimization

Adam is a highly efficient optimization algorithm for gradient descent, particularly effective when dealing with large-scale problems involving vast amounts of data or numerous parameters [117]. It requires less memory compared to other methods and achieves efficient convergence. Adam combines two well-known gradient descent techniques: momentum [179] and root mean square propagation (RMSProp) [180].

The momentum method accelerates gradient descent by using an exponentially weighted average of past gradients, allowing faster convergence towards minima. The method for updating the weights is

$$a_{t+1} = a_t - \alpha m_t \tag{2.36}$$

where m_t is the moving average of gradients:

$$m_t = \beta m_{t-1} + (1-\beta)\left[\frac{\partial L}{\partial a_t}\right] \tag{2.37}$$

RMSProp is an adaptive algorithm that uses an exponential moving average of squared gradients to adjust the learning rate, improving upon AdaGrad. The weights are updated according to the following expression:

$$a_{t+1} = a_t - \frac{\alpha}{\sqrt{v_t + \epsilon}}\frac{\partial L}{\partial a_t} \tag{2.38}$$

where v_t represents the moving average of squared gradients, which can be expressed as:

$$v_t = \beta v_{t-1} + (1-\beta)\left[\frac{\partial L}{\partial a_t}\right]^2 \tag{2.39}$$

Adam combines the strengths of Momentum and RMSProp, controlling oscillations and ensuring large enough steps to avoid local minima.

The Adam update rule uses bias-corrected estimates for momentum (m_t) and RMSProp (v_t):

$$\hat{m}_t = \frac{m_t}{1-\beta_1^t}, \quad \hat{v}_t = \frac{v_t}{1-\beta_2^t} \tag{2.40}$$

The final updated weight in the Adam optimizer is calculated using the following Eq. 2.41:

$$a_{t+1} = a_t - \frac{\alpha \hat{m}_t}{\sqrt{\hat{v}_t + \epsilon}} \tag{2.41}$$

where ϵ is a small constant to avoid division by zero, $\beta_1 = 0.9$, $\beta_2 = 0.999$, and $\alpha = 0.001$. In the present study, the Adam optimizer is taken from PyTorch ML library [181] to optimize the weight parameters.

2.3.2.2 Global Extended Kalman Filter Optimization

GEKF is a non-linear second-order optimization method [23, 113]. The key advantage of the GEKF compared to other algorithms is its fast and reliable optimization capabilities. This is because it minimizes the error for each data point independently and converges faster than other methods. In this study, we employ the GEKF method to optimize the ANN weights. In GEKF method, the weights ($\vec{a}_{t+1}$) are updated from the previous weights ($\vec{a}_t$). This process requires the Kalman gain matrix (K_G) and the error vector ($\vec{E}$). The error vector represents the difference between the actual output and the predicted value, which is calculated using the old weights in ANN. The updated weights estimation has been calculated using Eq. 2.42

$$\vec{a}_{t+1} = \vec{a}_t + (K_G \times \vec{E}) \tag{2.42}$$

For energy and force prediction, the error vector ($\vec{E}$) comprises one energy ($E_{DFT}^{cluster} - E_{ANN}^{cluster}$) and 3N force component vector ($F_\alpha^{DFT} - F_\alpha^{ANN}$) of the data points of DFT and ANN. Hence, the dimension of the error vector is 3N+1. Where K_G is Kalman gain, which can be taken by the Kalman filter equation,

$$K_G = \lambda_n^{-1} \left[\frac{P_o \cdot H^T}{\lambda_n^{-1}(H \cdot P_o \cdot H^T) + R} \right] \tag{2.43}$$

where

$$\lambda_n = \lambda_o \times \lambda_{ini} + (1 - \lambda_o) \tag{2.44}$$

Here λ_n is a forgetting function which is used to prevent the weights from getting trapped in a local minimum. In this work, I use λ_o and λ_{ini} are initialized as 0.99 and 0.97, respectively. Hessian matrix (H) is the derivative of the error vector with respect to each weight. For the update of weights in each step, the Kalman filter uses the error covariance matrix of weights (P_{new}), which contains information on the direction of previous updates of weights. The P_o matrix is initialized as an identity matrix (I). The error covariance matrix gets updated at every step $(P_o = P_{new})$ by using Eq. 2.45

$$P_{new} = \lambda_n^{-1}[(I - K_G \cdot H)P_o] + Q \tag{2.45}$$

The step-by-step explanation of the GEKF process is expressed below:

Initialization: I initialized the ANN weights with random values, also defined the process noise (Q) and the measurement noise covariance (R), and initialized the error covariance matrix (P_o). In this study, Q is set to 0.000001, R to 0.2, and the initial P_o value to 50.

First evaluation: Using the initial random weights, compute the total energy and the 3N force components for the first reference point in the dataset. Then, calculate the error vector $(\vec{E})$.

Kalman gain: Determine the Kalman gain matrix (K_G) by utilizing the H matrix and the initial error covariance matrix (P_o).

Weight update: Finally, update the weight vector according to Eq. 2.42.

This approach allows for the simultaneous prediction of energy and forces using an ANN with minimal error and high accuracy.

2.4 Other ML Models

In this study, I have used additional ML models, including GPR and KRR, along with ANN. GPR provides probabilistic predictions with uncertainty estimates, which are useful for capturing complex patterns. KRR uses the kernel trick to effectively model non-linear relationships. Together, these models offer a flexible and interpretable approach for analyzing and predicting.

2.4.1 Gaussian Process Regression

The GPR model is a supervised ML technique that adopts a probabilistic approach to interpret data, functioning on a non-parametric basis [104]. It is a stochastic process where every finite subset of its collection of random variables has a multivariate normal distribution. That is to say, for an index set X, a real-valued stochastic process $\{f(x), x \in X\}$ is a Gaussian process if, for any subset $x = (x_1, \ldots, x_n) \in X$, $f(x)$ has a joint Gaussian distribution. It is then completely described by its mean function m and its covariance function k.

$$f \sim \mathcal{N}\left(m(x), K(x, x')\right) \tag{2.46}$$

Where $K(x, x')$ is the covariance matrix with entries $K_{i,j} = k(x_i, x'_j)$. In other words, a Gaussian process can be understood as a multivariate Gaussian distribution with an uncountably infinite number of random variables. The mean function m can be any real-valued function, and it is often set to zero by subtracting the mean from the data. The kernel function k can be any valid kernel. Thus, a Gaussian process is often written as:

$$f(x) \sim \mathcal{GP}\left(m(x), k(x, x')\right) \tag{2.47}$$

To sample functions from the Gaussian process, I simply need to define the mean and covariance functions. The covariance function k models the joint variability of the Gaussian process random variables, returning the modeled covariance between each pair of inputs. In other words, with f and f^* representing the training and test outputs, respectively, I have the following joint distribution:

$$\begin{bmatrix} f \\ f^* \end{bmatrix} \sim \mathcal{N}\left(0, \begin{bmatrix} K(X,X) & K(X,X^*) \\ K(X^*,X) & K(X^*,X^*) \end{bmatrix}\right) \tag{2.48}$$

As I have seen, the specification of this covariance function, the kernel function, implies a distribution over functions. By choosing a specific kernel function it is possible to set prior information on this distribution. I can sample function evaluations of a function drawn from a Gaussian process at a finite but arbitrary set of points. Using the properties of Gaussian processes, I can evaluate the posterior by conditioning the joint Gaussian prior distribution on the observation:

$$\begin{aligned}(f^* \mid X^*, X, f) \sim \mathcal{N}\big(K(X^*,X)K(X,X)^{-1}f,\ K(X^*,X^*) \\ - K(X^*,X)K(X,X)^{-1}K(X,X^*)\big).\end{aligned} \tag{2.49}$$

In the GPR model, I use the squared exponential kernel, also known as the radial basis function (RBF) kernel [182] for its effectiveness in modeling smooth and continuous functions.

$$K_{\mathrm{RBF}}(x,x') = \exp\left(-\frac{\|x-x'\|^2}{2l^2}\right) \tag{2.50}$$

2.4.2 Kernel Ridge Regression

KRR integrates ridge regression (linear least squares with L2-norm regularization) with the kernel trick [105]. This allows it to learn a linear function in the feature space defined by the chosen kernel. When non-linear kernels are used, KRR effectively models a non-linear function in the original input space. KRR model minimizes a loss function composed of two terms: a residual error term and a regularization term. Given a dataset $\{(x_i, y_i)\}_{i=1}^N$, where $x_i \in \mathbb{R}^d$ are the input features and $y_i \in \mathbb{R}$ are the target values, the objective of KRR is to find a function $f(x)$ that minimizes the following cost function:

$$E(L) = \sum_{i=1}^{N} (y_i - f(x_i))^2 + \lambda \|f\|_{\mathcal{H}}^2 \tag{2.51}$$

where:

- $\|f\|_{\mathcal{H}}^2$ represents the norm of the function f in a RKHS method,
- $\lambda > 0$ is the regularization parameter that controls the trade-off between the fit to the data and the complexity of the model.

Using the representer theorem [183], the solution $f(x)$ can be expressed as a linear combination of kernel functions:

$$f(x) = \sum_{i=1}^{N} \alpha_i K(x, x_i), \tag{2.52}$$

where $K(x, x_i)$ is a positive semi-definite kernel function that computes the similarity between x and x_i, and α_i are the coefficients to be learned. By substituting $f(x)$ into the cost function and solving for $\boldsymbol{\alpha} = [\alpha_1, \alpha_2, \ldots, \alpha_N]^T$, the following closed-form solution is obtained:

$$\boldsymbol{\alpha} = (\mathbf{K} + \lambda \mathbf{I})^{-1} \mathbf{y}, \tag{2.53}$$

where $\mathbf{K}$ is the kernel matrix with entries $K_{ij} = K(x_i, x_j)$, $\mathbf{I}$ is the identity matrix, and $\mathbf{y} = [y_1, y_2, \ldots, y_N]^T$ is the vector of target values. In this work, I use the RBF kernel from Eq. 2.50. Once it $\boldsymbol{\alpha}$ is computed, predictions for a new data point x_{new} can be made as:

$$f(x_{\text{new}}) = \sum_{i=1}^{N} \alpha_i K(x_{\text{new}}, x_i). \tag{2.54}$$

2.5 Atomic Descriptor Function

The atomic descriptor function plays a crucial role in the accurate representation of an atom's local environment within nanoclusters. In ML models applied to molecular systems, this descriptor must be carefully designed to ensure that the atom's local environment is captured in a manner that is invariant to specific transformations. In particular, these functions must satisfy the properties of translational, rotational, and permutational invariance to ensure that the atomic interactions are represented consistently, irrespective of their orientation or order within the nanocluster [120].

Translational invariance ensures that the descriptor function remains unaffected by the overall position of the nanocluster in space. This is critical as the position of the nanocluster relative to an arbitrary origin has no physical relevance for its intrinsic properties, such as dipole moments or interaction energies. Similarly, rotational invariance ensures that the descriptor function is independent of the cluster's orientation in space. Whether the nanocluster is rotated or remains in its original orientation, the symmetry function produces the same result, allowing the model to capture the true physical interactions between atoms without being misled by extrinsic factors like molecular orientation. The third key requirement, permutational invariance, ensures that the function is indifferent to the ordering of atoms within the nanocluster. For example, if two atoms of the same element switch positions in the atomic structure, the descriptor function will produce identical results. This is particularly important when dealing with metallic systems like gold, silver or platinum nanoclusters, where multiple atoms of the same type may be present in symmetric configurations.

By ensuring invariance to these transformations, symmetric descriptor functions guarantee that each atomic environment is uniquely mapped, meaning that identical local atomic environments will always yield the same descriptor. This uniqueness is essential for neural network to correctly identify and learn the complex relationships between atomic configurations and properties such as molecular dipole moments. Furthermore, the descriptor function captures the structural equivalence between atomic environments, ensuring that symmetrically equivalent configurations are treated as identical, thus preventing redundant or conflicting information from entering the model. These descriptor functions serve as input to the ANN model to predict energies, forces or polarizabilities. The number of descriptors must be sufficient to provide a complete representation of the atomic environment. If too few descriptors are used, the representation may lack important details, while an excess of descriptors can lead to redundancy. To select the optimal number of descriptors, it is essential to combine a thorough understanding of the atomic system with iterative testing. This process ensures that the chosen descriptors effectively capture the atomic environment without being too sparse or redundant. Once the optimal descriptors are identified, it is important that the number of descriptors for each atom remains consistent across the entire system. This consistency is necessary to maintain the correct dimensionality throughout the neural network model, allowing for accurate predictions of energy, forces, and polarizabilities. In this work, I utilized a descriptor function that incorporates both the radial and angular environments of an atom. For the angular environment, I used power spectrum and bispectrum-based functions to accurately depict the atomic environments.

2.5.1 Radial Descriptor Function

Radial descriptor functions are the two body functions which incorporate the radial distribution in the environment around an atom. For each i^{th} atom, the function is expressed as a sum of Gaussian functions with varying decay rates ε, depending on the distance r_{ij} between the i^{th} and j^{th} atoms (see Eq. 2.55). These functions explore various regions up to a specified cutoff radius, ensuring a smooth transition in interactions as atoms near or far away from this cutoff radius.

$$Q^i_{rad} = \sum_{j \neq i} e^{-\varepsilon r_{ij}^2} f_c(r_{ij}). \tag{2.55}$$

Where the cut-off function $f_c(r_{ij})$ is,

$$f_c(r_{ij}) = \frac{1}{2}\left[\cos\left(\frac{\pi r_{ij}}{r_c} + 1\right)\right]. \tag{2.56}$$

Here r_c is the cutoff radius, its value is chosen to be 8Å in accordance with our previous studies [134, 177, 184, 185]. The hyperparameter ε used in this study is listed in Table 2.1, which controls the width of the multiplied Gaussian function as well as the decay of its tail portion. The number and distribution of these parameters are finalized through a trial-and-error process. Various sets of ε values are tested by performing neural network prediction for energy and force. The prediction errors are then analyzed to determine the optimal number of parameters. In this work, I use nine different values of ε from Table 2.1 to produce nine radial functions by employing Eq. 2.55

Table 2.1: Values of ε parameter

.

$\varepsilon(\AA^{-2})$	0.005	0.015	0.0230	0.038	0.060	0.090	0.150	0.260	0.480

Radial functions alone don't capture atomic movement at fixed interatomic distances; additional functions are needed to describe the angular positioning of atoms relative to each other. In this study, I use higher-order invariants angular functions derived from atomic density modelled by spherical harmonics.

2.5.2 Atomic Density Function

The atomic density function (ADF) serves as a key descriptor that accounts for the local environment of each atom in the cluster. It is represented as a sum of delta functions centred on neighbouring atoms.

$$\rho^i(\mathbf{r}) = \sum_{j\neq i} \delta(\mathbf{r} - \mathbf{r_{ij}}), \tag{2.57}$$

The density can be represented as an expansion using spherical harmonics $\mathrm{Y}_{lm}(\theta, \phi)$, which serve as an orthonormal basis for L_2 functions defined on the unit sphere, which is shown in Eq. 2.58

$$\rho(\hat{\mathbf{r}}) = \sum \delta(\hat{\mathbf{r}} - \hat{\mathbf{r}}_{\mathbf{ij}}) = \sum_{l=0}^{\infty} \sum_{m=-l}^{l} c_{lm} Y_{lm}(\hat{\mathbf{r_{ij}}}) \tag{2.58}$$

From Eq. 2.58, it indicates that radial information is completely omitted from the density projection, as r_{ij} is not directly factored into the calculation of atomic density. To address this, a factor is incorporated into the delta function expansion to reflect the actual positions of the atoms within a certain cut-off distance. The modified ADF is defined as follows:

$$\rho^i(\mathbf{r}) = \sum_{j \neq i} e^{-\eta r_{ij}^2} \delta(\mathbf{r} - \mathbf{r_{ij}}) f_c(r_{ij}), \tag{2.59}$$

Where the vector $\mathbf{r_{ij}} = \mathbf{r_i} - \mathbf{r_j}$ and its magnitude r_{ij} represent the distance between the i^{th} atom and the j^{th} atom in its vicinity within a certain range defined by the cut-off function $(f_c(r_{ij}))$. In the above Eq. 2.59, the parameter η modulates the width of the Gaussian function. The factor η accounts for varying distances from the central atom. The hyperparameter η are used in this study are listed in Table 2.2

Table 2.2: Values of η parameter

$\eta(\mathring{A}^{-2})$	0.0028	0.0040	0.0110	0.028	0.059

The spherical harmonic coefficient c^i_{lm} is obtained by the inner product of Y_{lm} with the ADF $\rho(\hat{\mathbf{r}})$, and it is given as:

$$c^i_{lm} = \sum_{j \neq i} Y^*_{lm}(\hat{\mathbf{r_{ij}}}) e^{-\eta r_{ij}^2} f_c(r_{ij}). \tag{2.60}$$

The coefficient c^i_{lm} contains all the information about the ADF for atom i. The ADF is represented by spherical harmonics coefficients c^i_{lm}, which describe the amplitude and phase of the atomic environment at a specific frequency l and m. Since the spherical harmonics expansion is infinite, it is truncated at a specific l value. This value is chosen by fitting the model to minimize errors in predictions.

Power Spectrum : A descriptor that exhibits both rotational and permutational invariance can be constructed from the coefficients c^i_{lm} as a power spectrum. This power spectrum serves as a second-order invariant descriptor for atomic environments, ensuring consistency under rotations and permutations. For the i^{th} atom, it can be expressed as follows:

$$D^{i}_{ang,PS,l} = \frac{4\pi}{2l+1} \sum_{m=-l}^{l} (c^{i}_{lm})^{*} c^{i}_{lm}, \tag{2.61}$$

In this study, l ranges from 0 to 9, and η is set to 5 (as shown in Table 2.2), resulting in 50 angular coefficients per atom. This power spectrum function captures the angular information of the local atomic environment surrounding the i^{th} atom.

Bispectrum : In the power spectrum [134, 177], which is a second-order invariant descriptor, can effectively capture an atomic environment, but some information may be lost when Fourier modes are treated independently. In this thesis, the present study explores the use of the third-order invariant bispectrum [186, 187] to address this limitation in representing the atomic environment with the power spectrum.

The bispectrum is obtained through the Fourier transform of the triple correlation function [188], thereby incorporating the coupling of information between two frequencies (l_1, l_2) as depicted in Eq. 2.62:

$$B^{i}_{ll_1l_2} = \sum_{m=-l}^{l} \sum_{m_1=-l_1}^{l_1} \sum_{m_2=-l_2}^{l_2} {c^{i}_{lm}}^{*} C^{ll_1l_2}_{mm_1m_2} c^{i}_{l_1m_1} c^{i}_{l_2m_2}, \tag{2.62}$$

where $C^{ll_1l_2}_{mm_1m_2}$ represent the Clebsch Gordon coefficients. The phase coupling between two frequencies (l_1, l_2) provides additional information compared to independent frequency (l). To construct the bispectrum, the coefficient l ranges from $|l_1 - l_2|$ to $|l_1 + l_2|$ and the sum of these coefficients (l, l_1, l_2) must be an even number. Maintaining $m_1 + m_2 = m$ such that Clebsch Gordon coefficients do not equal to zero. Hence, with increasing values of l_1 and l_2, the calculation of the bispectrum becomes more complex due to the expanding number of potential combinations for l,l_1, and l_2. I present a solution by calculating the bicoherence [186, 189], a normalised

Table 2.3: Possible combination of l, l_1 and l_2 for l_1 max =4, l_2 max = 4.

ll_1l_2	ll_1l_2	ll_1l_2	ll_1l_2	ll_1l_2
000	121	222	624	534
101	312	422	033	734
202	213	123	233	044
303	413	323	433	244
404	314	523	633	444
011	514	242	134	644
211	022	424	343	844

form of bispectrum, to evaluate the frequencies with correlated information:

$$D^i_{ang,BS,ll_1l_2} = \sqrt{\frac{(B^i_{ll_1l_2})^2}{D^i_{l_1}.D^i_{l_2}.D^i_l}}. \tag{2.63}$$

In our case, I employ Eqs. 2.62 and 2.63 and explored a range for l_1, l_2 spanning from 0 to 4, while l varying from $|l_1$ - $l_2|$ to $|l_1$ + $l_2|$. This exploration yielded a total of 35 combinations representing distinct values for l, l_1 and l_2 as outlined in Table 2.3. Subsequently, I selected the top 15 combinations per atom with a bicoherence range of 0.4 to 1.0, extracting 15 bispectrum coefficients. Therefore, these extracted coefficients are adequate for describing complex atomic environments.

2.5.3 Descriptor for the Nanoalloys

The modeling of the atomic density is distinct for nanoalloy systems, primarily due to the presence of two different metal atoms. In nanoalloys, the interaction and arrangement of these different metal atoms lead to unique atomic environments and bonding characteristics that differ with the neighboring atoms. To effectively incorporate this effect into the ADF, I utilized a bond-specific weighting factor ϑ_{ij} for each pair of ith and jth atoms. This weighting factor is defined as $\vartheta_{ij} = e^{\mu_{ij}/m_\beta}$, following the methodology briefly described in the recent works of Bulusu and co-workers [184]. By implementing this approach, I am able to account for the influence of distinct atomic interactions within the nanoalloy system. The weighted atomic density can be written for nanoalloy systems as follows:

$$\rho^i_{NA}(\mathbf{r}) = \sum_{j \neq i} \vartheta_{ij} e^{-\eta r_{ij}^2} \delta(r - r_{ij}) f_c(r_{ij}), \tag{2.64}$$

Hence, the weighted radial function for nanoalloys is written as:

$$Q^i_{rad} = \sum_{j \neq i} \vartheta_{ij} e^{-\varepsilon r_{ij}^2} f_c(r_{ij}). \tag{2.65}$$

The parameter μ_{ij} appearing in the exponential is the reduced mass given by $\frac{m_i \times m_j}{m_i + m_j}$, where m_i and m_j are the atomic masses of ith and jth atoms, respectively. The parameter m_β represents the atomic mass of an atom whose function is being calculated.

In Eq. 2.64, $\rho_i^{NA}(r)$ represents the weighted atomic density at position r around atom i. The summation runs over all atoms j except i. The factor $e^{-\eta r_{ij}^2}$ is a Gaussian function controlling the spatial spread of the atomic density based on the interatomic distance r_{ij}. The function $\delta(r - r_{ij})$ is the Dirac delta function, which selects contributions exactly at distance r_{ij}. Finally, $f_c(r_{ij})$ is a cutoff function that smoothly reduces contributions from atoms beyond a certain distance to ensure locality. In Eq. 2.65, ε represent the parameter controls the decay rate of the radial function with distance. To accurately model the forces in nanoalloy systems, it is essential to address the complexities introduced by their multi-component nature. The weighted atomic density function and weighted radial function have been employed to calculate the energy for nanoalloys. However, this method introduces an undesired scaling of forces due to the bond-specific weighting, complicating the neural network's ability to converge on a global minimum for the weights. To address this issue, the forces are modelled separately from the previously calculated energy, ensuring more accurate force predictions. The schematic diagram illustrating this approach is presented in Figure 2.2.

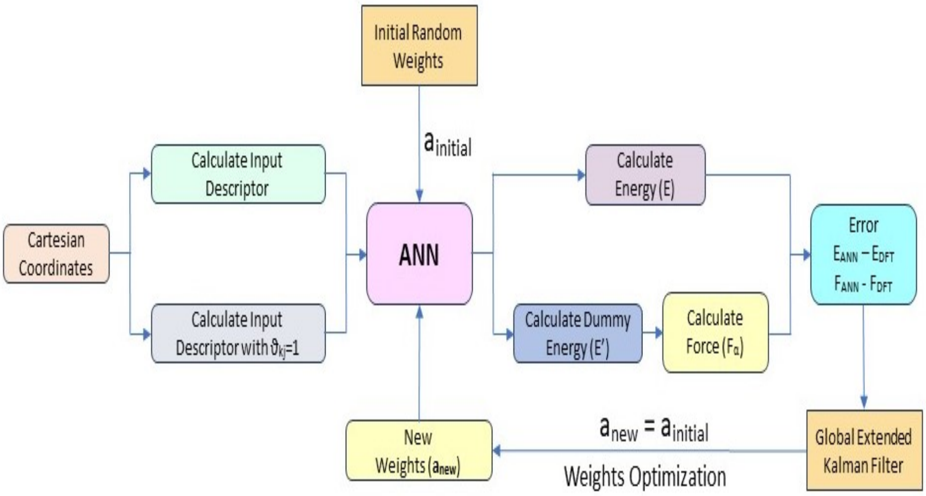

Figure 2.2: Calculation of energy and force using ANN for nanoalloy systems.

I calculate the force acting on the system by using the following expression for the χ^{th} component ($\chi = x, y, z$) of the force in terms of the derivative of energy with respect to input descriptor for nanoalloys:

$$F^i_\chi = -\frac{\partial E'_{cluster}}{\partial \chi_i} = -\sum_{N=1}^{atoms} \frac{\partial E'_N}{\partial \chi_i} = -\sum_{N=1}^{atoms}\sum_{k=1}^{M} \frac{\partial E'_N}{\partial G^\mu_{N,k}} \left(\omega_s \times \frac{\partial G^\mu_{N,k}}{\partial \chi_i}\right) \tag{2.66}$$

Here, $E'_{cluster}$ denotes the dummy energy of the cluster, which is determined by putting the bond-specific weighting factor $\vartheta_{ij} = 1$ in Eqs. 2.64 and 2.65. Such modifications in descriptors are required for smooth training of ANN without any numerical instability. In order to add the characteristics of an element to the local environment of the atom, I used an element-specific weighting factor (ω_s) to modulate the gradients of the descriptor with respect to the atomic coordinates. In Eq. 2.66, the weighting factor ω_s is defined as the ratio of the effective nuclear charge (Z_e) of the i^{th} atom to the total effective nuclear charge of all chemical species present in the molecular system.

2.5.4 Molecular Dynamics Simulation

The PES of any system can be explored using MD simulations to study its structural and dynamic properties. Since the 1980s, MD simulations [190, 191] have proven to be an effective tool for simulating molecular systems over time. Understanding the behaviour of chemical systems under realistic conditions requires accurate modeling of atomistic processes. Simulating these processes at finite temperatures provides valuable insights into the interactions and transformations within the system. Therefore, MD simulation techniques are crucial for tracking the dynamics of a chemical system and for computing ensemble-averaged properties, such as free energies, under different temperature and pressure conditions. The conventional method for simulating a chemical system over time involves using MD trajectories, where molecular positions are updated by following Newton's equations of motion.

$$F_i(t) = m_i \frac{\partial^2 r_i}{\partial t^2} \tag{2.67}$$

Where F_i denotes the force acting on the i^{th} atom, m is the mass of the atom, and r_i signifies the atomic positions described in cartesian coordinates. Hence, Newton's equations of motion in terms of potential energy ($V(r_i)$) are

$$F_i(t) = -\frac{\partial V(r_i)}{\partial r_i} \tag{2.68}$$

Hence,

$$m_i \frac{\partial^2 r_i}{\partial t^2} = -\frac{\partial V(r_i)}{\partial r_i} \tag{2.69}$$

In order to integrate the equations of motion, the MD simulations must calculate the forces of all atoms at each time step. In this study, ANN potential has been used to conduct the MD simulation at finite temperatures. The Verlet algorithm [192] is used to update the positions (r_i) and velocities (v) at each time step (t), and the Anderson thermostat [190] is utilized to keep the temperature constant during the simulation. The simulations were performed at different temperatures to study the PES of the nanoclusters.

MD trajectories were collected at varying temperatures and time steps. After the various initial configurations, structures were sampled every 1000 steps. These structures were then quenched using limited memory Broyden–Fletcher–Goldfarb–Shanno (L-BFGS) local optimization [112] to identify local minima on the PES, allowing for effective exploration of the surface.

2.6 Polarizability

To study the response properties of metal nanoclusters in this work, I focus on polarizability, which describes a material's ability to become polarized when exposed to an electric field. When a dielectric material is subjected to an external electric field, the charge distribution within its atoms or molecules is distorted, causing a displacement of charges (see Figure 2.3). The positive charges (nuclei) tend to move in the direction of the field, while the negative electrons are pushed in the opposite direction. When the electric field is extremely strong, atoms can be ionized. However, equilibrium is achieved for moderate field strengths. The electric field tends to displace the nuclei and electrons in opposite directions, though their mutual attraction still holds them together. As a result, the atom or molecule develops an induced electric dipole moment that depends on the applied field. For example, a neutral atom subjected to an electric field $\vec{F}$ acquires an induced dipole moment $\vec{\mu}$ that is roughly proportional to the field, This can be expressed as:

$$\vec{\mu} = \alpha \vec{F} \tag{2.70}$$

Here, α denotes the atomic polarizability, and the induced dipole aligns with the direction of the electric field.

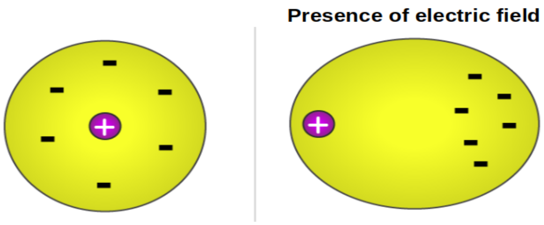

Figure 2.3: Polarization of molecule in the presence of electric field.

2.6.1 Polarizability Formulation

The interaction of an external electromagnetic field with matter results in the induction of dipole moment in the matter. The total dipole moment $\vec{p}$ can be expanded in a Taylor series in the power of external applied electric field $\vec{F}$ as [193]:

$$p_i = \mu_i + \sum_j \alpha_{ij} F_i F_j + \sum_{jk} \beta_{ijk} F_i F_j F_k + \sum_{jkl} \gamma_{ijkl} F_i F_j F_k F_l + \cdots, \tag{2.71}$$

where p_i and F_i denote the i^{th} $(i = x, y, z)$ component of dipole moment $\vec{p}$ and electric field $\vec{F}$, respectively. In the above expression, μ_i is the i^{th} component of permanent dipole moment which may be absent for some systems with special symmetry. On the other hand, the induced part of the dipole moment characterized by α_{ij} is the linear polarizability, and β_{ijk} and γ_{ijkl} are second- and third-order hyperpolarizabilities. Note that α, β, and γ are second-, third-, and fourth-rank tensors, respectively. In the present work, I focus on the calculations of static (that is frequency independent) polarizability only.

The interaction of the dipole moment with the external field in turn leads to a change in the energy of the material. The change in energy can also be expanded in powers of the applied electric field $\vec{F}$. Restricting up to second-order in the field, the change in energy is given by [193]:

$$\Delta E(F) = -\sum_i \mu_i F_i - \frac{1}{2} \sum_{i,j} \alpha_{ij} F_i F_j. \tag{2.72}$$

From Eq. 2.72, the static polarizability α_{ij} can be written in terms of the second derivative of energy with respect to electric field strength along i^{th}

and j^{th} axes:

$$\alpha_{ij} = \left[\frac{\partial^2 E}{\partial F_i \partial F_j}\right]_{F=0}, \tag{2.73}$$

or from Eq. 2.71, it can be written as the first derivative of i^{th} component of induced dipole moment with respect to the electric field along j^{th} axis:

$$\alpha_{ij} = \left[\frac{\partial p_i}{\partial F_j}\right]_{F=0}. \tag{2.74}$$

The expression for polarizability in terms of the derivatives of energy forms the foundation of the finite-field method. This method is successfully used to calculate static polarizability using a ground-state DFT-based approach. Notably, it does so without relying on the density functional perturbation theory (DFPT) approach [194–198].

As mentioned before, polarizability is a tensorial quantity consisting of nine components. In this thesis, I calculate two representative quantities characterizing the linear response properties of a cluster dependent on the nine components, namely, the average or isotropic polarizability (α_{iso}) given by:

$$\alpha_{iso} = \frac{1}{3}(\alpha_{xx} + \alpha_{yy} + \alpha_{zz}), \tag{2.75}$$

and anisotropy in polarizability ($\Delta\alpha$) defined as:

$$\Delta\alpha = \left\{\frac{1}{2}\left((\alpha_{xx}-\alpha_{yy})^2+(\alpha_{yy}-\alpha_{zz})^2+(\alpha_{zz}-\alpha_{xx})^2\right)+\left(6\alpha_{xy}^2+6\alpha_{yz}^2+6\alpha_{zx}^2\right)\right\}^{1/2}. \tag{2.76}$$

The α_{iso} provides a measure of the average polarizability of a molecule, while $\Delta\alpha$ provides a measure of the anisotropy of the cluster's electron density. Thus, both quantities are important in understanding how molecules interact with electric fields.

.

Chapter 3

Structure and Dynamics of Ag-Pt Nanoalloys

3.1 Introduction

Noble metal nanoclusters, particularly those containing platinum, are widely recognized for their superior catalytic properties in various chemical reactions, including CO oxidation [38, 39] and hydrogenation [40]. However, the high cost and limited availability of platinum have necessitated the development of more affordable bimetallic nanoclusters. Alloying platinum with transition metals like silver not only reduces platinum usage but also enhances catalytic performance through synergistic effects [41, 42, 44]. Ag-Pt nanoalloys have emerged as promising materials in catalysis due to their unique combination of high efficiency and reduced reliance on pure platinum [46, 50, 52]. The synergy between Ag and Pt atoms enhances catalytic performance, making these nanoalloys cost-effective alternatives. This has led to their extensive use in both catalysis and optoelectronics. The catalytic activity of Ag-Pt nanoalloys is strongly influenced by their size, composition, and atomic arrangement. By tailoring these factors, it is possible to optimize their performance and achieve higher selectivity and reactivity. The reactivity of Ag–Pt nanoalloys depends on their structure and composition. It becomes important to determine their atomic-level geometrical and electronic structures to develop a better understanding of their catalytic properties. In this chapter, I employ an ANN-based IAP to construct the PES of Ag-Pt nanoalloys. A bond-specific spherical harmonic descriptor is used as input to the ANN. Using this ANN-based IAP, I investigate the structural characteristics of several medium-sized 38-atom Ag-Pt nanoalloys and explore their temperature dependence. The choice of 38-atom clusters with a face-centred cubic (FCC) structure and truncated octahedron (TO) geometry is driven by the fact that this cluster size represents a magic number configuration. Additionally, the high symmetry of the TO geometry reduces the number of homotops and simplifies the study of diffusion mechanisms.

3.2 Computational Details

Descriptor: The atomic environment descriptors consist of 59 inputs, including 9 radial functions from Eq. (2.65) by varying the values of the parameters ε in Table 2.1, and 50 power spectrum coefficients obtained using Eqs. (2.60) and (2.61) for five different values of η (see Table 2.2), with the maximum value of $l = 10$. All the above parameters are chosen such that the optimal values of root mean square error in energy and force can be obtained in the training process of ANN [134, 177, 184, 185].

Dataset generation: For training datasets for $\text{Ag}_{38-n}\text{Pt}_n$ nanoclusters, I have used a variety of available configurations of bimetallic $\text{Ag}_m\text{Pt}n$ clusters, with m ranging from 18 to 55 and n from 1 to 28, to fit the energy and forces. In this way, I created 2000 different structures or data points of various clusters using MD simulations with the Gupta potential [73] as the IAP. Using these structures, I obtained the descriptors and trained the ANN with the energy of an atom as the output. The force acting on an atom was calculated by taking the derivative of the energy with respect to the descriptors. After obtaining the first set of initial weights, I conducted MD simulations at different temperatures to generate more data for the $\text{Ag}_{38-n}\text{Pt}_n$ nanoalloys. After removing any correlations in the data points, I collected approximately 11,000 data points. I shuffled this dataset of 11,000 data points and then divided it into two sets: a training set consisting of 10,200 structures and a testing set comprising the remaining 800 structures. I implemented a GEKF method to optimize the ANN weights.

DFT calculations: I used the VASP package [199] for all DFT-based calculations (single-point energy and optimizations). For these calculations, I employed the PBE exchange-correlation functional [160] within the GGA. The DFT-based calculations were performed using the PAW method with pseudo-potentials, taking into account the scalar relativistic effects. A gamma k-point $(1 \times 1 \times 1)$ mesh was applied to sample the Brillouin zone. The energy and force convergence was set to 10^{-4} and 10^{-3} respectively, and the energy threshold was set to 260 eV. For the entire dataset, a box length of $26 \times 26 \times 26$ Å^3 was used, with a vacuum dimension of 11 Å.

3.3 Results

3.3.1 Training and Testing of ANN Potential

The training phase uses a dataset of Ag-Pt nanoalloy configurations with corresponding DFT energies and forces. During training, the weights are iteratively updated, and after each iteration, the average root mean square error (RMSE) for energy and force is calculated to validate the model. Training stops when the RMSE on the testing set begins to increase. Figures 3.1.(a) and 3.1.(b) show the evolution of RMSE for energy and force during the training and testing of the ANN potential. In our calculations, the training procedure is considered to be completed once the value of RMSE in energy and force reaches 6 meV/atom and 125 (meV/Å)/atom, respectively, for the testing data set. To check the accuracy of the ANN-based results, the correlation plot between DFT energies ($\mathrm{E_{DFT}}$) and ANN energies ($\mathrm{E_{ANN}}$) of the test set is found to be linear and which can be seen in Figure 3.2. The energy per atom ($\mathrm{E_{ANN}}$) of various 38-atom nanoalloys with the corresponding results ($\mathrm{E_{DFT}}$) obtained through DFT-based

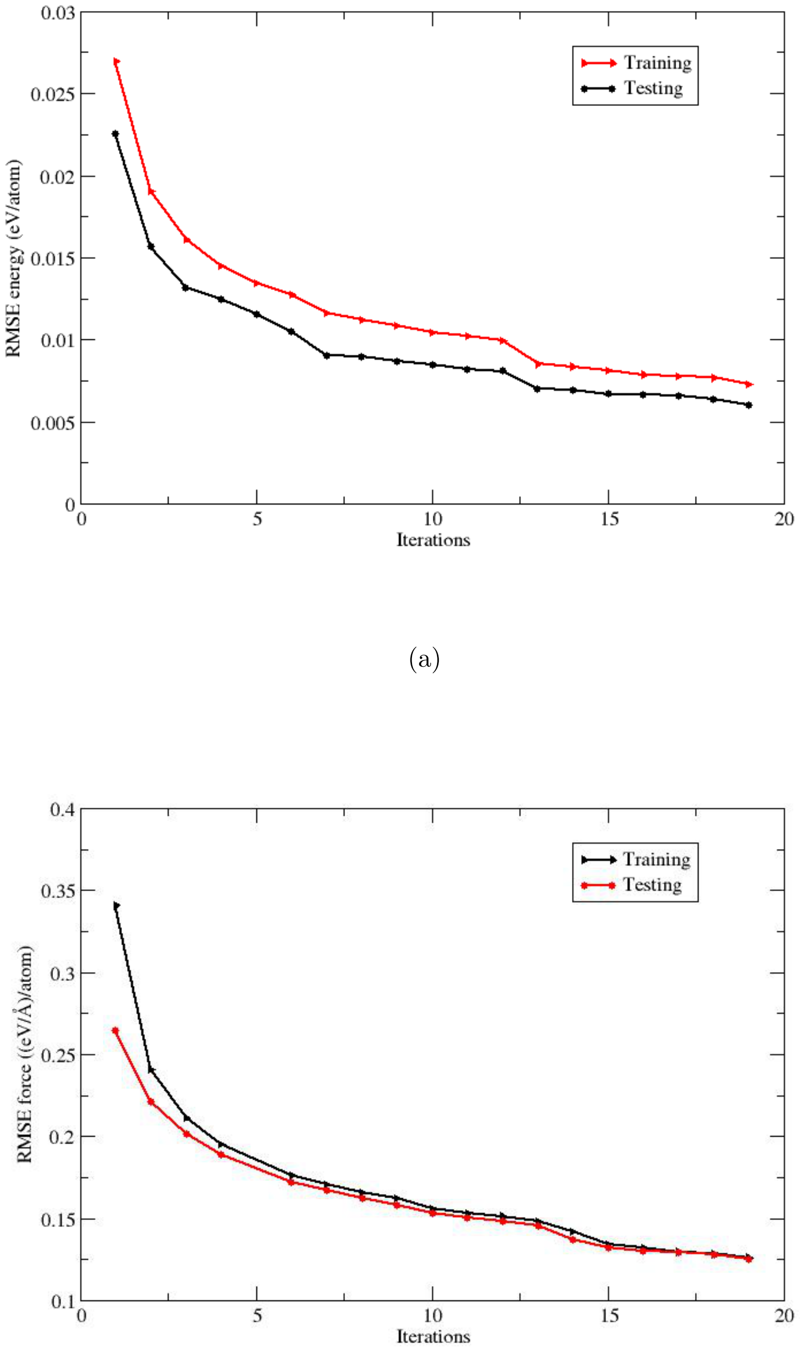

(a)

(b)

Figure 3.1: RMSE in energy and force decay with the number of iterations involved in the training and testing of data.

method. It is clearly evident that the two results match quite well, signifying the level of accuracy of the ANN-based potential obtained for Ag-Pt

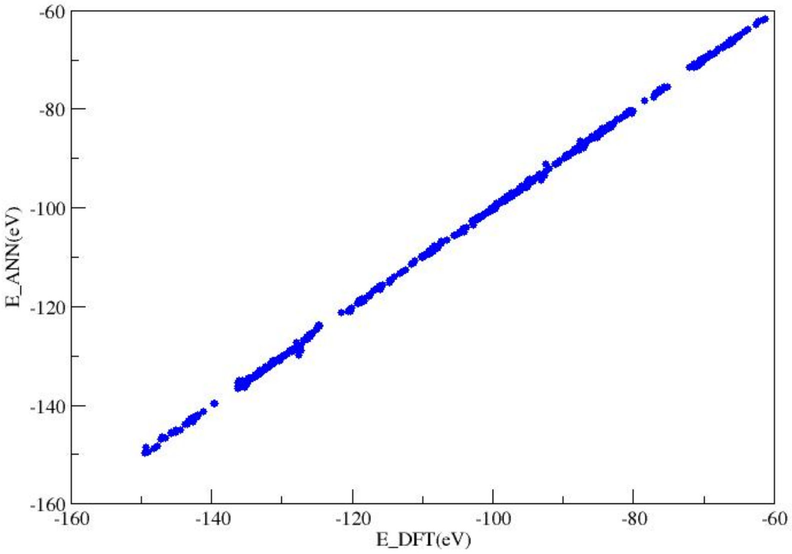

Figure 3.2: Correlation plot between DFT and ANN energies of Ag_mPt_n clusters.

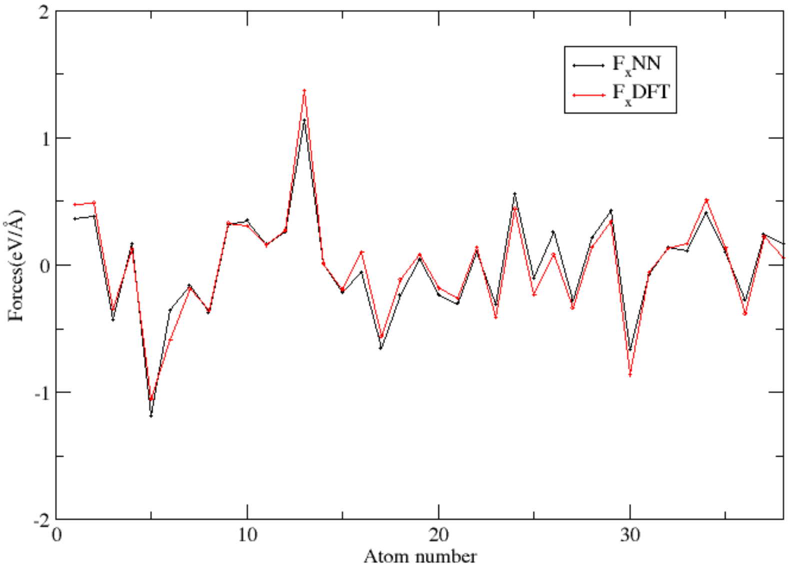

Figure 3.3: Comparison of x-component of force on $Ag_{34}Pt_4$ obtained employing DFT- and ANN-based methods.

nanoalloys. To further assess the accuracy of the ANN fitting, in Figure 3.3, I compared the results for the x-component of force acting on $Ag_{34}Pt_4$ cluster obtained using DFT- and ANN-based methods. This Figure 3.3 elucidates that the forces obtained by the ANN-based method are quite close to the corresponding DFT-based results. Therefore, from the accuracy of the results, it is natural to expect that the ANN-based method will yield IAP for the 38-atom Ag-Pt nanoclusters with good accuracy.

3.3.2 Global Optimization of $Ag_{38-n}Pt_n$ Nanoalloys

I have used ANN-based IAPs to carry out MD simulations to explore the PES of 38-atom $Ag_{38-n}Pt_n$ clusters. These simulations were carried out for 1.5 million time steps with a step size of 0.1 fs for different values of temperature in the range of 100 - 600K for each composition of $Ag_{38-n}Pt_n$ (where n = 1 - 8). Further, for each composition of the $Ag_{38-n}Pt_n$ nanoalloys, I generated several trajectories starting from randomly chosen initial configurations. For each trajectory, I took the structure after every 5000 steps and quenched it using the L-BFGS local optimization technique [112]. I collected the top 50 lowest-energy isomers for each composition of $Ag_{38-n}Pt_n$ nanoalloys predicted by ANN potential and re-optimized their geometries with the DFT-based method. I found that the energy ordering predicted using the ANN-based method is identical to that obtained with DFT. The energies of the lowest-energy isomers predicted by ANN- and DFT-based methods for each composition of $Ag_{38-n}Pt_n$ nanoalloys are tabulated in Table 4.1. From this table, it can be seen that the two results for the energy are very close, and ANN-based numbers are slightly higher than those obtained with DFT.

For completeness, I have shown in Figure 3.4 the geometric structure of the lowest energy configurations of $Ag_{38-n}Pt_n$ nanoalloys obtained with the ANN-based method. First of all, I note from this figure that the structural pattern of 38-atom $Ag_{38-n}Pt_n$ nanoalloys consists of 32 atoms located on the surface region, and the remaining six atoms occupy the core region of the clusters. For $Ag_{38-n}Pt_n$ nanoalloys, the lowest isomers are found to possess a core-shell structure. The core-shell structure is favoured for $Ag_{38-n}Pt_n$ nanoalloys because of stronger Pt-Pt interactions in comparison to Ag-Ag interactions and the greater surface energy of the Pt surface in comparison to that of the Ag surface [15]. Due to these factors, Pt atoms occupy the core region, and Ag atoms occupy the surface sites. Further, it is observed that for n = 1 - 6, all the Pt atoms are located at the core region of the $Ag_{38-n}Pt_n$ nanoalloys. On the other hand, for n = 7 and 8, the six Pt atoms are located in the core regions, and the remaining Pt atoms (one for n = 7 and two for n = 8) occupy the centre of the hexagonal faces forming the surface of each structure. Having discussed the general structural pattern of $Ag_{38-n}Pt_n$ nanoalloys, next I focus our attention on the geometric characteristics of the individual nanoalloys. At this point, it should be noted that except for $Ag_{37}Pt_1$ nanoalloy, the geometric structures of all the other nanoalloys obtained with ANN- and DFT-based calculations are identical.

Table 3.1: Energies of lowest energy isomers of $Ag_{38-n}Pt_n$ nanoalloys predicted by ANN- and DFT-based methods.

Composition	ANN(eV)	DFT(eV)
$Ag_{37}Pt_1$	-85.5405	-85.5716
$Ag_{36}Pt_2$	-88.7306	-89.0227
$Ag_{35}Pt_3$	-92.2483	-92.3998
$Ag_{34}Pt_4$	-95.6127	-95.9418
$Ag_{33}Pt_5$	-98.7986	-98.8902
$Ag_{32}Pt_6$	-101.7942	-102.0207
$Ag_{31}Pt_7$	-104.6887	-104.8421
$Ag_{30}Pt_8$	-108.3238	-107.9898

In the case of $Ag_{37}Pt_1$, the ANN potential predicts an amorphous kind of structure as shown in Figure 3.4(b). On the other hand, DFT-based calculations yielded a symmetric structure with O_h symmetry for the lowest energy isomer, which is shown in Figure 3.4(c). For all other nanoalloys, the ANN-based potential predicts symmetric structures which are identical to those obtained with DFT-based calculations. In all the cases, the Pt atoms prefer to occupy the core position (see Figure 3.4). The generic structure of the core regions in all these nanoalloys exhibits an O_h-type symmetry except for $Ag_{37}Pt_1$ (see Figure 3.5). In the case of $Ag_{32}Pt_6$, all six core sites of O_h-type symmetry are occupied by the Pt atoms and all the 32 surface sites are fully occupied by the Ag atoms, leading to the formation of a perfect core-shell structure.

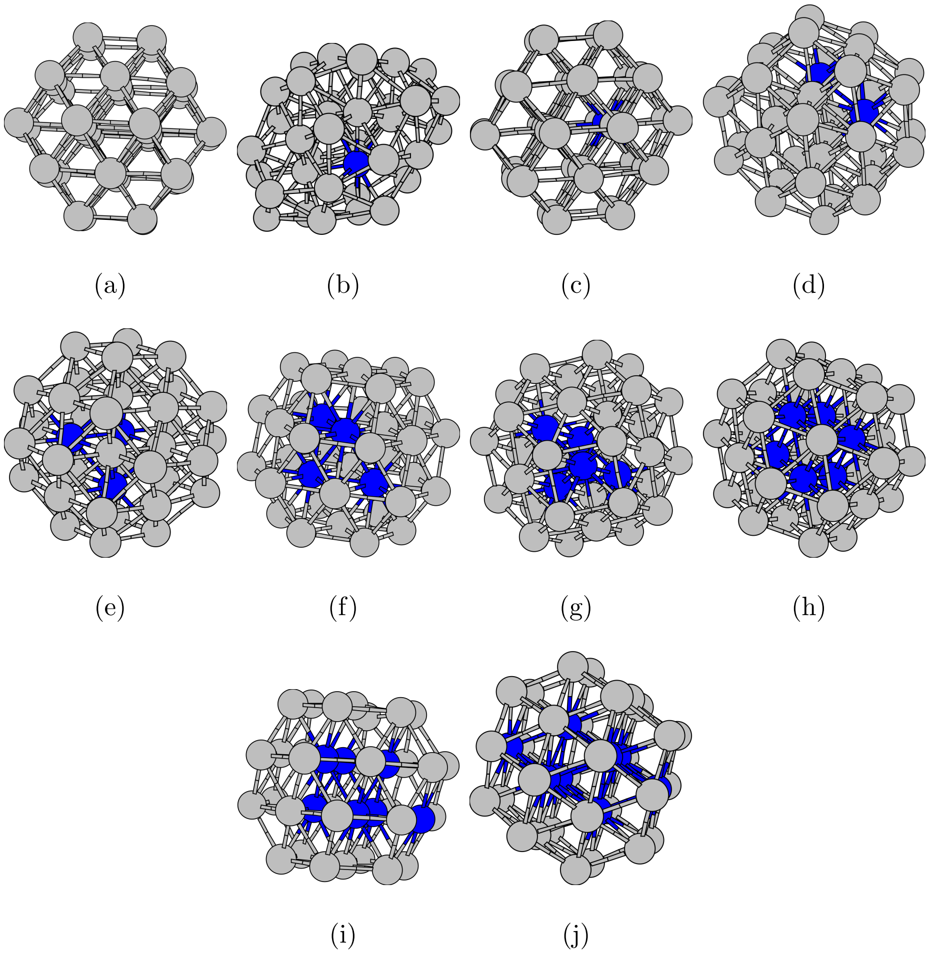

(a) (b) (c) (d)

(e) (f) (g) (h)

(i) (j)

Figure 3.4: Lowest energy isomers of (a) Ag_{38} (b) $Ag_{37}Pt_1$ (predicted with ANN), (c) $Ag_{37}Pt_1$ (predicted with DFT), (d) $Ag_{36}Pt_2$, (e) $Ag_{35}Pt_3$, (f) $Ag_{34}Pt_4$, (g) $Ag_{33}Pt_5$, (h) $Ag_{32}Pt_6$, (i) $Ag_{31}Pt_7$, and (j) $Ag_{30}Pt_8$. Grey and blue balls represent Ag and Pt atoms, respectively.

3.3.3 Energetic Analysis

I examine the relative stability of the different compositions of $\mathrm{Ag}_{38-n}\mathrm{Pt}_n$ nanoalloys. For this, I calculate the excess energy (E_{exe}) and the second-order energy difference ($\Delta_2 E$), for each of them [200–202]. The excess energy, which is given in Eq. 3.1, has been used to investigate the relative stabilities of the nanoalloys.

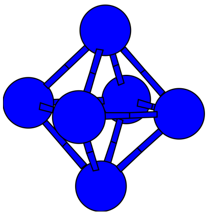

Figure 3.5: The geometry of the generic inner core of $\mathrm{Ag}_{38-n}\mathrm{Pt}_n$ nanoalloys, where n = 2 - 8. Blue balls represent Ag/Pt atoms.

$$E_{\mathrm{exe}} = \frac{1}{38}[E_{\mathrm{tot}}^{Ag_{38-n}Pt_n} - \frac{(38-n)}{38}E_{\mathrm{tot}}^{\mathrm{Ag}} - \frac{n}{38}E_{\mathrm{tot}}^{\mathrm{Pt}}] \tag{3.1}$$

where $E_{\mathrm{tot}}^{\mathrm{Ag}_{38-n}\mathrm{Pt}_n}$, $E_{\mathrm{tot}}^{\mathrm{Pt}}$, and $E_{\mathrm{tot}}^{\mathrm{Ag}}$ are total energies of $\mathrm{Ag}_{38-n}\mathrm{Pt}_n$, Pt_n and Ag_n system, respectively. The negative value E_{exe} indicates that the alloy formation is energetically favourable and $E_{\mathrm{exe}} = 0.0$ eV for pure Ag (n = 0) and pure Pt (n = 38). On the other hand, the second-order energy difference is a measure of the stability of a cluster of a particular composition relative to its neighbours. The second-order energy difference for $\mathrm{Ag}_{38-n}\mathrm{Pt}_n$ nanoalloys is determined by using the following expression:

$$\Delta_2 E_{Ag_{38-n}Pt_n} = [E_{\mathrm{tot}}^{Ag_{38-n-1}Pt_{n+1}} + E_{\mathrm{tot}}^{Ag_{38-n+1}Pt_{n-1}} - 2E_{\mathrm{tot}}^{Ag_{38-n}Pt_n}] \tag{3.2}$$

A positive value $\Delta_2 E$ generally indicates a stable composition relative to its neighbour. In Figure 3.6, I display the excess energy as a function of the composition of nanoalloys. From this figure, it is evident that this $\mathrm{Ag}_{32}\mathrm{Pt}_6$ is the most stable composition because it has the minimum value

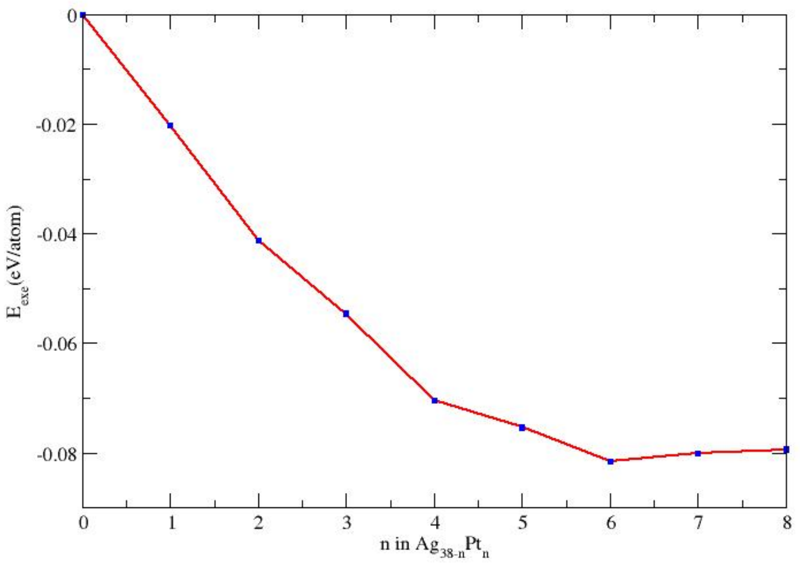

Figure 3.6: The excess energy plot with respect to the number of Pt atoms in 38-atoms $Ag_{38-n}Pt_n$ nanoalloys.

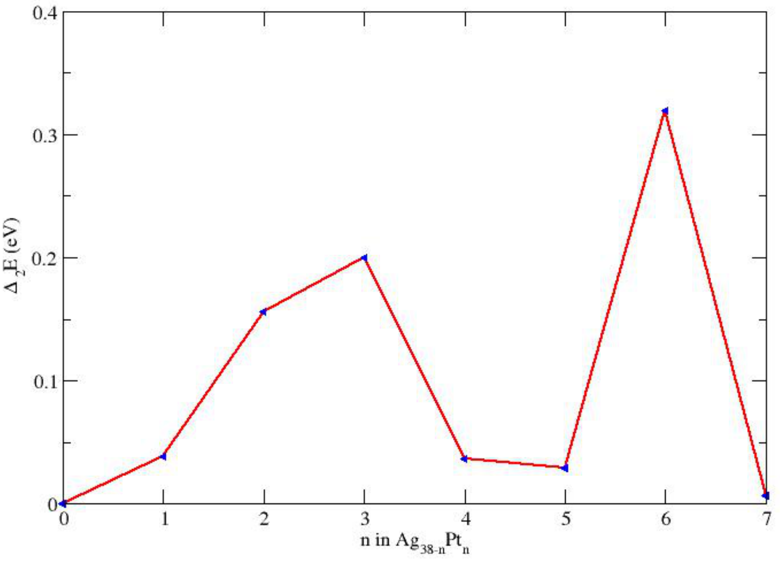

Figure 3.7: Plot shows the second-order energy differences with respect to the number of Pt atoms in 38 atoms $Ag_{38-n}Pt_n$ nanoalloys.

of E_{exe}. Furthermore, in Figure 3.7, I depicted the $\Delta_2 E$ as a function of the composition of nanoalloys. The maximum value for the $\Delta_2 E$ is also observed for the $\text{Ag}_{32}\text{Pt}_6$ nanoalloy. Usually, a cluster with a high positive value $\Delta_2 E$ has high stability relative to its neighbouring clusters. Thus, from the point of view of excess energy and second-order energy difference, I observed that this $\text{Ag}_{32}\text{Pt}_6$ is the most stable composition in comparison to other isomers. This is also consistent with the fact that the $\text{Ag}_{32}\text{Pt}_6$ nanoalloy possesses a perfect core-shell-type structure, as discussed above and shown in Figure 3.4.

3.3.4 Charge Transfer Analysis

The phenomenon of charge transfer plays a key role in determining the chemical stability and reactivity of the nanoalloys. This phenomenon leads to an uneven distribution of charges, which in turn may give rise to the polarization of the nanoalloys. To estimate the charge distribution on Ag and Pt atoms in $\text{Ag}_{38-n}\text{Pt}_n$ nanoalloys, I used Bader's approach [203] to partition the nanoalloy into atomic volumes by identifying the zero-flux surfaces in the electron density field. This method calculates the Bader charge (Q^B), which represents the total electron density confined within each atom's Bader volume. I determined the effective charge on each atom using the Multiwfn tool [204], which allows for detailed charge analysis based on the Bader partitioning scheme. From the Q^B values, I computed the effective Bader charge (Q^B_{eff}) using the formula:

$$Q^B_{\text{eff}} = Z_{\text{val}} - Q^B$$

where Z_{val} is the number of valence electrons of the neutral atom. A positive Q^B_{eff} indicates that the atom has lost electrons (cationic), while a negative Q^B_{eff} indicates electron gain (anionic). This charge transfer behavior is attributed to the electronegativity difference between Pt and Ag atoms. The results of the average charge distributions on the Pt atoms in $\text{Ag}_{38-n}\text{Pt}_n$ nanoalloys are compiled in Table 3.2. From this table, it can be seen that for all the nanoalloys, the Pt atoms residing in the core region carry a negative charge. On the other hand, for n = 7 and 8, the charge of the Pt atom residing in the surface region is more (-0.202 e for n = 7 and -0.2515 e for n = 8) than that of Pt atoms located in the core region. Therefore, for $Ag_{38-n}Pt_n$ nanoalloys, the Pt atoms residing both in the core and surface regions are anionic, whereas the Ag atoms acquire a cationic character. Hence, the charge distribution shows that in $Ag_{38-n}Pt_n$ nanoalloys, the charge transfer takes place from Ag to Pt as a Pt atom is more electronegative than an Ag atom.

The above results have an important bearing on the reactivity of these nanoalloys towards the adsorption of CO and O_2 molecules. In order to use Ag-Pt nanoalloys as the catalyst of the CO oxidation reaction, it would be more advantageous to have the Pt atoms, which are rich in negative charges, be located in the surface region for greater exposure to the incoming gas molecules involved in the concerned reaction. At elevated temperatures, it is possible to bring out more Pt atoms on the surface to increase their exposure to the impinging gas molecules. For this purpose, it is necessary to get an idea of the temperature range at which Pt atoms are more likely to be found in the surface region and estimate the probability of such occurrences.

Table 3.2: Average charge distribution over Pt and Ag atoms on $Ag_{38-n}Pt_n$ nanoalloys (where n = 1 - 8).

Composition	charge on Pt(e)	charge on Ag(e)
$Ag_{37}Pt_1$	-0.545720	0.02122
$Ag_{36}Pt_2$	-0.528483	0.02845
$Ag_{35}Pt_3$	-0.392453	0.03363
$Ag_{34}Pt_4$	-0.319539	0.03759
$Ag_{33}Pt_5$	-0.257644	0.03903
$Ag_{32}Pt_6$	-0.220839	0.04140
$Ag_{31}Pt_7$	-0.221869	0.05009
$Ag_{30}Pt_8$	-0.247435	0.05983

3.3.5 Probability of Pt atom on the Surface at Finite Temperature

The active sites play a vital role in heterogeneous catalysis, as the adsorption of the gaseous molecules occurs at these locations on the surface. Generally, all the sites are not equally active. The reactivity of any site depends on the arrangement of atoms on the surface and their chemical compositions. Knowing that the locations of Pt atoms on the surface may turn out to be reactive, I calculate the probability of getting the structures of $Ag_{38-n}Pt_n$ nanoalloys with at least one of the Pt atoms located on the surface. For this purpose, I computed the ratio of the number of structures for which at least one Pt atom is located on the surface to the total number of possible structures in the MD trajectories at a specific temperature. To this end, I performed the MD simulations for 1 million time steps at four different temperatures: 300K, 320K, 340K, and 360K. As the melting temperature for pure Ag_{38} is 375K (obtained using classical MD simulations), [205] all the MD calculations are performed at temperatures below 375K.

Table 3.3: Probability of surface Pt atom in $Ag_{38-n}Pt_n$(for n=1-8) at finite temperature.

Composition	300(K)	320(K)	340(K)	360(K)	P_B(360K)
$Ag_{37}Pt_1$	0	0	0	15.0	0
$Ag_{36}Pt_2$	0	0	0	58.8	0
$Ag_{35}Pt_3$	0	0	65.7	87.0	96.4
$Ag_{34}Pt_4$	0	0	67.0	83.2	85.8
$Ag_{33}Pt_5$	0	0	74.7	82.5	98.3
$Ag_{32}Pt_6$	0	0	0	98.3	99.0
$Ag_{31}Pt_7$	100	100	100	100	100
$Ag_{30}Pt_8$	100	100	100	100	100

As shown in Table 3.3, at 300K, for each composition of $Ag_{38-n}Pt_n$ (n = 1 - 6) nanoalloys, the probability of finding a Pt atom on the surface is zero. On the other hand, for $Ag_{31}Pt_7$ and $Ag_{30}Pt_8$ nanoalloys, I find that the six Pt atoms are always located in the core regions, and the remaining Pt atoms occupy the surface sites. From the results presented in Table 3.3, I infer that in the temperature range of 300K to 360K, at least one Pt atom will certainly be found on the surface sites of Ag-Pt nanoalloys. At 340K, the probability is greater than 60% for $Ag_{35}Pt_3$,$Ag_{34}Pt_4$ and $Ag_{33}Pt_5$ and at 360K, it is greater than 80% for $Ag_{35}Pt_3$, $Ag_{34}Pt_4$, $Ag_{33}Pt_5$ and $Ag_{32}Pt_6$.

For the sake of completeness, in Table 3.3, I also presented a more traditional method to compute probabilities using the Boltzmann factor at 360 K. I employed the following method to calculate Boltzmann probabilities. The global minimum structure for each composition is used as the initial structure for MD simulations. After removing 30% initial steps, I extracted one structure in every 1000 steps of the MD trajectory to create an ensemble of 700 structures. In the ensemble, I selected the structure with the lowest energy, E_{ref}, as the reference structure. The probability of i^{th} isomer in the ensemble is given by $P_i = \frac{e^{(E_i - E_{ref})/KT}}{\sum e^{(E_i - E_{ref})/KT}}$. I have also shown the total energies of the MD trajectory for the ensemble of 700 structures for $Ag_{35}Pt_3$,$Ag_{34}Pt_4$ and $Ag_{33}Pt_5$ in Figures 3.8, 3.9, and 3.10 respectively, obtained both at 340K and 360K. At 340K, for all the compositions except $Ag_{31}Pt_7$ and $Ag_{30}Pt_8$, the reference structure is the structure with all Pt atoms residing in the core. Hence, the Boltzmann probability for all the compositions favours structures with all Pt atoms in the core. This is also evident from Figures 3.8 (a), 3.9 (a), and 3.10 (a), in which I can clearly see that the total energies of structures with core Pt atoms are generally lower in energies in comparison to structures with at least one Pt atom on the surface by more than 2 eV. Here, it should be noted that the cumulative Boltzmann probability, $P_B = \sum P_i$, is the sum of probabilities of all the isomers in which at least one Pt atom is on the surface of the cluster. Therefore, at 340K, P_B values can be considered zero for all practical purposes and are not shown explicitly in Table 3.3. At 360K, the total energies in Figures 3.8 (b), 3.9 (b), and 3.10 (b) correspond mostly to structures

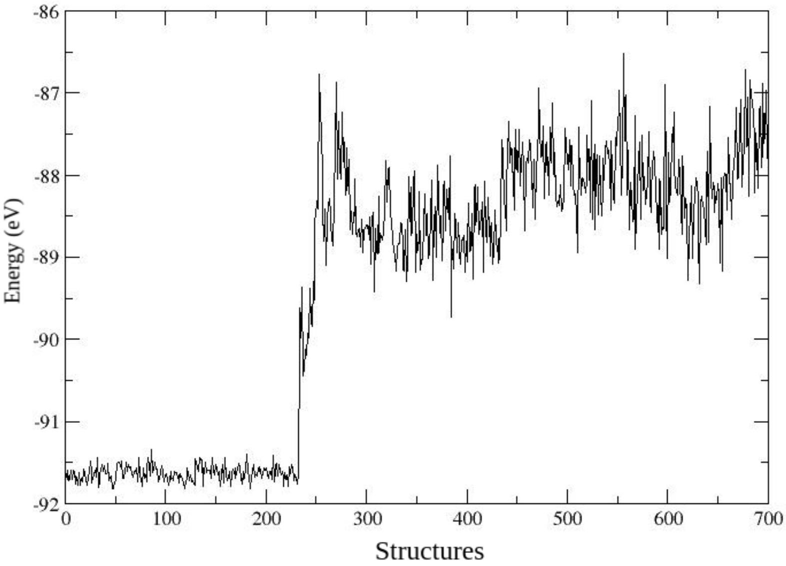

(a)

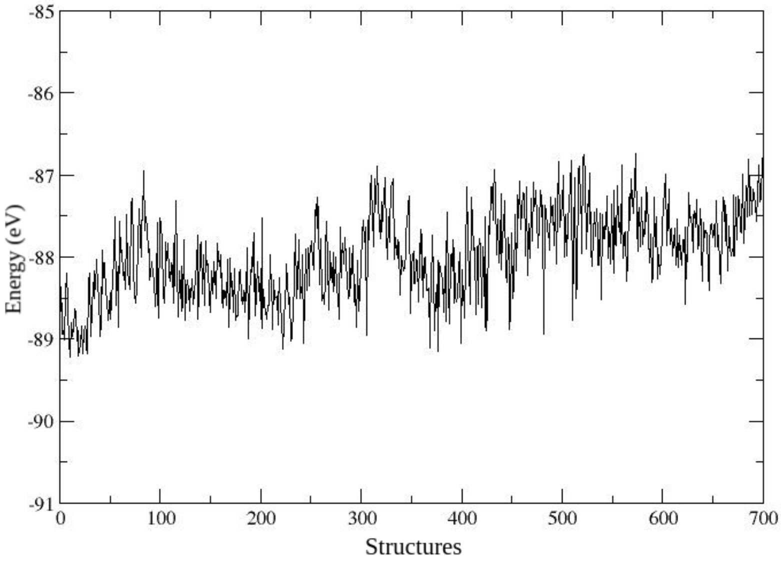

(b)

Figure 3.8: MD trajectories of $Ag_{35}Pt_3$ at (a) T=340K and (b) T=360K.

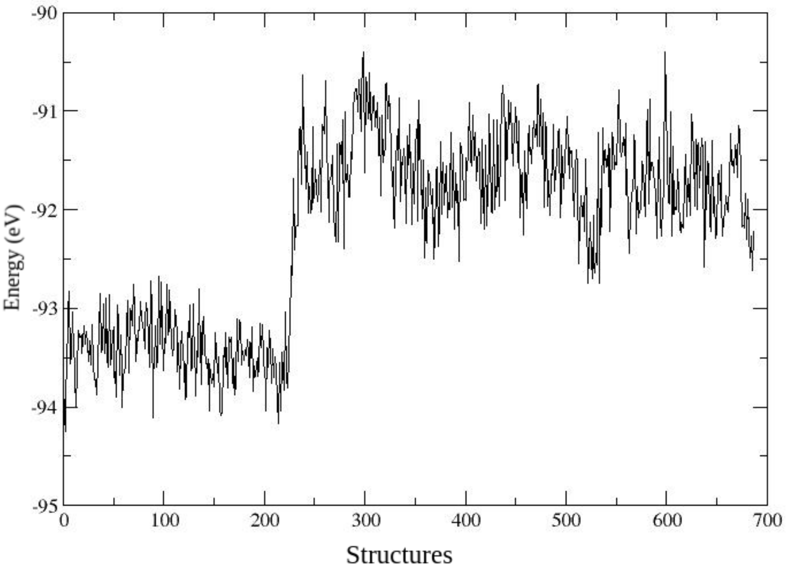

(a)

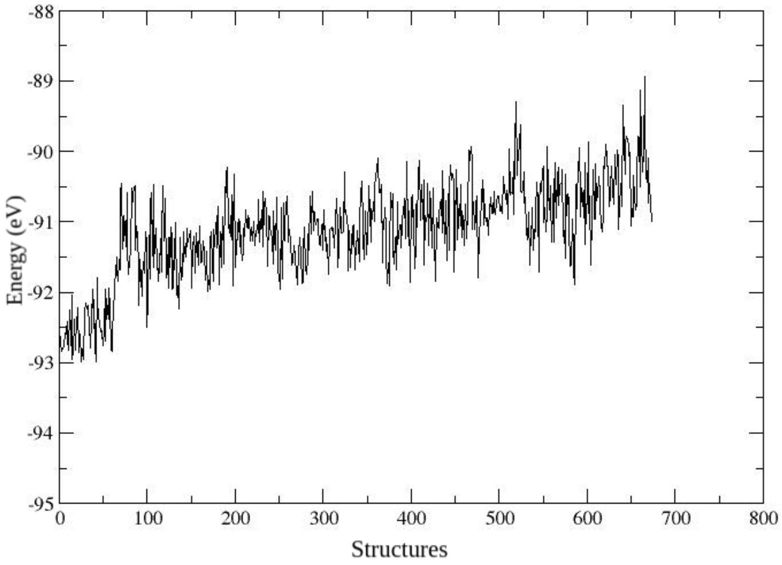

(b)

Figure 3.9: MD trajectories of $Ag_{34}Pt_4$ at (a) T=340K and (b) T=360K.

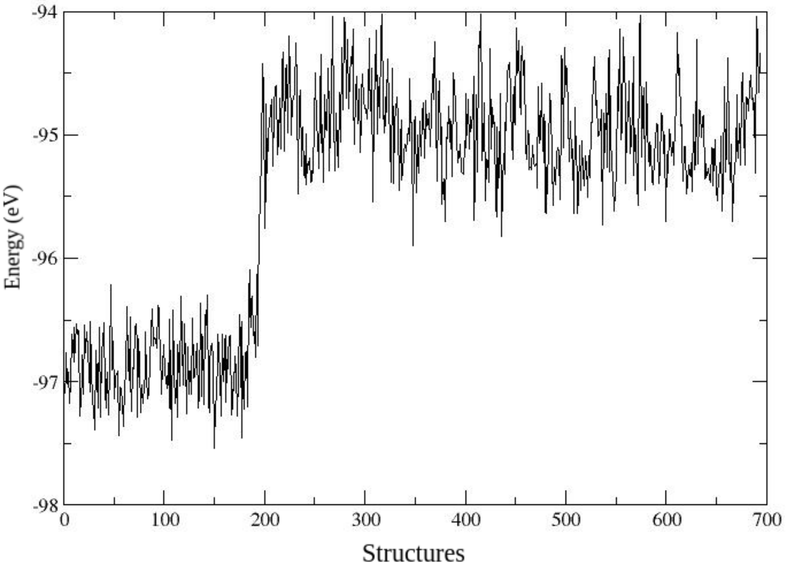

(a)

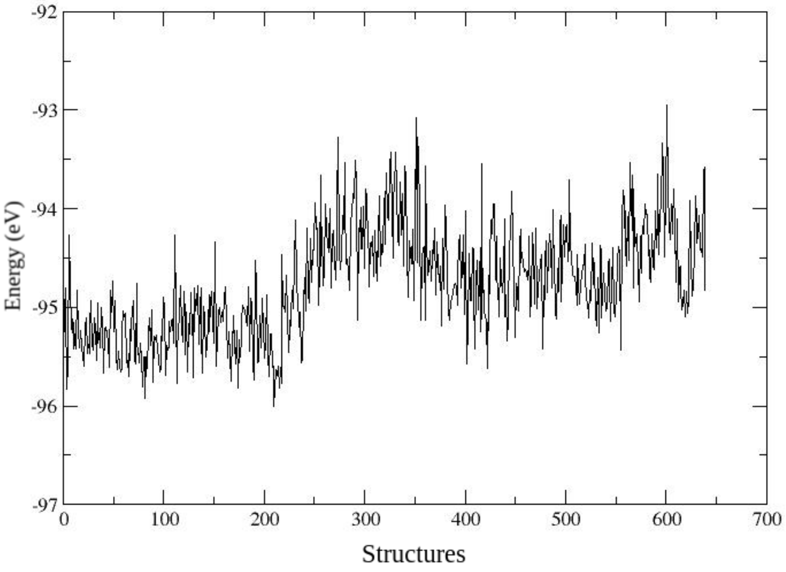

(b)

Figure 3.10: MD trajectories of $Ag_{33}Pt_5$ at (a) T=340K and (b) T=360K.

with at least one Pt atom on the surface. In Table 3.3, at 360K, the P_B values calculated for $Ag_{35}Pt_3$,$Ag_{34}Pt_4$ and $Ag_{33}Pt_5$ favour structures with one or more than one Pt atom on the surface. From this study, I can conclude that at 360K, the probability of structures with at least one surface Pt atom is in good agreement with cumulative Boltzmann probabilities.

3.4 Summary

In summary of this work, an ANN-based IAP has been constructed for Ag-Pt nanoalloys. The resulting ANN potential accurately fits both the energies and the forces obtained using DFT for Ag-Pt nanoalloys. Using ANN-based IAP, MD simulations and global optimizations of $Ag_{38-n}Pt_n$ (where n = 1–8) nanoalloys have been performed. It is found that the lowest energy isomers obtained are the core-shell structures, with Ag atoms occupying the surface sites and Pt atoms occupying the core locations. It has also studied the relative stability of $Ag_{38-n}Pt_n$ nanoalloys by investigating the excess energy and second-order energy difference calculations. It is found that the composition $Ag_{32}Pt_6$ is a more favourable isomer compared to the other isomers. By examining the charge distribution in $Ag_{38-n}Pt_n$ nanoalloys, it has been shown that the Pt atoms carry a negative charge, whereas the Ag atoms carry a positive charge. The charge transfer that occurs from the surface Ag atoms to the core Pt atoms provides further stability to the nanoalloys. It is well known that the locations of Pt atoms in the clusters are generally reactive and responsible for the reactivity of nanoalloys. Keeping this in mind, the probability of finding Pt atoms at the surface sites at finite temperatures has been calculated. It is found that for all the isomers of $Ag_{38-n}Pt_n$ nanoalloys, at least one Pt atom is certain to be found at the surface sites of nanoalloys at a temperature above 360K.

.

Chapter 4

Small Molecules Adsorption on Ag-Pt Nanoalloys

4.1 Introduction

In Chapter 3, an ANN-based IAP was developed to fit the PES of medium-sized Ag-Pt nanoalloys. It was observed that in the lowest energy isomers of 38-atom Ag-Pt nanoalloys, Pt atoms tend to occupy core positions, while Ag atoms prefer surface sites. These surface sites are crucial in heterogeneous catalysis, as they serve as active locations for the adsorption of gaseous molecules. The atomic arrangement and chemical composition of the surface influences the reactivity of these sites. It has been established that Pt-based nanoalloys enhance their stability and reactivity, exhibiting selective catalytic activity in various chemical reactions [8, 61, 206]. Their interaction with gases like CO and O_2 has been widely studied to evaluate their effectiveness as nanocatalysts, particularly for CO oxidation reactions. This reaction plays a vital role in environmental protection by helping to remove harmful CO emissions from automobile exhausts and hydrogen gases used in fuel cells [207–209]. The key step in this process involves the adsorption and activation of these molecules on the catalyst's surface. Ag-Pt nanoalloys, a subclass of Pt-based systems, are investigated as high-potential catalysts for CO oxidation and oxygen reduction reactions (ORR) due to their distinct structural and electronic properties. Adsorption and activation of O_2 are crucial steps for enabling environmentally sustainable and industrially significant reactions like CO oxidation. Studies have highlighted the structural stability, catalytic activity, and selectivity of Ag-Pt nanoalloys, which are closely tied to their structural arrangement and surface phenomena. These properties make them highly promising for diverse catalytic applications [45, 46, 50, 52].

In this chapter, I employ an ANN-based method to construct a PES for the 55-atom Mackay Ih structure of Ag-Pt nanoalloys. Specifically, I modeled different compositions of $\mathrm{Ag}_{55-n}\mathrm{Pt}_n$, where n ranges from 0 to 14. This approach has enabled the identification of the global minimum structure of the nanoalloys using MD simulations. Additionally, the adsorption of O_2 and CO molecules on $\mathrm{Ag}_{55-n}\mathrm{Pt}_n$ nanoalloys has been systematically analyzed using DFT methods.

4.2 Computational Details

The dataset is a crucial component in generating PES. The ANN-based method was employed to fit the dataset using descriptor functions. As discussed in Chapter 2, the input functions for the network are generated by modifying the values of ε in Eqs. 2.65 and η in Eqs. 2.64, respectively. By taking the radial distribution of the surrounding atom, I use nine radial functions by employing Eq. 2.65. For the angular environment, I use fifty power spectrum coefficients, resulting in 59 input descriptors for each atom in the ANN. I curated the dataset, producing around 10,980 structures of $\mathrm{Ag}_m\mathrm{Pt}_n$ nanoalloys, ranging from 23 to 78 Ag atoms and 1 to 51 Pt atoms. The dataset was split into 9900 training and 1080 testing data points. I used a GEKF optimization method [177] to optimize the ANN weights. In the training of the ANN potential, I determined both the energy and forces for our reference dataset using the DFT in VASP package [199]. The DFT calculations are carried out using the PAW method with pseudo potential and scalar relativistic effects. I used the PBE exchange-

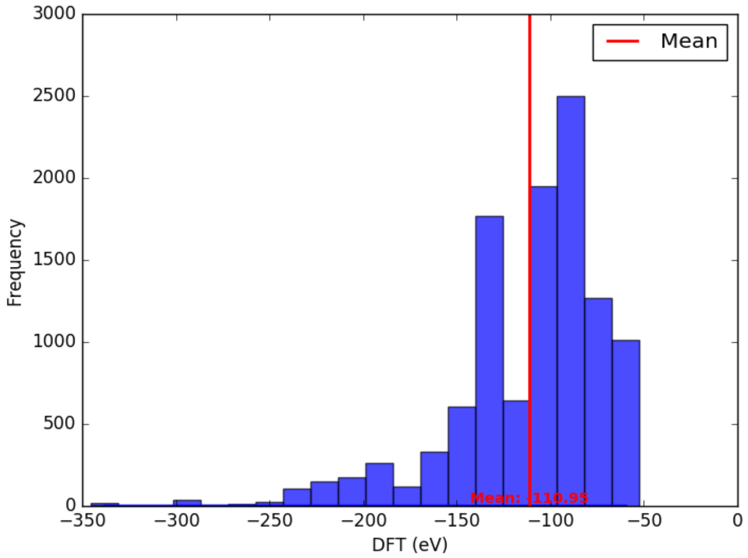

Figure 4.1: Distribution of the fitted data from the DFT method. The red line represents the mean of the data.

correlation functional [160] within the GGA. A gamma k-point ($1 \times 1 \times 1$) mesh has been used to sample the Brillouin zone. The energy and force convergence parameter was set to 10^{-4} eV and 10^{-3} eV/Å, and the cutoff energy is set to 260 eV. A box length of $26 \times 26 \times 26$ Å^3 is used for the complete dataset, with a vacuum dimension of 11 Å.

4.3 Results

4.3.1 Fitting of PES using ANN-based Potential

ANN has been trained to minimize the error of energy and the force on each atom calculated using ANN and DFT. The training was conducted in an iterative manner, and the RMSE for energy and forces on the test dataset was calculated and is shown in Fig 4.2(a) and 4.2(b), respectively. The RMSE values for energy and forces on the test dataset are found to be 7.5 meV/atom and 133 (meV/Å)/atom, respectively. To further evaluate the accuracy of the ANN fitting, I have also plotted the correlation between DFT energies and ANN energies in Figure 4.3. This linear correlation of DFT and ANN energies indicates that the ANN-based method is in agreement with the DFT method. I depicted the absolute error per atom (in eV/atom) for all the clusters in the test set in Figure 4.4. The mean of the absolute error is 0.009 eV/atom, and the maximum absolute error is close to 0.088 eV/atom. It is important here to note that absolute errors greater than 0.04 eV/atom arise mainly due to large-size clusters. This is because the number of large-sized clusters in the training data set is very small in comparison to medium-sized clusters, as shown in Figure 4.1.

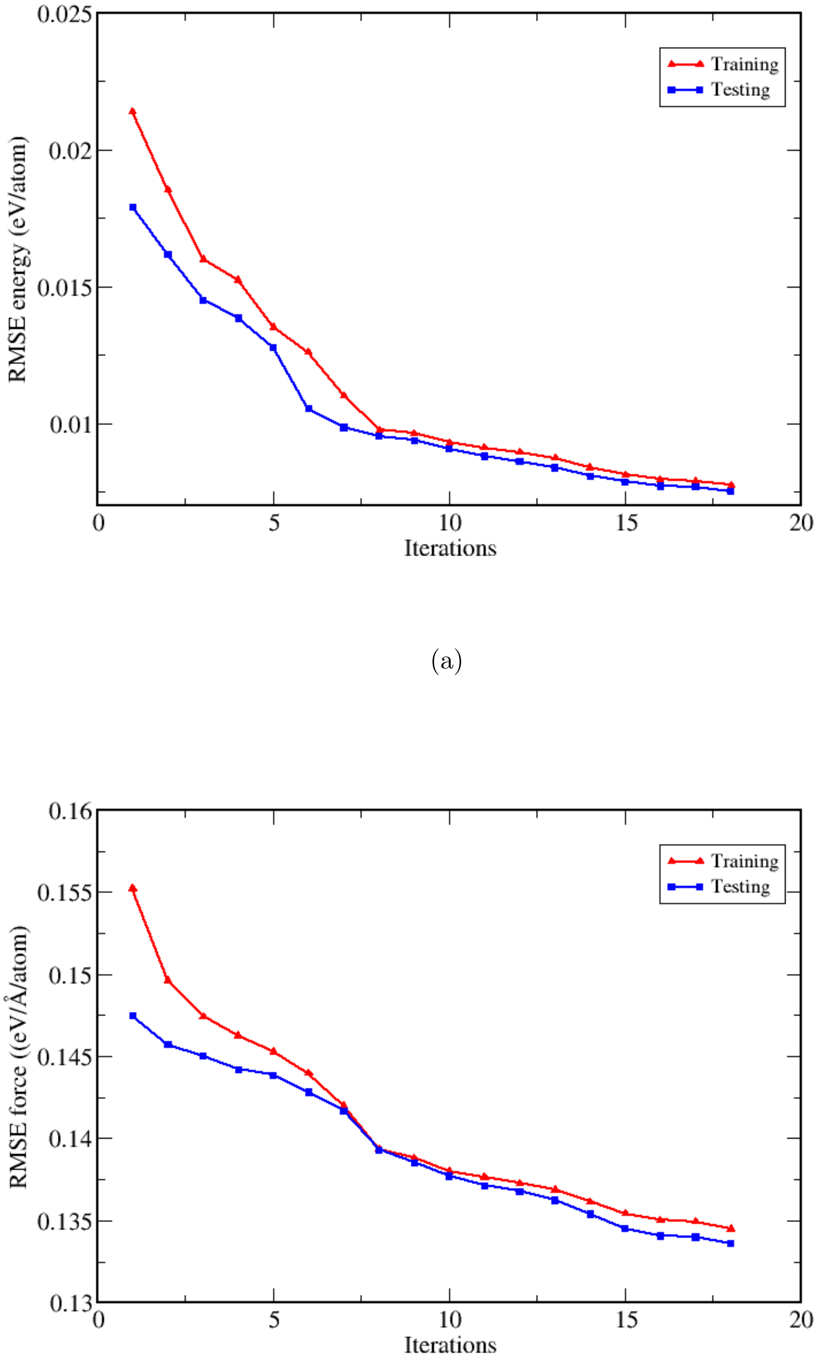

(a)

(b)

Figure 4.2: RMSE in (a) energy and (b) force decay with the number of iterations involved in the training and testing data.

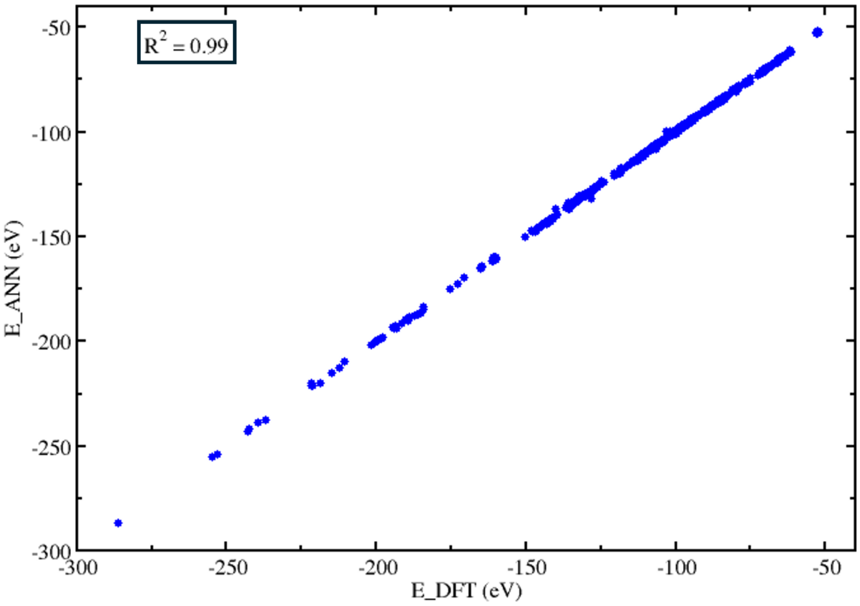

Figure 4.3: The correlation plot between DFT energies and ANN energies for Ag_mPt_n clusters.

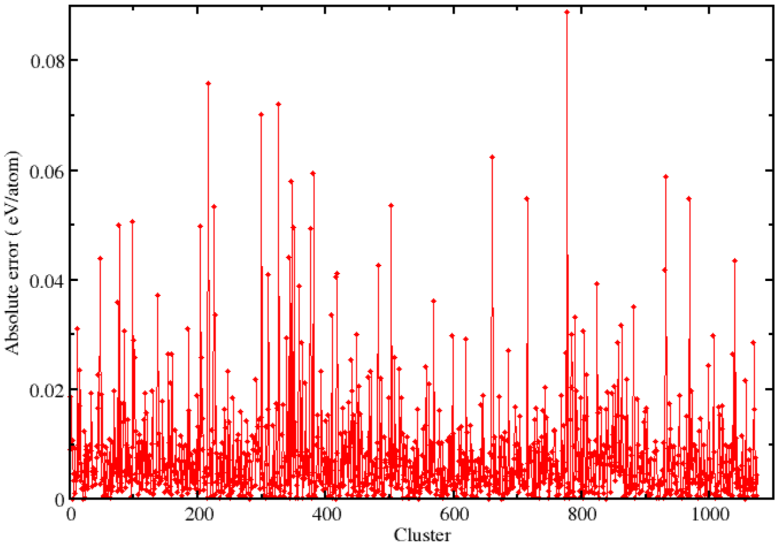

Figure 4.4: Plot showing the absolute error for Ag_mPt_n clusters.

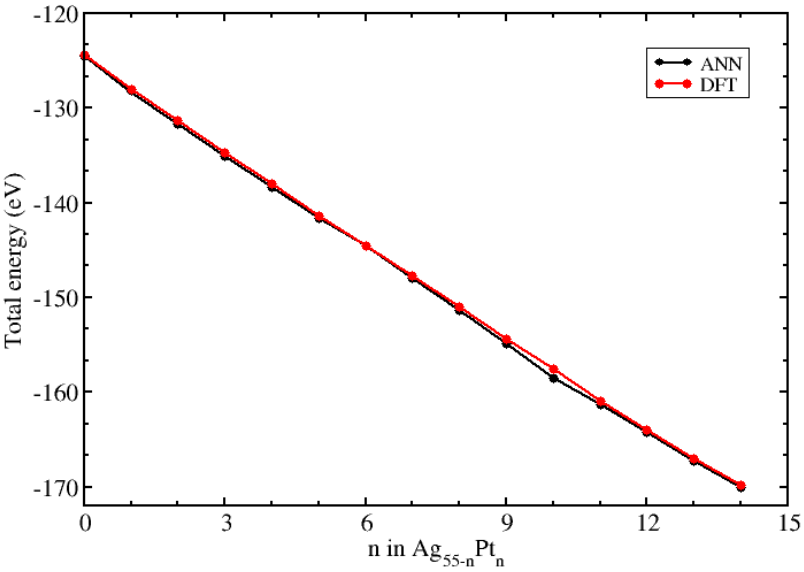

Figure 4.5: Correlation plot of total energies of between ANN and DFT based method for $Ag55 - nPtn$ nanoalloys (n = 0–14).

4.3.2 Global Optimization of Ag-Pt Nanoalloys using ANN-based Potential

In this study, I employ the ANN-based potential for Ag-Pt nanoalloys to perform MD simulations to investigate the PES of $Ag_{55-n}Pt_n$ for n = 1–14. These simulations ran for a total of 1.5 million time steps with a step size of 0.1 fs for a range of temperatures from 100 to 700 K. Several trajectories have been constructed by running the simulations using different random initial configurations. For each simulation, the structure for every 5000 MD steps has been quenched using the L-BFGS local optimization method [112].

A 55-atom $Ag_{55-n}Pt_n$ nanoalloys are core-shell structures that adopt Ih shape in their lowest energy isomers, as shown in Figure 4.6. Furthermore, to check the stability of the lowest energy isomers at elevated temperatures, MD simulations are performed for a range of temperatures from 100 to 950 K, starting from the lowest energy isomer for all the compositions. It has been observed that the lowest-energy isomers are the dominant isomers even at elevated temperatures for all the compositions. The energies obtained using the ANN potential for the core-shell Ih structures $Ag_{55-n}Pt_n$ are identical to those obtained using the DFT method, as shown in Figure 4.5. According to the ANN-based structure of Ag_mPt_n nanoalloys, the Pt atoms are found to primarily favour core positions in the lowest energy isomers of $Ag_{55-n}Pt_n$ nanoalloys with n = 1–14. This preference is due to the fact that the metal atoms with greater cohesive energy in bulk tend to form strong bonds with each other and occupy core positions. To check this, I calculated the cohesive energy per atom (E_{coh}) for a pure M_n nanocluster using the following Eq. 4.1,

$$E_{coh} = E_t(M) - \frac{E_t(M_n)}{n} \tag{4.1}$$

where, $E_t(M)$ and $E_t(M_n)$ are the total energies of the metal atom and M_n nanocluster, respectively. From Eq. 4.1, the cohesive energy per atom of Pt_{55} is 4.88 eV, and that of Ag_{55} is 2.18 eV. In the case of n = 1, i.e., $Ag_{54}Pt_1$ structure, the Pt atom is found to be located at the centre of the core position while for n = 2 to 13 in $Ag_{55-n}Pt_n$ nanoalloys, Pt atoms are found to occupy various available core sites. However, for n= 14, since all the core sites are occupied by 13 Pt atoms, the 14^{th} Pt atom is forced to occupy a site that is located at the surface. The total energies of the lowest energy isomer of $Ag_{55-n}Pt_n$ nanoalloys are shown in Table 4.1. In $Ag_{41}Pt_{14}$, the surface Pt atom occupies the top of the vertex site in the lowest energy isomer, which is shown in Figure 4.6 (o).

4.3.3 Assessment of the Relative Stability of $Ag_{55-n}Pt_n$ Nanoalloys

(1) Excess energy: In order to conduct a comparative assessment of the relative stability of various compositions of $Ag_{55-n}Pt_n$ nanoalloys, I calculated the excess energy [210] (E_{exe}) which is given by following Eq. 4.2,

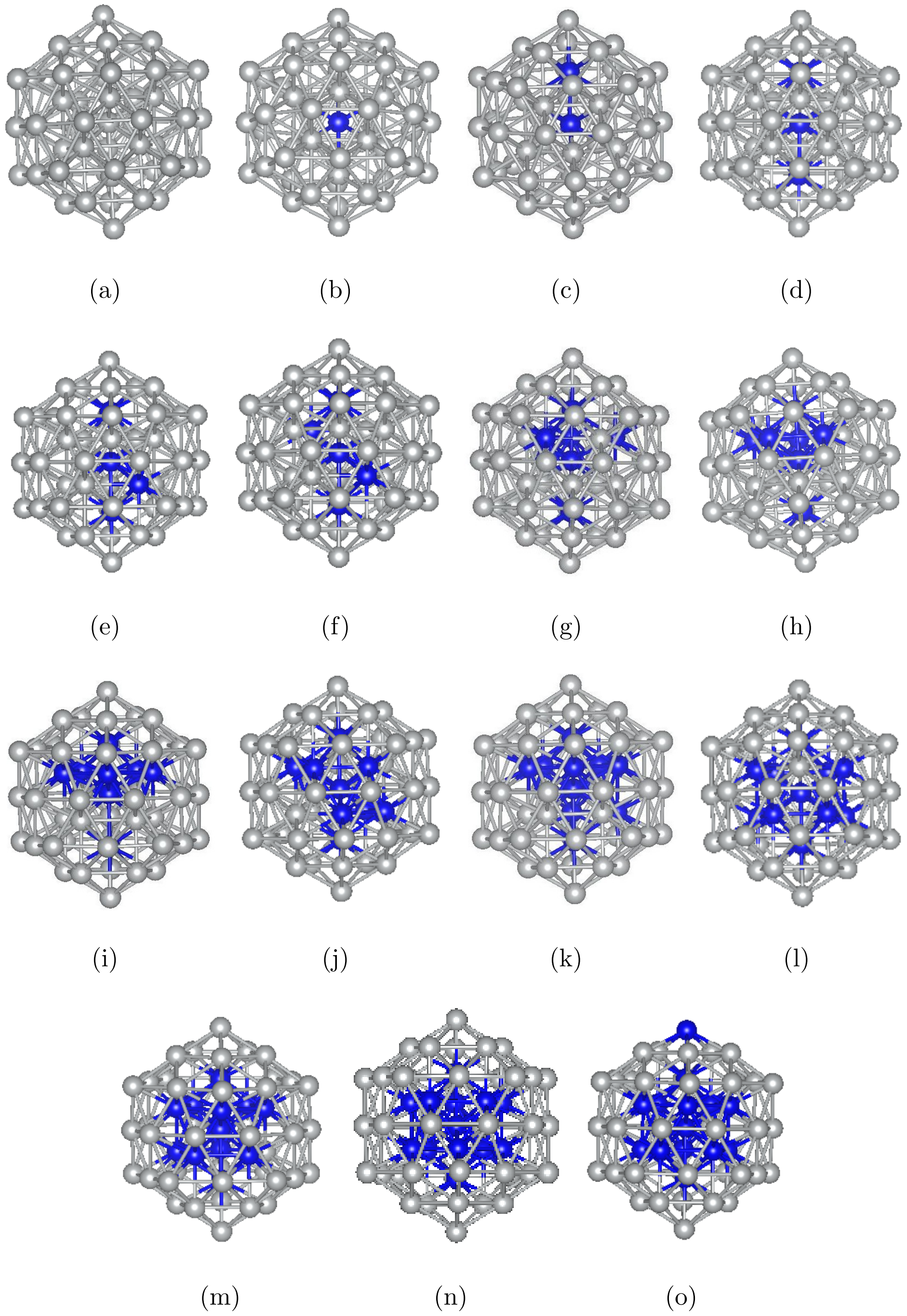
(a) (b) (c) (d)

(e) (f) (g) (h)

(i) (j) (k) (l)

(m) (n) (o)

Figure 4.6: Lowest energy isomers of $\text{Ag}_{55-n}\text{Pt}_n$ nanoalloys, where n = 0-14. Grey and blue represent Ag and Pt atoms, respectively.

$$\mathrm{E_{exe}} = \mathrm{E_{total}^{AgPt}} - \frac{(55-n)}{55}\mathrm{E_{total}^{Ag}} - \frac{n}{55}\mathrm{E_{total}^{Pt}} \tag{4.2}$$

In this Eq. 4.2, $\mathrm{E_{total}^{AgPt}}$ is the total energy of $Ag_{55-n}Pt_n$ composition, while $\mathrm{E_{total}^{Ag}}$ and $\mathrm{E_{total}^{Pt}}$ are the total energies of Ag_{55} and Pt_{55} nanoclusters, respectively. The variation of $\mathrm{E_{exe}}$ with the number of Pt atoms is shown in Figure 4.7. The presence of negative values in the excess energy implies favourable alloying for all the compositions, and it reveals that the $Ag_{42}Pt_{13}$ emerges as the most stable composition among all compositions of $Ag_{55-n}Pt_n$ nanoalloys, where n = 0-14. It is interesting to note that $\mathrm{E_{exe}}$ of $Ag_{41}Pt_{14}$ is only 0.1 eV higher in comparison to that of $Ag_{42}Pt_{13}$, whereas $\mathrm{E_{exe}}$'s of all the other compositions are greater than 0.2 eV in comparison to the most stable composition. From Figure 4.7, I observed an interest-

Table 4.1: Total energies of $Ag_{55-n}Pt_n$ nanoalloys where n= 0-14 predicted by ANN potential and DFT based method

System	ANN(eV)	DFT(eV)
Ag_{55}	-124.472	-124.418
$Ag_{54}Pt_1$	-128.339	-128.041
$Ag_{53}Pt_2$	-131.732	-131.291
$Ag_{52}Pt_3$	-135.106	-134.701
$Ag_{51}Pt_4$	-138.340	-137.986
$Ag_{50}Pt_5$	-141.606	-141.428
$Ag_{49}Pt_6$	-144.545	-144.533
$Ag_{48}Pt_7$	-147.899	-147.753
$Ag_{47}Pt_8$	-151.357	-150.959
$Ag_{46}Pt_9$	-154.874	-154.415
$Ag_{45}Pt_{10}$	-158.460	-158.504
$Ag_{44}Pt_{11}$	-161.323	-160.958
$Ag_{43}Pt_{12}$	-164.228	-163.934
$Ag_{42}Pt_{13}$	-167.261	-167.032
$Ag_{41}Pt_{14}$	-169.991	-169.770

ing trend in excess energies as I move from Ag_{55} to $Ag_{41}Pt_{14}$, the excess energy required to replace a single Ag atom from the core by a Pt atom is roughly -1.1 eV. This is the difference in excess energies while I move from Ag_{55} to $Ag_{54}Pt_1$. The difference in excess energies is roughly -0.6 eV for every additional replacement of Ag atom by a Pt atom upto $Ag_{46}Pt_9$. Beyond $Ag_{46}Pt_9$, there is almost negligible change in excess energies. So, it is very favourable to substitute a central Ag atom with a Pt atom. It is favourable to substitute the next 9 Ag atoms in the core with Pt atoms, but only marginally favourable (or unfavourable) for further substitutions. I observed a similar trend in the flattening of excess energy close to the minimum value that has already been reported in the literature [46, 200, 210]. Such a trend may be attributed to the fact that as the size of the Pt core increases, the cohesion between the Pt atoms (which is greater than those of Ag atoms) gets saturated due to the newly added Pt atom moving away from a central core. Due to the reduction of the cohesion, additional Pt atoms move to surface sites, thereby reducing the excess energy.

(2) Composition-based stability: There is another way to check the stability of various compositions of $Ag_{55-n}Pt_n$ nanoalloys by calculating the energy difference between E_{dist} and E_{GM} of Ag_{55}, which gives the energy required to distort the GM of Ag_{55} from Ag-Pt nanoalloy. For E_{dist}, consider the global minimum of every composition, replace all the Pt atoms with Ag atoms, and do a single-point energy calculation. A large positive value would indicate a large strain associated with a substitution (unfavourable), and a small positive value would indicate little strain (favourable). The difference in energy is positive for all the Pt-substituted nanoalloys, as tabulated in Table 4.2. However, I observed that the energy difference is 0.45 eV, which indicates strain for the formation of $Ag_{54}Pt_1$ and reaches a maximum of 0.56 eV to replace all core Pt atoms with Ag atoms in the case of $Ag_{42}Pt_{13}$.

(3) Interaction energy: Another stability descriptor that can be considered to assess the relative stability of various compositions of $Ag_{55-n}Pt_n$ nanoalloys is the interaction energy (E_{int}). E_{int} is defined as

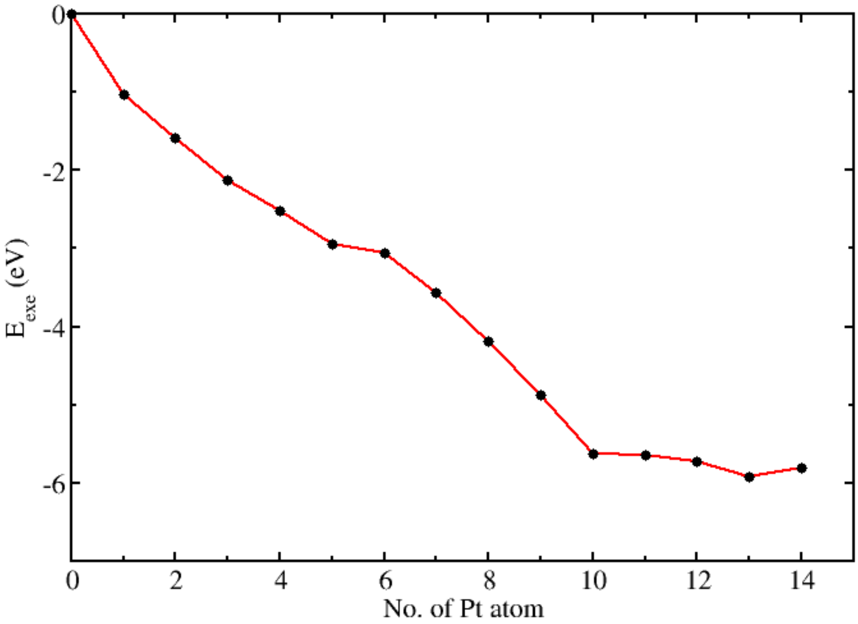

Figure 4.7: Plot of excess energy for $Ag_{55-n}Pt_n$ nanoalloys with number of Pt atoms.

the stabilization energy of $Ag_{55-n}Pt_n$ nanoalloys with respect to distorted core and distorted shell [211]. The structures of the distorted core and distorted shell are considered to be the same as the structures in the optimized $Ag_{55-n}Pt_n$ nanoalloys. E_{int} for core-shell $Ag_{55-n}Pt_n$ nanoalloys can be calculated by the following Eq. 4.3,

$$E_{int} = E_{\text{total}}(Ag_{55-n}Pt_n) - E^{\text{dis}}(\text{core}) - E^{\text{dis}}(\text{shell}) \tag{4.3}$$

where $E_{\text{total}}(Ag_{55-n}Pt_n)$ is total energy of core-shell $Ag_{55-n}Pt_n$ structure while, $E^{\text{dis}}(\text{core})$ and $E^{\text{dis}}(\text{shell})$ are energies of distorted core and distorted shell structures of the $Ag_{55-n}Pt_n$ nanoalloys, respectively. A negative E_{int} indicates that the formation of the core-shell structure is favourable in comparison to the distorted core and distorted shell structures. The variation of E_{int} with the number of atoms of Pt is shown in Figure 4.8. From this figure, it is evident that core-shell structure is favoured for all the com-

Table 4.2: The energy difference between E_{dist} and E_{GM} with respect to Pt-substituted nanoalloy.

Cluster	$E_{dist} - E_{GM}$
$Ag_{54}Pt_1$	0.4527
$Ag_{53}Pt_2$	0.4798
$Ag_{52}Pt_3$	0.5027
$Ag_{51}Pt_4$	0.5120
$Ag_{50}Pt_5$	0.5190
$Ag_{49}Pt_6$	0.5287
$Ag_{48}Pt_7$	0.5237
$Ag_{47}Pt_8$	0.5376
$Ag_{46}Pt_9$	0.5427
$Ag_{45}Pt_{10}$	0.5528
$Ag_{44}Pt_{11}$	0.5587
$Ag_{43}Pt_{12}$	0.5619
$Ag_{42}Pt_{13}$	0.5636
$Ag_{41}Pt_{14}$	0.5667

positions, which is akin to the trend obtained for E_{exe}. It also reveals that $Ag_{42}Pt_{13}$ nanoalloy is most stable and is closely followed by $Ag_{41}Pt_{14}$ nanoalloy, which is 0.1 eV higher in energy in comparison to $Ag_{42}Pt_{13}$ nanoalloy.

The following conclusion can be drawn from MD simulations and energetic analysis of all the compositions of $Ag_{55-n}Pt_n$ nanoalloys. For all the composition the core-shell Ih structures are dominant both at 0 K and also at elevated temperatures upto 950 K. Using the energy descriptors such as E_{exe} and E_{int} it is evident that $Ag_{42}Pt_{13}$ and $Ag_{41}Pt_{14}$ nanoalloys are the most stable compositions.

In the following sections, I will investigate the adsorption and activation characteristics of O_2 and CO molecules on core-shell $Ag_{55-n}Pt_n$ nanoalloys with n ranging from 0 to 14.

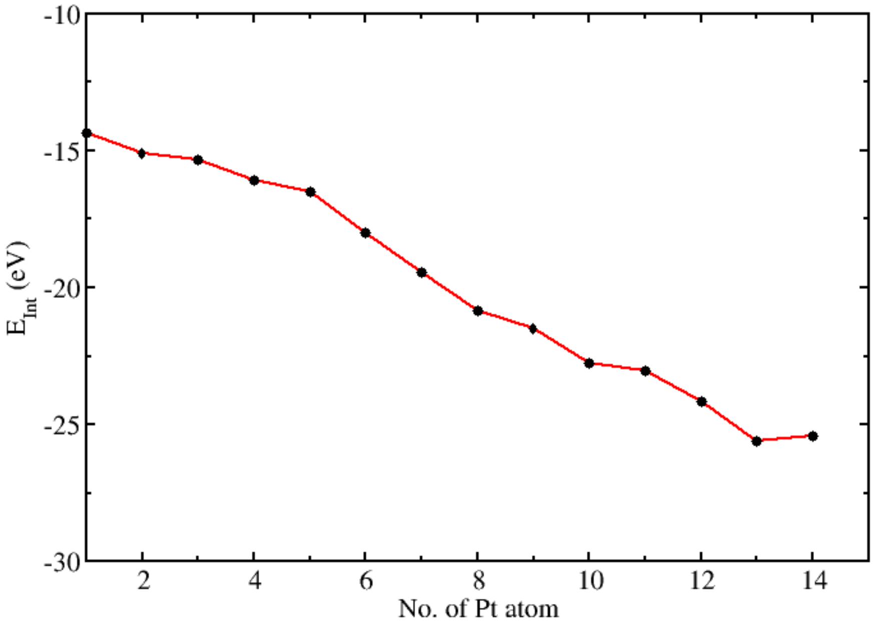

Figure 4.8: Plot of interaction energy for $Ag_{55-n}Pt_n$ nanoalloys with number of Pt atoms.

4.3.4 Adsorption and Activation of O_2

To investigate the adsorption of O_2 onto Ag-Pt nanoalloys, first I consider the most stable structures of various different compositions of $Ag_{55-n}Pt_n$ nanoalloys, as shown in Figure 4.6, and place an O_2 molecule at several possible nonequivalent sites of each nanoalloy, as shown in Figure 4.9. The Ih structure showcases a total of 20 identical triangular facets on its external surface, and each facet possesses two distinctive sites, namely the vertex and the edge. These facets offer seven potential adsorption sites (see Figure 4.9(b): T1 (atop the vertex), T2 (atop the edge), B1 (between a vertex and an edge), B2 (between two edges), H1 (within the hollow region defined by one vertex and two edges), H2 (within the hollow region defined by three edges), and H3 (where an O_2 molecule rotates by a small angle from its orientation at the H1 site, coordinating with one vertex and two edges, see Figure 4.10).

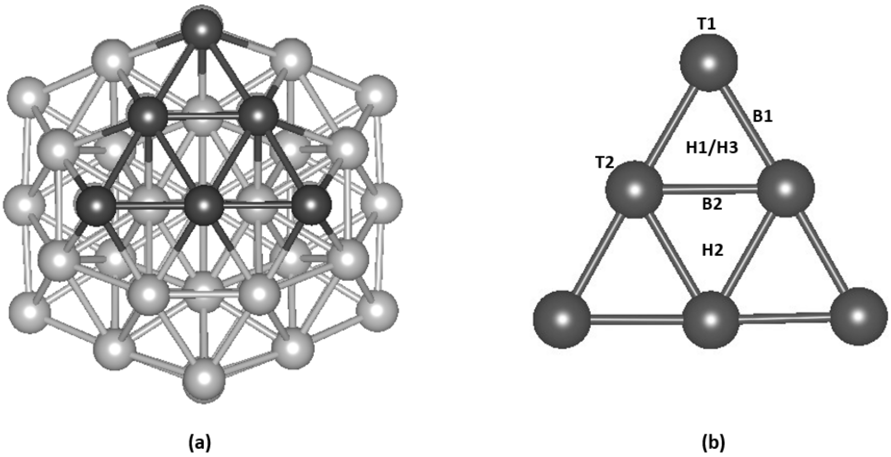

Figure 4.9: One of the 20 identical triangular facets on its external surface of core-shell structure for preferential adsorption sites.

In the literature survey, I found that O_2 is more likely to prefer adsorption at the bridge and hollow sites of 55-atom Ih structure. [206, 212]. Hence, to reduce the computational requirements, our focus is directed towards O_2 adsorption at the bridge or hollow sites only. To characterize the interaction between O_2 and $Ag_{55-n}Pt_n$ nanoalloys, I employed the adsorption energy E_{ads}, which is determined by using the Eq. 4.4 below,

$$E_{ads} = [E(\text{cluster} + O_2) - E(\text{cluster}) - E(O_2)] \tag{4.4}$$

where $E(\text{cluster}+O_2)$, $E(\text{cluster})$, and $E(O_2)$ correspond to the energies of the cluster-O_2 complexes, bare isomers of $Ag_{55-n}Pt_n$, and the isolated O_2 molecule, respectively. It is important to mention that a higher negative value of E_{ads} calculated using Eq. 4.4 indicates a stronger interaction between the cluster and O_2 molecule.

The adsorption energies of O_2 and CO on the nanoalloy surfaces were calculated using DFT as implemented in the VASP package [199]. The PAW method [160] was employed to describe the interaction between core and valence electrons. The exchange-correlation energy was treated within the GGA using the Perdew–Burke–Ernzerhof PBE functional. A plane-wave energy cutoff of 400 eV was used for the expansion of the wavefunctions. Electronic self-consistency was achieved with an energy convergence threshold of 1×10^{-5} eV. Structural relaxations were performed until the forces on all atoms were less than 0.01 eV/Å. A Gamma-point ($1 \times 1 \times 1$) k-point mesh was applied to sample the Brillouin zone.

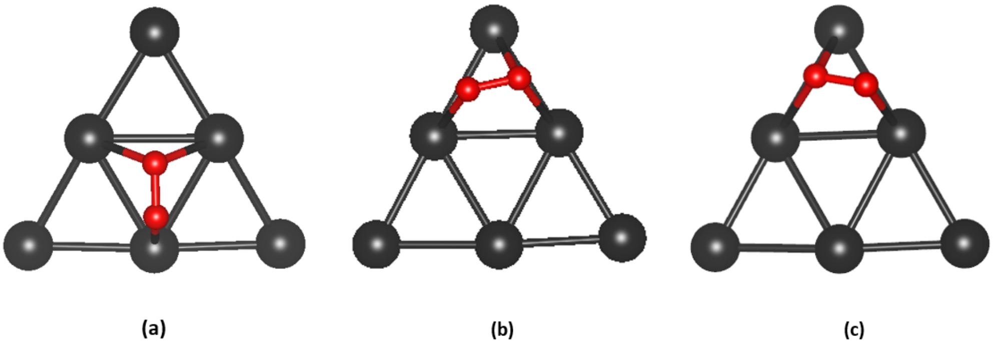

Figure 4.10: (a) H2, (b) H3, and (c) H3' adsorption sites of O_2 on the external surface of the core-shell structure.

Furthermore the adsorption of O_2 on $Ag_{55-n}Pt_n$ nanoalloys, five nonequivalent bridge sites namely B1 and B2 and hollow sites H1, H2 and H3 are considered. For all these sites, the O_2 adsorption energies have been calculated by using Eq. 4.4 and the corresponding values are compiled in Table 4.3. The values highlighted in bold indicate the preferred adsorption sites for O_2. In this table, I also tabulate the O-O bond lengths of the adsorbed O_2. It is noted that for all compositions of $Ag_{55-n}Pt_n$ nanoalloys, except for the $Ag_{41}Pt_{14}$ nanoalloy, hollow sites H2 or H3 are preferred as their energies are lower in comparison to other sites. From Table 4.3, it is apparent that from n = 0 to n = 5 in $Ag_{55-n}Pt_n$ nanoalloys, the most preferable site for O_2 adsorption is the hollow site (H2), as shown in Figure 4.11(a) to Figure 4.11(f) . In the case of n = 0, a 55-atom pure Ag nanocluster (Ag_{55}), and for $Ag_{54}Pt_1$, the adsorption energy of O_2 on the H2 site is -0.30 and -0.33 eV, respectively. For this site, it is observed that O-O bond length undergoes an elongation of 0.15 Å in comparison to the bond length of the free O_2 molecule (d_{O-O} = 1.23 Å). As I increased the alloying proportion of Pt atom in $Ag_{55-n}Pt_n$ nanoalloys, i.e., as I go from n = 2 to 5, the most favoured site for the O_2 adsorption continues to be the H2 site. However, for n = 6 to 13 on the $Ag_{55-n}Pt_n$ nanoalloys, the maximum adsorption energies for O_2 are found to be at the H3 site, as

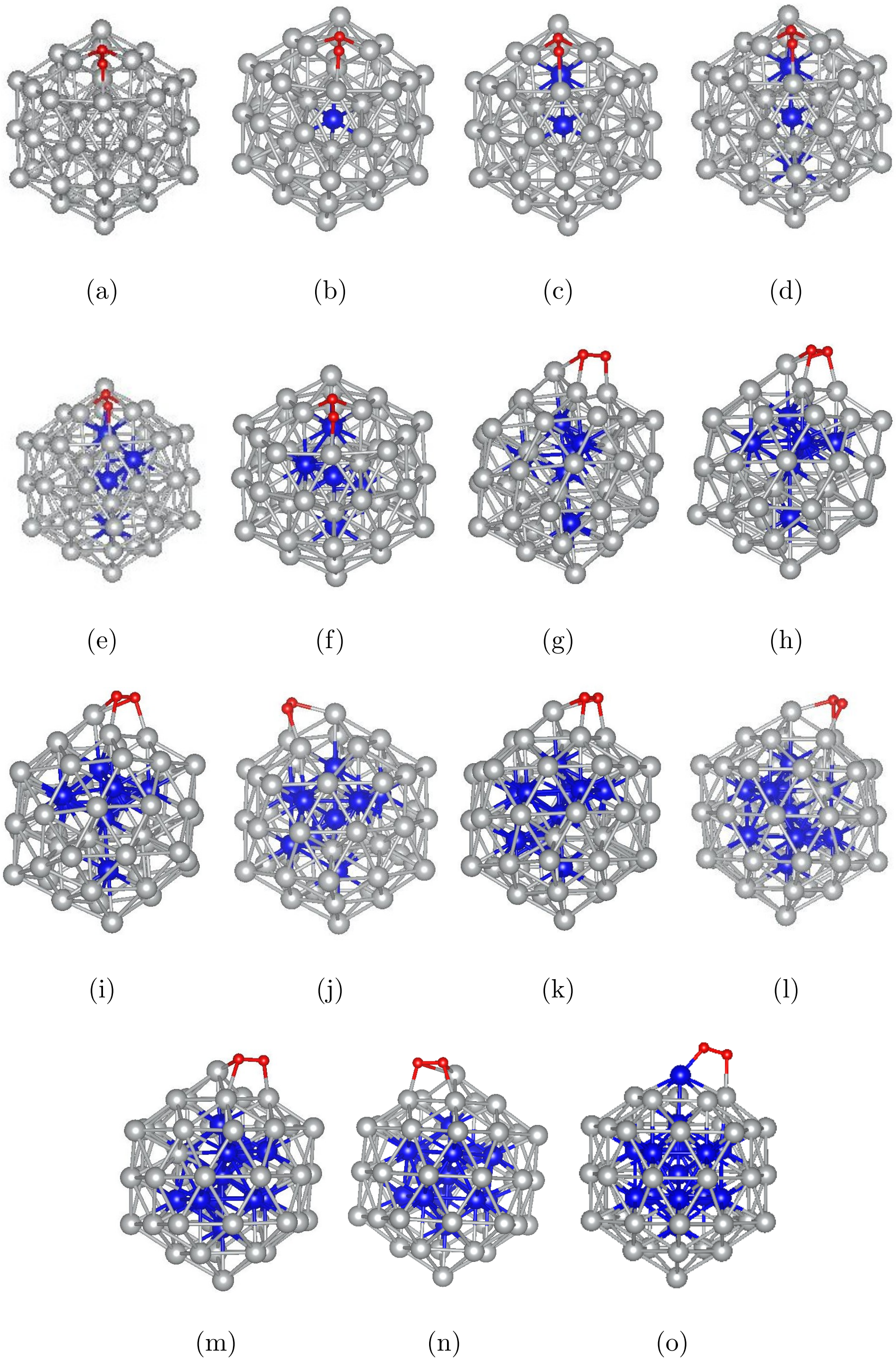

(a) (b) (c) (d)

(e) (f) (g) (h)

(i) (j) (k) (l)

(m) (n) (o)

Figure 4.11: Most preferred O_2 adsorption configuration on $Ag_{55-n}Pt_n$ nanoalloys, where n varies from 0 to 14. Ag, Pt, and O atoms are symbolized by grey, blue, and red balls, respectively.

Table 4.3: Adsorption energy, bond length of the O_2 molecule and charges of the preferred sites for $Ag_{55-n}Pt_n - O_2$ nanoalloy-O_2 complexes.

Cluster	$\mathbf{E_{ads}}$**(eV)**	$\mathbf{d_{O\text{-}O}}$(Å)	**Charges**(e)
Ag_{55}	**-0.30** (H2)	**1.38**	-0.026
$Ag_{54}Pt_1$	**-0.33** (H2)	**1.38**	-0.028
$Ag_{53}Pt_2$	**-0.33** (H2)	**1.37**	-0.031
$Ag_{52}Pt_3$	**-0.34** (H2)	**1.38**	-0.029
$Ag_{51}Pt_4$	**-0.34** (H2)	**1.35**	-0.027
$Ag_{50}Pt_5$	**-0.30** (H2)	**1.38**	-0.024
$Ag_{49}Pt_6$	**-0.27** (H3)	**1.38**	-0.027
$Ag_{48}Pt_7$	**-0.36** (H3)	**1.41**	-0.030
$Ag_{47}Pt_8$	**-0.34** (H3)	**1.41**	-0.029
$Ag_{46}Pt_9$	**-0.35** (H3)	**1.40**	-0.031
$Ag_{45}Pt_{10}$	**-0.31** (H3)	**1.41**	-0.029
$Ag_{44}Pt_{11}$	**-0.29** (H3)	**1.39**	-0.028
$Ag_{43}Pt_{12}$	**-0.36** (H3)	**1.39**	-0.028
$Ag_{42}Pt_{13}$	**-0.41** (H3)	**1.40**	-0.027
$Ag_{41}Pt_{14}$	**-1.02** (B1)	**1.36**	-0.318

depicted in Figure 4.11(g) to 4.11(n). For n = 6, i.e., $Ag_{49}Pt_6$ nanoalloy, the adsorption energy of O_2 is -0.27 eV at the preferred H3 site shows weak adsorption when compared to other highly adsorbed structures. In the case of nanoalloys such as $Ag_{48}Pt_7$, $Ag_{47}Pt_8$, $Ag_{46}Pt_9$, $Ag_{45}Pt_{10}$, $Ag_{44}Pt_{11}$ and $Ag_{43}Pt_{12}$, the adsorption energies of -0.36, -0.34, -0.35, -0.30, -0.29 and -0.36 eV, respectively. In all of these cases, the bond length of O_2 is nearly 1.4 Å. Furthermore, in the case of the $Ag_{42}Pt_{13}$ nanoalloy, it has been found that the adsorption of O_2 is equally prominent at both the H1 and H3 sites, resulting in identical adsorption energy of approximately -0.41 eV for both of these sites. In this composition, a new conformer identical to the one at the H3 site can be obtained by rotating the O_2 molecule on the adsorbed H3 site by 180 degrees, which I named as $H3'$. The adsorption energies of both H3 and $H3'$ are found to be the same.

It is important to note that adsorption of O_2 is favourable on the hollow sites in which core Pt atoms are directly bonded with surface Ag atoms that are involved in forming the hollow sites on the facets. So, I considered only those facets in which the core Pt atom is directly bonded to Ag atoms that form the hollow site on the surface and ignore all other facets. In the case of $Ag_{54}Pt_1$ and $Ag_{42}Pt_{13}$, the hollow sites on all 20 facets are chemically equivalent. In the case of $Ag_{53}Pt_2$, the 2^{nd} Pt atom is directly bonded to Ag atoms on the surface that forms the H2 hollow site, leading to 5 chemically equivalent facets. For $Ag_{52}Pt_3$, I got 10 facets that are chemically equivalent, in which core Pt atoms are directly bonded to Ag atoms on the surface hollow. For compositions from $Ag_{51}Pt_4$ to $Ag_{43}Pt_{12}$ I got chemically non-equivalent facets when the core Pt atoms are directly bonded to surface Ag atoms. I found that the adsorption of O_2 is favourable on the hollow sites, in which the magnitude of charges is maximum. To begin with, I calculated the charges on individual atoms on the cluster using Bader charge analysis [203]. In order to find the most favourable hollow site for adsorption of O_2, I sum the charges on the Ag atoms that form the hollow site in which the core Pt atom is directly bonded. Finally, I chose the hollow site that has the maximum value of the summed charges. I tabulate the summed charges for the most favourable hollow sites for every composition in Table 4.3

From the above discussion, it can be concluded that by alloying Pt in a bare Ag_{55} nanocluster, there is no substantial change in the adsorption energy of O_2 on $Ag_{55-n}Pt_n$ nanoalloys. On the bare Ag_{55} nanocluster, the adsorption energy for O_2 is -0.30 eV, and this value is -0.41 eV in the case of the $Ag_{42}Pt_{13}$ nanoalloy. To enhance the role of Pt, it would be more advantageous if the Pt atom were located at the surface site of Ag-Pt nanoalloys. As discussed above, for $Ag_{42}Pt_{13}$, the Pt atoms have exhausted all the thirteen core sites. Hence, the 14^{th} Pt can only be accommodated at the surface sites instead of going to core sites. I have investigated the adsorption of O_2 on the most stable $Ag_{41}Pt_{14}$ nanoalloy in which the 13 Pt atoms are present in the core region and one Pt atom is located on the surface site. Furthermore, the most favourable position for this 14^{th} Pt atom on the surface is the vertex site. In this case, I find that the B1 site is favoured for the O_2 molecule adsorption, as shown in Figure 4.11(o). The adsorption energy of O_2 on the B1 site is -1.02 eV, whereas at the H1 site, it is -0.86 eV. On the other hand, the adsorption of O_2 is weakest at the H2 site. The O-O bond length at the B1 site is 1.36 Å, while the Pt-O and Ag-O bond lengths are 1.95 Å and 2.28 Å, respectively. From these results, it can be concluded that the Pt atom present on the surface of the core-shell $Ag_{41}Pt_{14}$ structure exhibits stronger adsorption of the O_2 molecule in comparison to the Pt atom present in the core. The sum of charges of only those atoms which are involved in a particular adsorption site (H2, H3 or B1) is tabulated in Table 4.3 for all the compositions. These findings reveal that the sum of charges on site B1 in $Ag_{41}Pt_{14}$, which is the preferred site for O_2 adsorption then the sum of charges at the H2/H3 sites of $Ag_{55-n}Pt_n$ with n = 1–13. Therefore, I expected comparatively more charge transfer between $Ag_{41}Pt_{14}$ and O_2 molecule, resulting in stronger adsorption of O_2 molecule on this nanoalloy.

4.3.4.1 d-band Center Calculation

The stronger adsorption of O_2 on $Ag_{41}Pt_{14}$ in comparison to all other compositions considered in this study can be further understood in terms of the electronic structure of bare Ag-Pt nanoalloys. It has been shown that the centre of the d-band relative to Fermi energy plays an important role in the reactivity of these nanoalloys. The increase in adsorption energy of the nanoalloys can be directly correlated to the shift in the d-band centre to higher energies. The d-band centre(the first moment of d-DOS distribution) developed by Nørskov and co-workers [213] is given by the following Eq. 4.5,

$$E_d = \frac{\int_{-\infty}^{\infty} (E - E_{HOMO})\, P_d(E)\, dE}{\int_{-\infty}^{\infty} P_d(E)\, dE} \tag{4.5}$$

where E_d is the d-band centre, the energy of HOMO of nanoalloy is denoted by E_{HOMO}, and the partial density of states (PDOS) of d-orbitals in the

Table 4.4: d-band center value for all compositions of $Ag_{55-n}Pt_n$ nanoalloys with n = 1-14.

Cluster	**d-band center (E_d)**
$Ag_{54}Pt_1$	-4.223
$Ag_{53}Pt_2$	-3.769
$Ag_{52}Pt_3$	-3.787
$Ag_{51}Pt_4$	-3.734
$Ag_{50}Pt_5$	-3.725
$Ag_{49}Pt_6$	-3.681
$Ag_{48}Pt_7$	-3.677
$Ag_{47}Pt_8$	-3.628
$Ag_{46}Pt_9$	-3.607
$Ag_{45}Pt_{10}$	-3.543
$Ag_{44}Pt_{11}$	-3.531
$Ag_{43}Pt_{12}$	-3.462
$Ag_{42}Pt_{13}$	-3.445
$Ag_{41}Pt_{14}$	-3.343

nanoalloy is denoted by $P_d(E)$. Using the above formula, I have calculated the E_d for all the compositions considered in this study and values of E_d are tabulated in Table 4.4. From Table 4.4, it is evident that E_d values shift to higher energies as I increase the number of Pt atoms. It is also evident that in $Ag_{41}Pt_{14}$, where the 14^{th} Pt atom occupies the surface site of nanoalloy, the E_d value is closest to the Fermi energy and therefore is more reactive to O_2 molecule in comparison to nanoalloys in which Pt atoms are present in the core sites.

4.3.4.2 Charge Transfer Analysis

To understand the mechanism of O_2 activation on Ag-Pt nanoalloys, I consider the transfer of charge between the nanoalloy and the O_2 molecule. By employing Bader charge analysis [203], I have assessed the charges on chemisorbed O_2 within the nanoalloy-O_2 complex, as presented in Table

4.5 along with O-O bond distance ($d_{\text{O-O}}$). From Table 4.5, I found that the charge transfer from $Ag_{55-n}Pt_n$ to O_2 molecule results in an elongation of bond length of O_2 molecule (1.36 - 1.40 Å) as compared to that of free O_2 molecule (1.23 Å). It is also evident that the charge transferred onto the O_2 molecule is proportional to the elongation of bond length of O_2 molecule. I showed this by using a correlation plot in Figure 4.12 between the charge on the O_2 molecule and the elongation of bond length of O_2 molecule with correlation coefficient, $R^2 = 0.78$.

Table 4.5: Total Charge on O_2 and the bond length in $Ag_{55-n}Pt_nO_2$ Complex.

Cluster	**Total charge on O_2(e)**	**$d_{\text{O-O}}$(Å)**
Ag_{55}	-0.78	1.38
$Ag_{54}Pt_1$	-0.78	1.38
$Ag_{53}Pt_2$	-0.73	1.37
$Ag_{52}Pt_3$	-0.77	1.38
$Ag_{51}Pt_4$	-0.66	1.35
$Ag_{50}Pt_5$	-0.76	1.38
$Ag_{49}Pt_6$	-0.76	1.38
$Ag_{48}Pt_7$	-0.83	1.41
$Ag_{47}Pt_8$	-0.83	1.41
$Ag_{46}Pt_9$	-0.79	1.40
$Ag_{45}Pt_{10}$	-0.80	1.41
$Ag_{44}Pt_{11}$	-0.76	1.39
$Ag_{43}Pt_{12}$	-0.75	1.39
$Ag_{42}Pt_{13}$	-0.80	1.40
$Ag_{41}Pt_{14}$	-0.60	1.36

For all the compositions, I observed from Table 4.5 that the charge accumulation on chemisorbed O_2 resulting in elongation of its bond lengths (1.36 - 1.40 Å) as compared to that of free O_2 molecule (1.23 Å). From Table 4.5, it is also evident that the elongation of bond-length of O_2 molecule is proportional to the charge transferred onto the O_2 molecule.

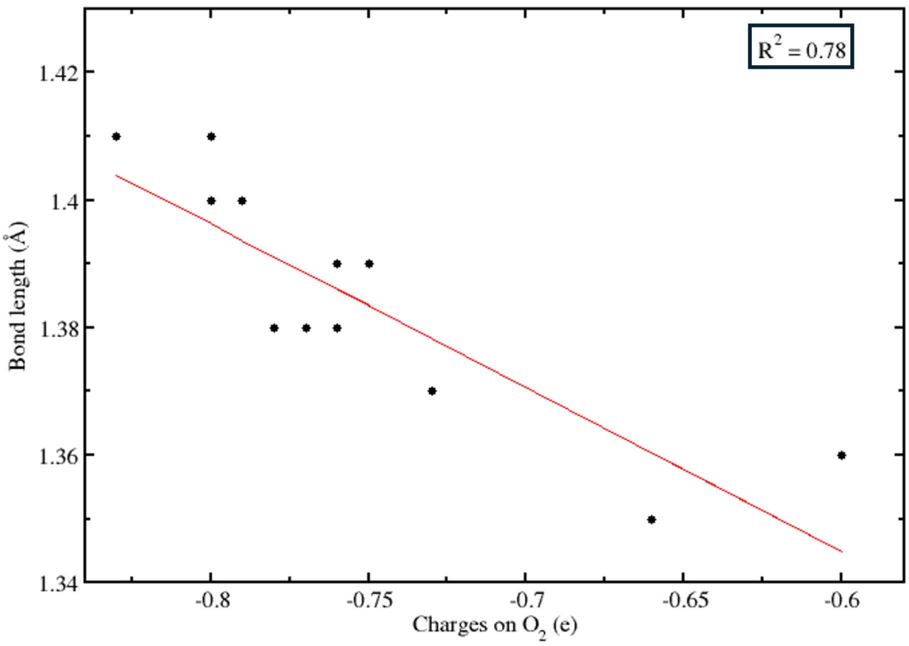

Figure 4.12: Plot shows a correlation between charges on O_2 with respect to the bond length of O_2.

4.3.4.3 Adsorption of Multiple O_2 Molecules on $Ag_{41}Pt_{14}$ Nanoalloy

Furthermore, I studied the adsorption of a second O_2 molecule onto the surface of $Ag_{41}Pt_{14}$ nanoalloy in the presence of an already adsorbed O_2 molecule. The presence of the first adsorbed O_2 molecule can influence the adsorption of the second O_2 molecule depending on the surface coverage and available adsorption sites. In this context, I have already determined the most stable adsorption site for a single O_2 molecule on $Ag_{41}Pt_{14}$, and this specific site remains constant as I proceed to identify the optimal adsorption site for the next O_2 molecule. I searched all possible sites for the adsorption of the second O_2 molecule and found that the adsorption of the second O_2 molecule is preferred at the bridge position on the same surface Pt atom but non-adjacent to the first O_2 as is shown in Figure 4.13. This preference is attributed to the higher negative charge of the surface Pt atom in comparison to the surface Ag atoms. The adsorption energy of the second O_2 is found to be -0.85 eV, and the bond length of both O_2

molecules is 1.33 Å. I observed a slight reduction in the bond length of the first O_2 molecule, indicating a strengthening of the Pt-O_2 interaction.

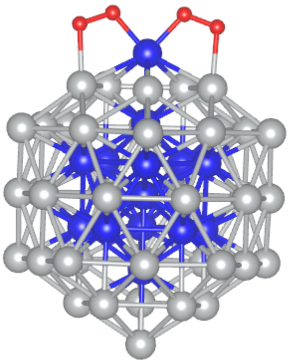

Figure 4.13: The most favourable adsorption site for second O_2 molecule on $Ag_{41}Pt_{14}$ nanoalloy.

4.3.5 Adsorption of CO on Ag-Pt Nanoalloys

I have also investigated the adsorption of CO molecule onto $Ag_{55-n}Pt_n$ nanoalloys, where n = 0–14. In the literature survey, it was found that the CO prefers to get adsorbed in the top vertex (T1) site only. It should be noted that placing a CO molecule, in which carbon atoms bind with the metal atom at the T1 site of the nanoalloy, leads to a stable configuration for all the compositions considered in this study. The corresponding adsorption energy is the highest at this site, as illustrated in Table 4.6. From Table 4.6, the adsorption energy of CO is minimum (-0.46 eV) for pure Ag_{55} nanocluster and the C-O bond length is 1.15 Å. As I increase the alloying percentage of the Pt atom in the Ag nanocluster, the adsorption energy increases. In the case of $Ag_{54}Pt_1$, the adsorption energy of CO is found to be -0.47 eV, which is only a slight increment in adsorption energy than pure Ag nanocluster. It is because in $Ag_{54}Pt_1$, the Pt atom is positioned in the centre of the core and not directly coordinated with the surface Ag atoms.

From n= = 2–13, the T1 site, in which the surface Ag atom is directly bonded to the core Pt atom, exhibits maximum adsorption energy in com-

Table 4.6: The adsorption energy and bond length of the CO molecule on preferred sites of $Ag_{55-n}Pt_n$ nanoalloys where n = 0-14.

Cluster	$\mathbf{E_{ads}}$ (eV)	$\mathbf{d_{C-O}}$(Å)
Ag_{55}	-0.46	1.15
$Ag_{54}Pt_1$	-0.47	1.15
$Ag_{53}Pt_2$	-0.55	1.15
$Ag_{52}Pt_3$	-0.54	1.15
$Ag_{51}Pt_4$	-0.53	1.15
$Ag_{50}Pt_5$	-0.53	1.15
$Ag_{49}Pt_6$	-0.51	1.15
$Ag_{48}Pt_7$	-0.52	1.15
$Ag_{47}Pt_8$	-0.52	1.15
$Ag_{46}Pt_9$	-0.53	1.15
$Ag_{45}Pt_{10}$	-0.54	1.15
$Ag_{44}Pt_{11}$	-0.55	1.15
$Ag_{43}Pt_{12}$	-0.56	1.15
$Ag_{42}Pt_{13}$	-0.58	1.15
$Ag_{41}Pt_{14}$	-2.48	1.17

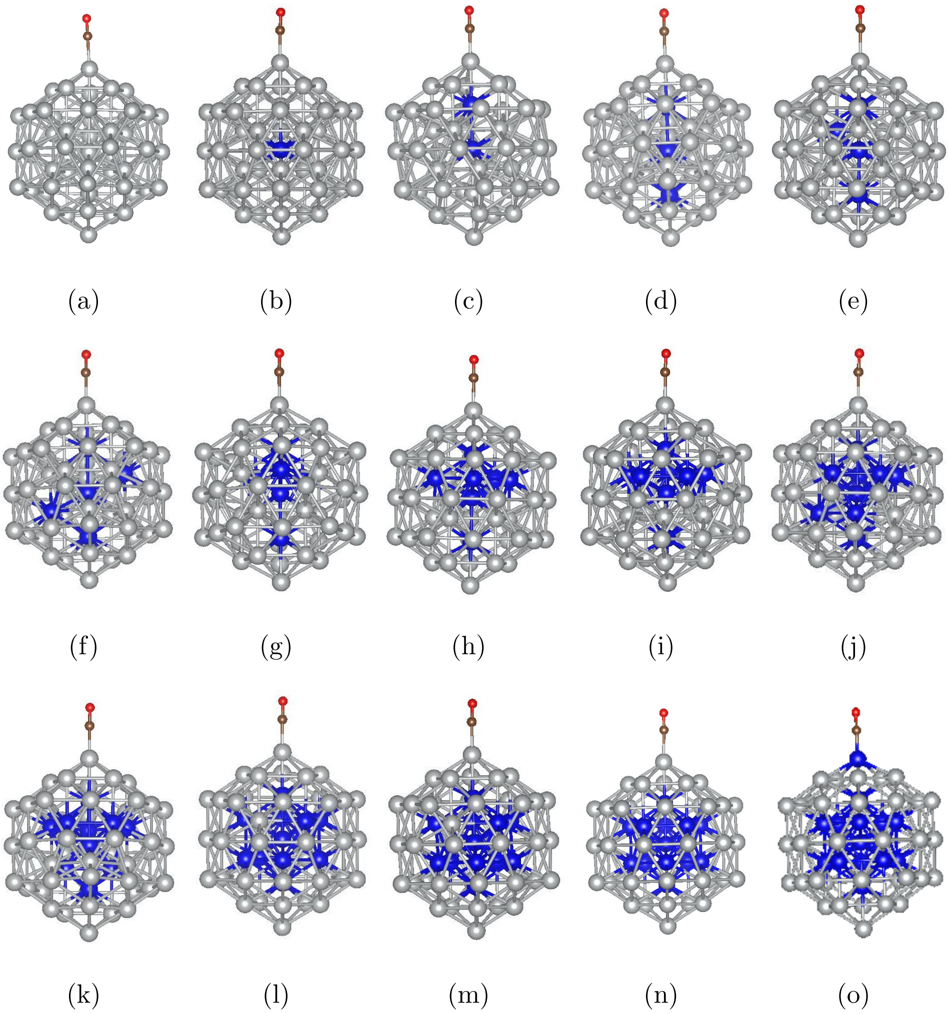
(a) (b) (c) (d) (e)

(f) (g) (h) (i) (j)

(k) (l) (m) (n) (o)

Figure 4.14: Most preferred CO adsorption configuration on $Ag_{55-n}Pt_n$ nanoalloys, where n varies from 0 to 14. Ag, Pt, C and O atoms are symbolized by grey, blue, brown, and red balls, respectively.

parison to other T1 sites where surface Ag atoms are directly bonded to core Ag atoms. The $Ag_{42}Pt_{13}$ nanoalloy, which has a perfect core-shell structure, is most favourable for CO adsorption among all other $Ag_{55-n}Pt_n$ nanoalloys in which Pt atoms are in the core. For n = 14, i.e., $Ag_{41}Pt_{14}$, the CO adsorption is strongest (with adsorption energy = -2.48 eV) among all the other compositions because CO adsorbs strongly to the surface Pt atom in comparison to the surface Ag atom, as shown in Figure 4.14(o). This is also evident from the elongation of the bond length of chemisorbed CO (1.17 Å) in comparison to the bond length of bare CO molecules (1.14 Å). The CO adsorbed lowest energy isomers of $Ag_{55-n}Pt_n$ nanoalloys are shown in Figure 4.14.

4.4 Summary

In this work, I have used ANN-based IAP to predict both energy and forces by fitting the DFT data for Ag-Pt nanoalloys. I have used ANN-based potential to carry out global optimization for 55 atom core-shell Ag-Pt nanoalloys. It is found that the lowest energy structure of $Ag_{55-n}Pt_n$ (where n= 0–14) nanoalloys are the core-shell structure in which Pt atoms occupy the core site and Ag atoms occupy the surface sites. However, for $Ag_{41}Pt_{14}$ nanoalloy, all the core sites are occupied by Pt atoms; hence, the 14th Pt atom is located at the vertex site on the surface of the core-shell structure. I have studied the relative stability of $Ag_{55-n}Pt_n$ nanoalloys by using excess energy and interaction energy calculation. I have found that the Ih $Ag_{42}Pt_{13}$ with core-shell structure is relatively most stable isomer among various $Ag_{55-n}Pt_n$ nanoalloys. I have investigated the adsorption of O_2 and CO molecules on core-shell $Ag_{55-n}Pt_n$ nanoalloys using DFT calculation. I have found that hollow sites are the preferred sites for O_2 adsorption in $Ag_{55-n}Pt_n$ clusters for n = 0–13. However, for $Ag_{41}Pt_{14}$, where the Pt atom is located on the surface of the core-shell structure, the adsorption of O_2 is the strongest at the bridge site. By examining the charge transfer between nanoalloys and O_2 molecules, I found the charge accumulation on O_2, which is responsible for the activation of the bond length of O_2 molecule. In the case of the CO adsorption study, I find that the adsorption of CO is higher on the top vertex site in $Ag_{55-n}Pt_n$ nanoalloys. However, $Ag_{41}Pt_{14}$ has the strongest adsorption and activation among all the other compositions. This study will help us to understand the reactivity of small gas molecules such as O_2 and CO on Ag-Pt nanoalloys towards CO oxidation reaction, which will be the focus of our study in the future. .

Chapter 5

Prediction of the Polarizability for Gold Nanoclusters

5.1 Introduction

In the previous chapters, I employed an ANN-based IAP to fit the PES of Ag-Pt nanoalloys, allowing us to accurately predict both the energy and its first-order derivative with respect to cartesian coordinates. We also studied the adsorption and activation of gas molecules on Ag-Pt nanoalloys understanding their catalytic properties. This chapter transitions to calculating static polarizability using ML methods to understand the physical properties of nanoclusters. The polarizability of metal nanoclusters holds significant importance as it directly characterizes their linear response to an external electromagnetic field, which in turn influences several of their physical and chemical properties. These unique properties make gold nanoclusters highly valuable for applications in optoelectronics, nanocatalysis, and medical fields. [91]. Nanoclusters made of gold atoms occupy a prime place in the field of atomic and molecular clusters due to their rich and interesting electronic, chemical, and optical properties. For instance, the optical response properties of gold nanoclusters play a crucial role in nano-photonic and optoelectronic applications [32, 34, 35]. Despite the importance of these properties, only a few studies have explored the prediction of response properties, such as polarizability or dipole moments, of various materials and organic molecules using ML methods. These investigations have employed a range of traditional ML models to predict the electric response properties [147, 152, 156, 214–216]. In this study, I propose to employ a spherical harmonic descriptor with ANN to predict both the isotropic polarizability (α_{iso}) and anisotropy in polarizability ($\Delta\alpha$) of gold nanoclusters describing their local atomic environment. The descriptor employed in the present work encompasses a Gaussian radial function and an angular function as a power spectrum or bispectrum function, providing a thorough representation of the local environment. Additionally, I extend the application of this descriptor to include GPR and KRR-based ML algorithms for polarizability calculations. It has been found that the ANN model with higher-order invariants like bispectrum is highly efficient in predicting polarizability (both isotropic and anisotropic) as compared to other ML models.

5.2 Computational Details

Descriptors: The atomic environment descriptors consist of 9 radial functions given by Eq. 2.55 and 15 bispectrum coefficients as given in Eq. 2.62 and 2.63. As discussed in Chapter 2, the parameters l_1 and l_2 vary from 0 to 4, while l ranges from $|l_1 - l_2|$ to $|l_1 + l_2|$. This results in a total of 35 possible combinations, from which 15 coefficients are selected based on a bicoherence value ranging from 0.4 to 1.0. The c_{lm} coefficient is provided in Eq. 2.60.

When utilizing the power spectrum coefficients, the atomic environment descriptors consist of 9 radial functions (Eq. 2.55) and 50 power spectrum coefficients (Eq. 2.61). For the ANN model, each of the two hidden layers contains 30 neurons, leading to an output layer with two nodes. The first output corresponds to α_{iso}, and the second corresponds to $\Delta\alpha$, as shown in Figure 5.1. Weights were optimized using both GEKF [113, 217, 218] and Adam optimizers [117]. I denote Adam optimizer as

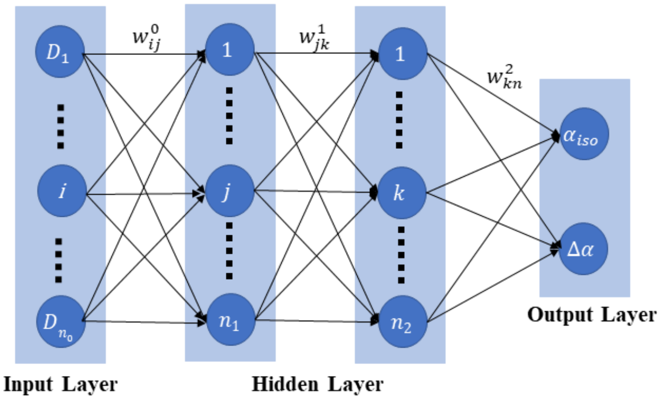

Figure 5.1: ANN architecture for polarizabilities prediction.

ANN-Adam and GEKF as ANN-Kalman in the remainder of the chapter. In addition to ANN, the GPR [219] and KRR [105] models were implemented with the Adam optimizer using the scikit-learn library [220]. In the present work, the polarizability of gold nanoclusters has been estimated by different metrics such as RMSE (Eq. 5.1), mean absolute error (MAE) (Eq. 5.2), mean squared error (MSE) (Eq. 5.3), and mean absolute percentage error (MAPE) (Eq. 5.4). These metrics provide valuable insights into the accuracy and performance of ML models.

$$\text{RMSE} = \sqrt{\frac{1}{N}\sum_{i=1}^{N}(\alpha_{iso_i}^{\text{Exact}} - \alpha_{iso_i}^{\text{Pred}})^2}. \tag{5.1}$$

$$\text{MAE} = \frac{1}{N}\sum_{i=1}^{N}\left|(\alpha_{iso_i}^{\text{Exact}} - \alpha_{iso_i}^{\text{Pred}})\right|. \tag{5.2}$$

$$\text{MSE} = \frac{1}{N}\sum_{i=1}^{N}(\alpha_{iso_i}^{\text{Exact}} - \alpha_{iso_i}^{\text{Pred}})^2. \tag{5.3}$$

$$\text{MAPE} = \frac{1}{N}\sum_{i=1}^{N}\left|\frac{(\alpha_{iso_i}^{\text{Exact}} - \alpha_{iso_i}^{\text{Pred}})}{\alpha_{iso_i}^{\text{Exact}}}\right|. \tag{5.4}$$

Training dataset: The training dataset comprises α_{iso} and $\Delta\alpha$ calculated using DFT for 1540 diverse configurations of gold nanoclusters with the number of atoms ranging from 17 to 50. The values of α_{iso} and $\Delta\alpha$ in the dataset are scaled to a range from 0 to 1. Figure 5.2 illustrates the distribution of data points in the dataset according to their polarizability values. Any data points above 0.8Å^3 in both α_{iso} and $\Delta\alpha$ are considered

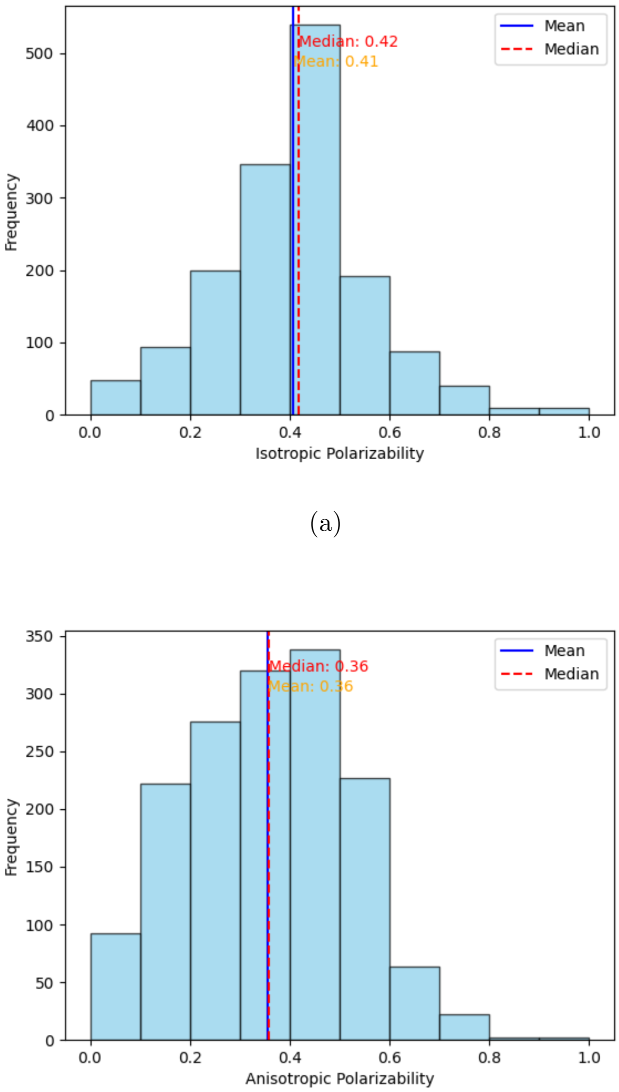

(a)

(b)

Figure 5.2: Distribution of polarizability data from the DFT method: (a) isotropic (α_{iso}) and (b) anisotropy in polarizability ($\Delta\alpha$). The blue line represents the mean, and the red dashed line indicates the median.

outliers and are thus excluded from the datasets.

I evaluated different train/test splits 70:30, 80:20, and 90:10 to determine the best ratio for training and testing. Since ANN models typically require a large amount of training data for optimal performance, I ultimately chose the 90:10 split. The corresponding performances for each split are presented in Table 5.1. The 80:20 split yielded the lowest mean squared error (MSE) of polarizability per atom, with values of 0.7×10^{-5} Å^3/atom for α_{iso} and 2.1×10^{-5} Å^3/atom for $\Delta\alpha$, using the ANN model optimized with GEKF. However, the 90:10 split produced comparable results with only a minimal difference in performance. The 70:30 split resulted in a higher MSE, likely due to the smaller training dataset size.

Table 5.1: MSE per atom for α_{iso} and $\Delta\alpha$ using ANN with GEKF optimizer across different training and testing data splits.

Training: Testing	MSE of polarizability per atom	
	α_{iso} (Å^3/atom)	$\Delta\alpha$ (Å^3/atom)
90 :10	2.10×10^{-5}	3.20×10^{-5}
80 :20	0.70×10^{-5}	2.10×10^{-5}
70 :30	1.11×10^{-4}	1.32×10^{-4}

All DFT calculations are done using the Gaussian 09 [172] package. In this calculation, B3LYP functional [163] is used to treat the exchange and correlation of electrons. The B3LYP functional, a hybrid functional in DFT, combines the Becke three-parameter exchange functional with exact HF exchange and the Lee-Yang-Parr correlation functional. The LANL2DZ basis set [171] is widely used to deal with 19 valence electrons per Au, and the remaining core electron is considered using effective core potential with relativistic correction.

5.3 Results

In this section, I discuss the prediction of polarizabilities, α_{iso} and $\Delta\alpha$, for gold nanoclusters using ANN, GPR, and KRR models. Firstly, using ANN, I estimate the prediction of α_{iso} and $\Delta\alpha$ by considering the bispectrum descriptor as input to ANN. Two different weight optimization methods, ANN-Kalman and ANN-Adam, have been used to train ANN. Four different performance metrics, MAE, MSE, RMSE, and MAPE, are

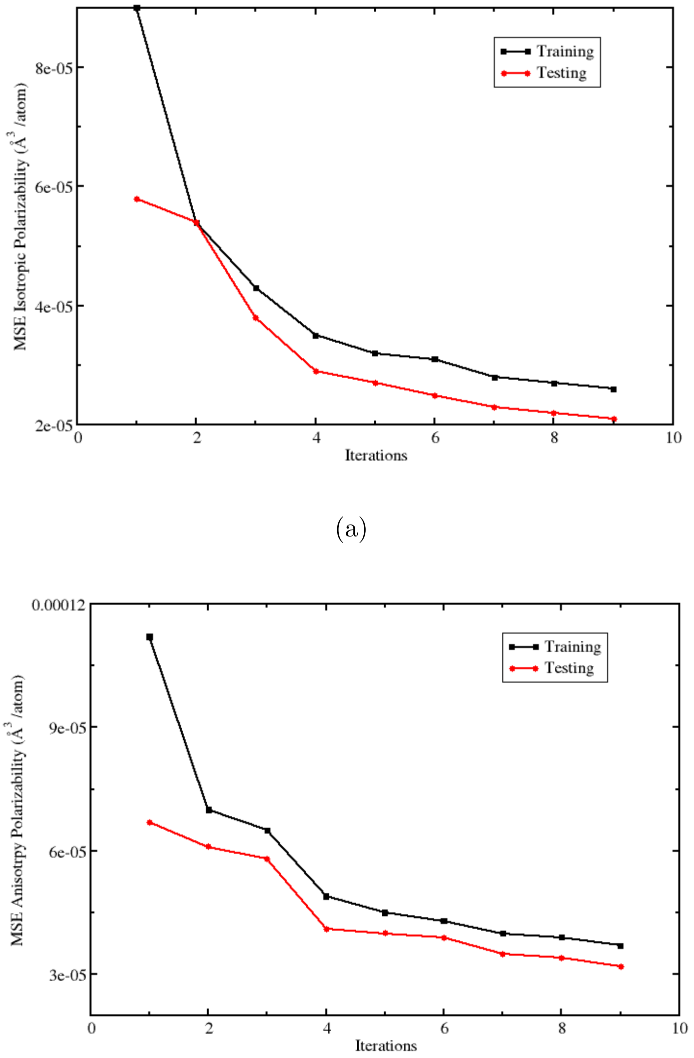

(a)

(b)

Figure 5.3: MSE of polarizability per atom with the number of iterations involved in the training and testing dataset. (a) isotropic (α_{iso}) and (b) anisotropy in polarizability ($\Delta\alpha$).

considered to calculate the error per atom in predicting α_{iso} and $\Delta\alpha$ using ANN.

5.3.1 Prediction of Polarizability using ANN

In the ANN model using bispectrum, the values of performance metrics for ANN-Kalman and ANN-Adam are tabulated in Table 5.2. From Table 5.2, it is clearly evident that ANN-Kalman outperforms the ANN-Adam using all the considered performance metrics. This is because ANN-Kalman, being a second-order method, is generally more accurate than ANN-Adam, which is a first-order method.

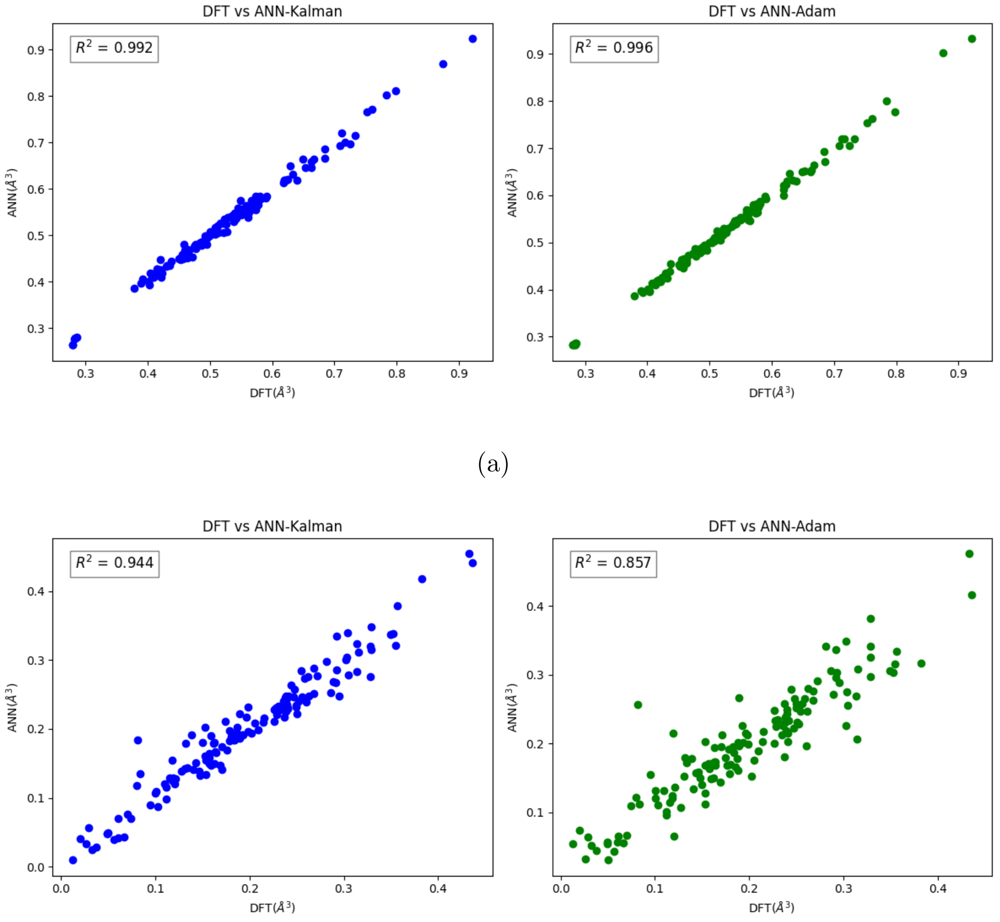

(a)

(b)

Figure 5.4: Comparison of DFT and ANN results using bispectrum descriptors and two different optimization schemes (Kalman and Adam) for the test dataset: (a) isotropic (α_{iso}) and (b) anisotropy in polarizability($\Delta\alpha$).

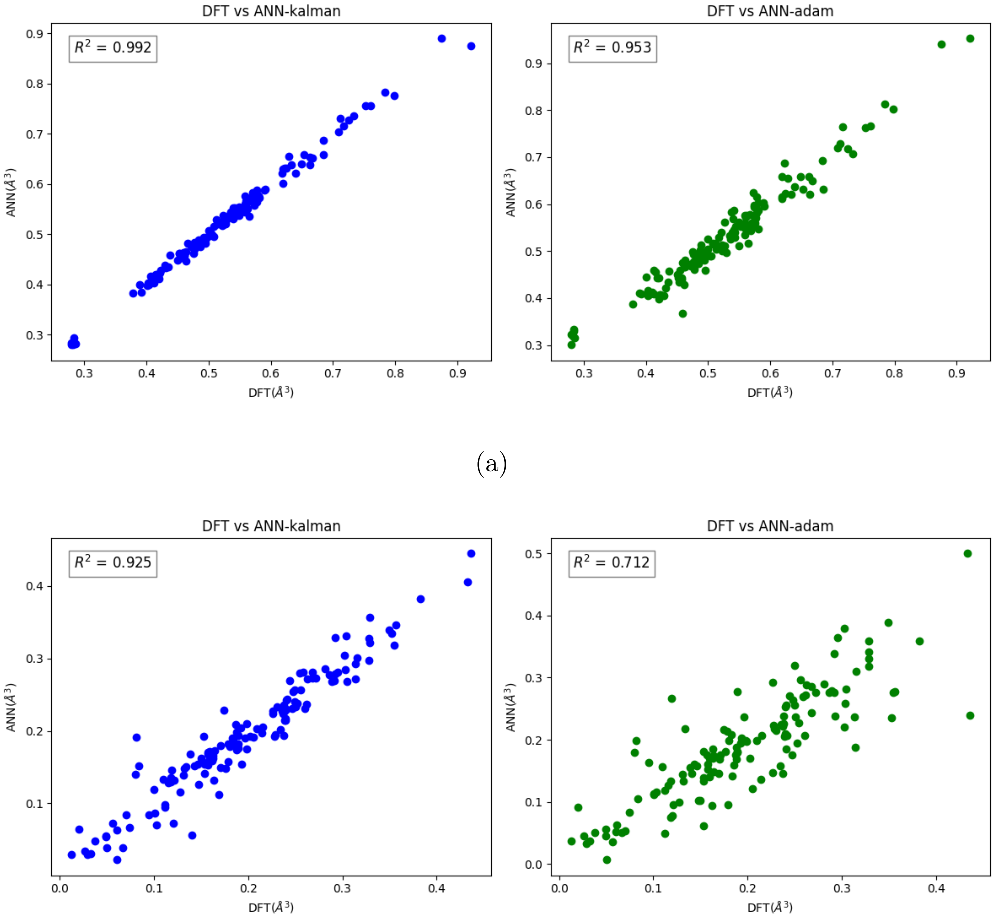

(a)

(b)

Figure 5.5: Comparison of DFT and ANN results using power spectrum descriptors and two different optimization schemes (Kalman and Adam) for the test dataset: (a) isotropic (α_{iso}) and (b) anisotropy in polarizability ($\Delta\alpha$).

Table 5.2: The average errors per atom of different metrics of ANN using bispectrum descriptors in the prediction of polarizabilities (Å^3/atom).

ANN	MAE	MSE	RMSE	MAPE
Kalman	6.7×10^{-4}	2.6×10^{-5}	3.8×10^{-4}	2.1×10^{-3}
Adam	8.0×10^{-3}	3.8×10^{-4}	1.9×10^{-2}	6.5×10^{-2}

In Figure 5.3, I have plotted learning curves to show the MSE per atom for both α_{iso} (Å^3/atom) and $\Delta\alpha$ (Å^3/atom) over the iterations of the ANN-Kalman model. From Table 5.2, it is also evident that MSE shows the lowest error in comparison to other metrics. Hence, I used MSE as a performance metric to calculate the error using different ML models in the present study.

Figure 5.4 presents correlation plots showcasing α_{iso} in 5.4 (a) and $\Delta\alpha$ in 5.4 (b) for gold nanoclusters using the test dataset. These plots indicate that the accuracy of the ANN model using both optimizers is very close to that of the DFT method. From Figure 5.4 (a), the R^2 coefficient values for both ANN-Kalman and ANN-Adam in predicting α_{iso} are 0.99. This indicates a strong correlation between the predicted values and the DFT-based values for α_{iso}. In Figure 5.4 (b), the R^2 coefficient values for ANN-Kalman and ANN-Adam are 0.94 and 0.85, respectively, for $\Delta\alpha$. This indicates a noticeable deviation in the correlation between the ANN model and the DFT. This deviation is more pronounced in the ANN-Adam compared to the ANN-Kalman, indicating that the ANN-Kalman is a better model for predicting α_{iso} and $\Delta\alpha$.

I also employ an ANN-Kalman and ANN-Adam utilizing the power spectrum as input to ANN to predict α_{iso} and $\Delta\alpha$. Upon observation, I note that the average MSE of polarizability per atom of ANN-Kalman is

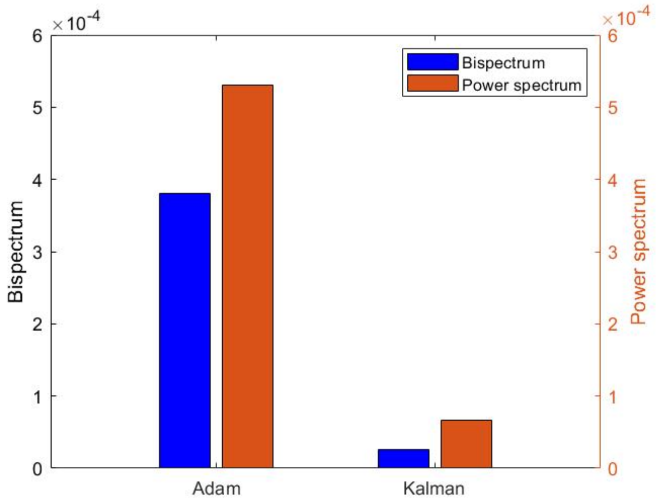

Figure 5.6: Comparison of performance of two ANN models utilizing Kalman and Adam optimizer for bispectrum and power spectrum descriptors.

6.7×10^{-5} (Å^3/atom), significantly lower than that of ANN-Adam, which stands at 4.13×10^{-4} (Å^3/atom). I plot the correlation between DFT and both ANN-Kalman and ANN-Adam for both α_{iso} and $\Delta\alpha$ in Figure 5.5 (a) and (b), respectively. For α_{iso}, the R^2 coefficient values are 0.99 for ANN-Kalman and 0.95 for ANN-Adam. For $\Delta\alpha$, the R^2 coefficient values are 0.92 for ANN-Kalman and 0.71 for ANN-Adam. These results suggest that the performance of ANN-Kalman is superior to ANN-Adam by using a power spectrum descriptor as well. When comparing the performance of the ANN model using bispectrum and power spectrum descriptors, a gain in MSE is evident with the bispectrum descriptors. This suggests that the ANN-Kalman model performs better when incorporating bispectrum descriptors as input in comparison to the power spectrum, as depicted in Figure 5.6.

5.3.2 Prediction of Polarizability using GPR and KRR

The performance of the GPR model is evaluated using bispectrum descriptors as input to assess polarizabilities. The GPR model exhibits a higher MSE of polarizability per atom of 5.6×10^{-4} (Å^3/atom) compared to the ANN-based model. Figure 5.7 (a) and 5.7 (b) depict the correlation between DFT data and predicted data for α_{iso} and $\Delta\alpha$ of the GPR model. The R^2 coefficient value for the GPR model in predicting α_{iso} is found to be 0.99, indicating a strong correlation between the predicted values and DFT. This suggests that the GPR model is highly accurate in estimating α_{iso} values. However, for $\Delta\alpha$, the R^2 coefficient value is slightly lower at 0.86, indicating a slightly weaker correlation with the DFT.

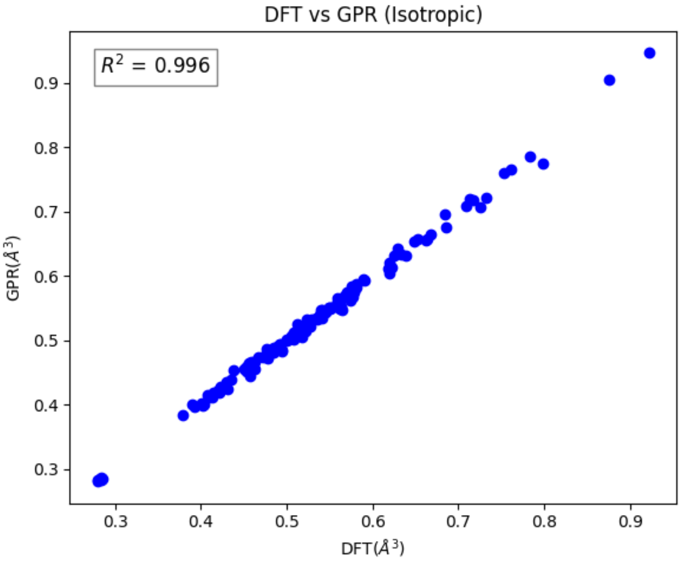

(a)

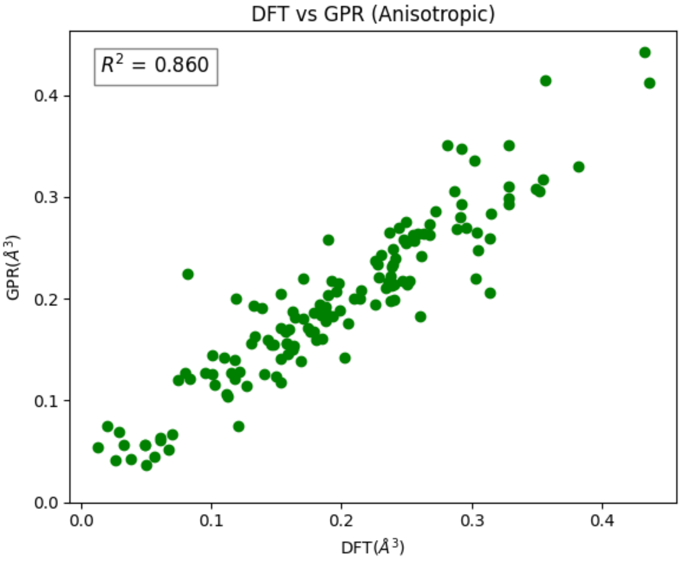

(b)

Figure 5.7: Comparison of DFT and GPR results using bispectrum descriptors for the test dataset: (a) isotropic (α_{iso}) and (b) anisotropy in polarizability ($\Delta\alpha$).

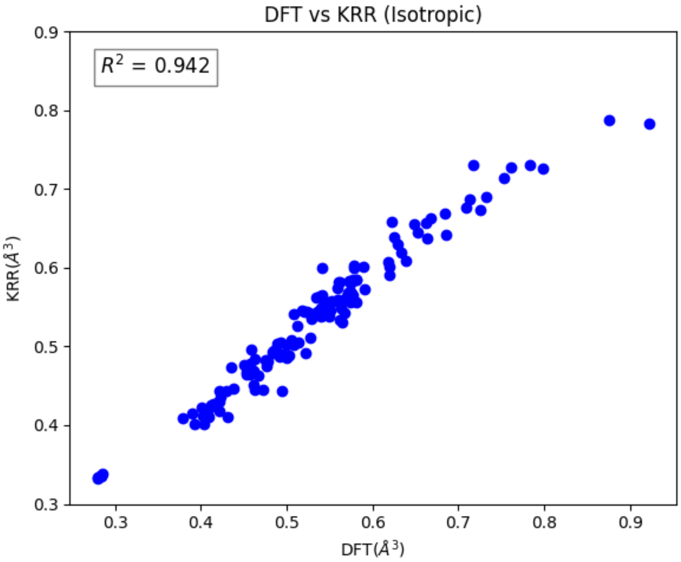

(a)

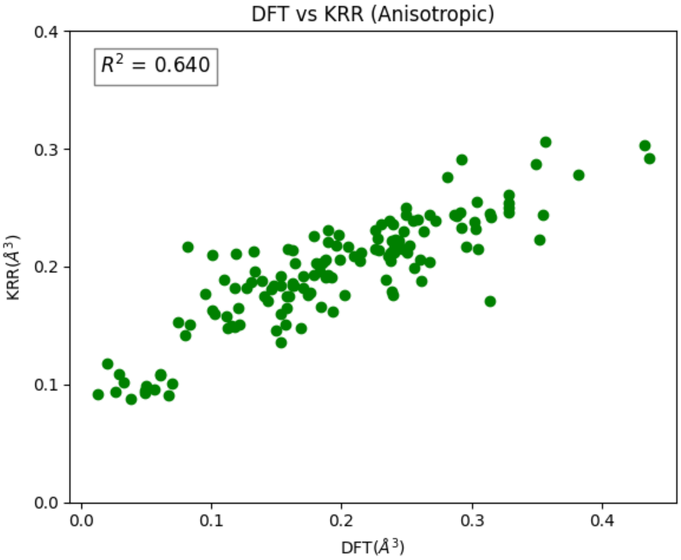

(b)

Figure 5.8: Comparison of DFT and KRR results using bispectrum descriptors for the test dataset: (a) isotropic (α_{iso}) and (b) anisotropy in polarizability ($\Delta\alpha$).

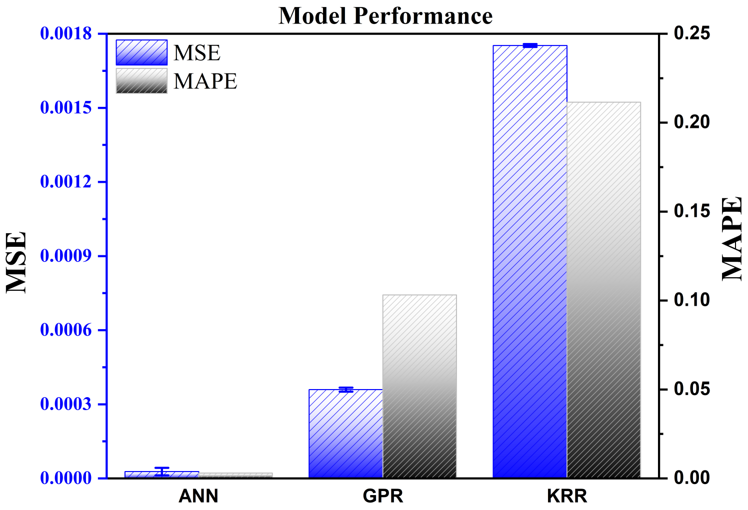

Figure 5.9: Comparison of the MSE and MAPE for all three ML models.

Similar to the GPR and ANN models, I employ the KRR model with bispectrum descriptors as input to assess the polarizabilities. Despite achieving satisfactory training performance based on metrics, its accuracy in predicting polarizabilities is limited, with a relatively high MSE of polarizability per atom of 1.7×10^{-3} (Å^3/atom), especially when compared to ANN and GPR-based models. Figure 5.8 (a) and 5.8 (b) show the correlation between DFT data and the predicted data for α_{iso} and $\Delta\alpha$ of the KRR model, respectively. The R^2 coefficient for the KRR model is 0.94 for α_{iso} and 0.64 for $\Delta\alpha$, indicating a moderate level of correlation between the KRR and DFT-based polarizabilities. This suggests that while the KRR model may exhibit satisfactory training performance, its predictive capabilities for polarizabilities are limited compared to other models, such as ANN and GPR.

I conducted a comparison of MSE and MAPE from Eq. 5.3 and 5.4 for all the considered models. While calculating the MAPE and MSE errors, I considered three consecutive iterations for all the models. The average value of error and its standard derivation have been calculated and shown in Figure 5.9. The standard derivation of all the considered models is within the limit. From Figure 5.9, the ANN model emerged as the best, with minimal error, followed by the GPR and KRR models. Thus, after a thorough comparison, I can conclude that the ANN model excels above the others, solidifying its position as the best-performing model in this analysis.

5.3.3 Validation of ANN-Kalman Model with Different sizes of the Gold Nanoclusters:

5.3.3.1 With Local Minimum Structures :

I used the local minimum structures of gold nanoclusters of Au_{17}, Au_{22}, Au_{23}, Au_{24}, Au_{25}, Au_{26}, Au_{27}, Au_{28} and Au_{34} [23], as shown in Figure 5.10, to test the predictive capability of the ANN-Kalman model. For the given gold nanoclusters, the α_{iso} and $\Delta\alpha$ values obtained using the DFT and ANN with bispectrum descriptors are illustrated in Figure 5.11. From Figure 5.11 (a) and (b), it is evident that there is a strong agreement between the α_{iso} and $\Delta\alpha$ values predicted by the ANN and those obtained through the DFT-based method. This consistency demonstrates the reliability and accuracy of the ANN-Kalman model in replicating DFT results. I also utilize the ANN with the power spectrum descriptors for α_{iso} and $\Delta\alpha$, which are shown in Figure 5.12 (a) and (b), respectively. The results closely resemble the polarizabilities (both α_{iso} and $\Delta\alpha$) for gold nanoclusters obtained through the DFT-based method.

5.3.3.2 With Smaller and Larger Clusters beyond Training Data:

Building on the successful validation with local minimum structures, I further assessed the reliability of the ANN-Kalman model by testing its predictive capability for clusters that are smaller and larger than those not included in the training dataset. Specifically, I focused on small clusters (Au_{10}, Au_{13}, Au_{15}, and Au_{16}) and larger clusters (Au_{38}, Au_{42}, Au_{55}, Au_{58}, Au_{64}, and Au_{70}). The MSE of polarizability per atom for α_{iso} on the testing

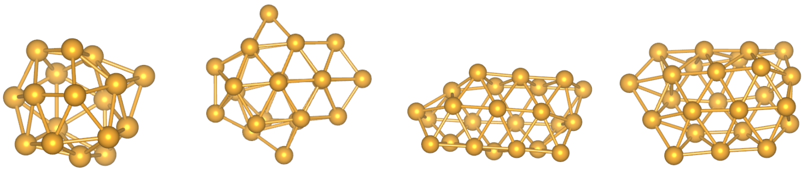

(a) Au_{17} (b) Au_{22} (c) Au_{23} (d) Au_{24}

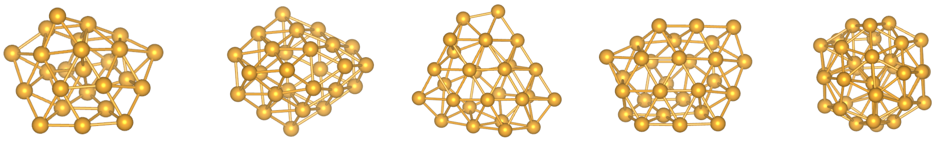

(e) Au_{25} (f) Au_{26} (g) Au_{27} (h) Au_{28} (i) Au_{34}

Figure 5.10: Local minimum structure of different sizes of gold nanoclusters.

data is 2.1×10^{-5} (Å^3/atom), and for $\Delta\alpha$, it is 3.3 $\times10^{-5}$ (Å^3/atom). The squared error of polarizability per atom for the given clusters, for both α_{iso} and $\Delta\alpha$, is given in Table 5.3. From this table, it is evident that the squared errors (SE) for clusters ranging from Au_{10} to Au_{16} and large clusters from Au_{38}-Au_{58} are relatively close to or slightly higher than the testing MSE values indicating the consistent performance of the ANN-Kalman model. However, for clusters such as Au_{64} and Au_{70}, the squared errors exceed the testing MSE. The increase in error for these clusters is due to the lack of atomic environment representation in the training data.

So, it can be concluded that the ANN model is an efficient and accurate alternative to DFT that provides significant computational advantages without compromising precision.

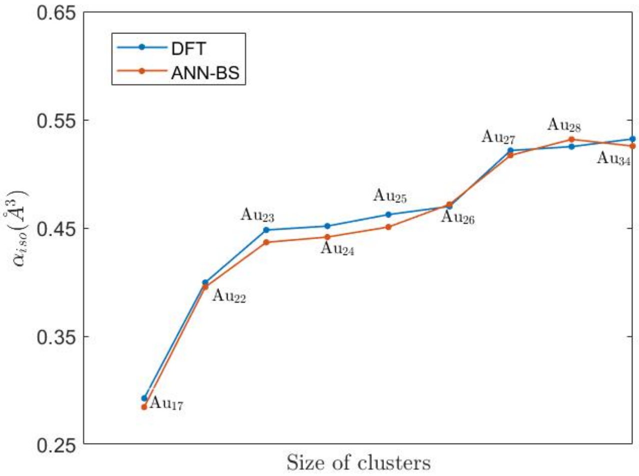

(a)

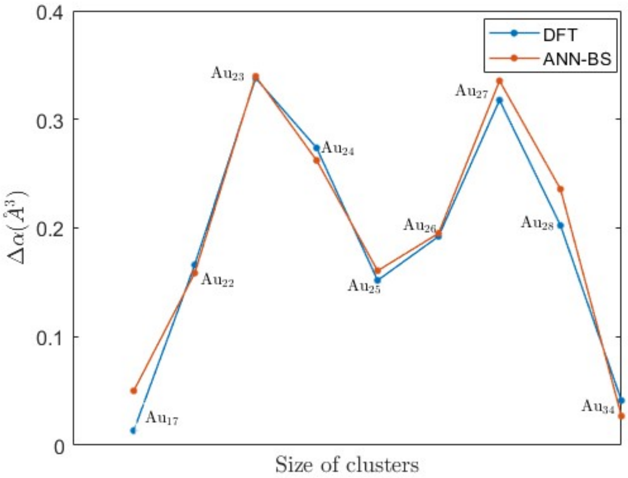

(b)

Figure 5.11: Comparison of DFT and ANN predicted polarizabilities of different sizes of gold nanoclusters using bispectrum: (a) isotropic (α_{iso}) and (b) anisotropy in polarizability ($\Delta\alpha$).

5.4 Summary

In the summary of this work, our study has demonstrated the efficiency and accuracy of ML models, specifically ANN, GPR and KRR, in predicting both isotropic polarizability and anisotropy in polarizability of gold nanoclusters. The ANN models, incorporating bispectrum and power spectrum descriptors, demonstrated superior performance, with the GEKF

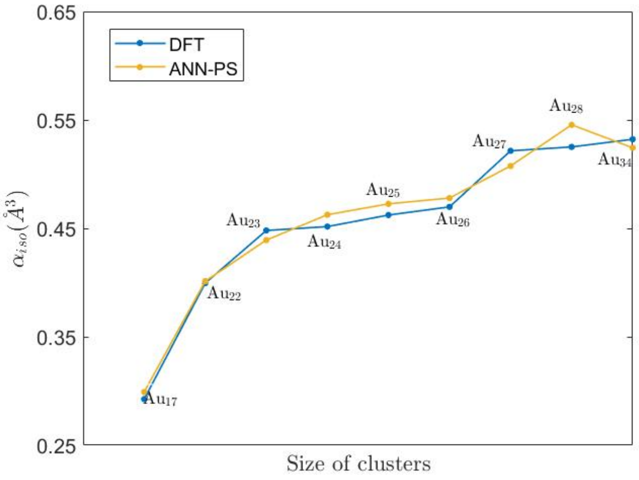

(a)

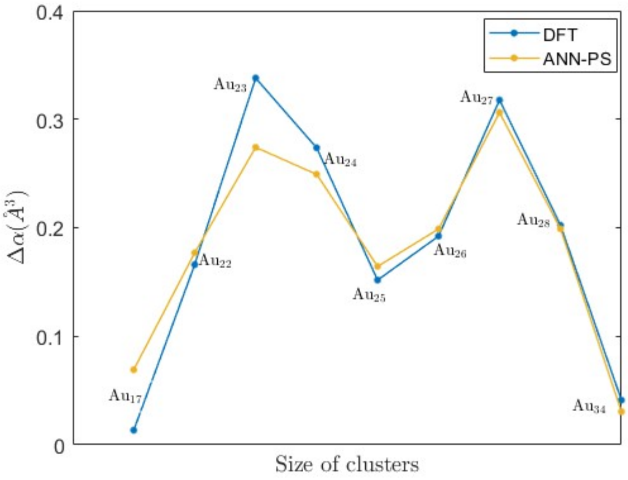

(b)

Figure 5.12: Comparison of DFT and ANN predicted polarizabilities of different sizes of the gold nanoclusters using power spectrum descriptor: (a) isotropic (α_{iso}) and (b) anisotropy in polarizability ($\Delta\alpha$).

outperforming the Adam optimizer across various performance metrics. Furthermore, when compared to DFT data, the ANN models showed a strong agreement, especially concerning isotropic polarizabilities, indicating their high accuracy. Similarly, GPR models showcased commendable performance in predicting isotropic polarizabilities, albeit with noticeable discrepancies in anisotropic predictions compared to DFT-based methods. Conversely, KRR models exhibited limited accuracy, particularly in the pre-

Table 5.3: MSE of testing data and SE per atom of α_{iso} and $\Delta\alpha$ for various clusters using the ANN-Kalman model.

Cluster	SE of α_{iso} (Å^3/atom)	SE of$\Delta\alpha$ (Å^3/atom)
Testing MSE	2.1×10^{-5}	3.2×10^{-5}
Au_{10}	8.8×10^{-5}	9.9×10^{-6}
Au_{13}	2.4×10^{-4}	1.5×10^{-3}
Au_{15}	1.0×10^{-6}	1.3×10^{-4}
Au_{16}	8.4×10^{-5}	1.0×10^{-4}
Au_{38}	3.6×10^{-5}	1.0×10^{-6}
Au_{42}	3.2×10^{-5}	2.0×10^{-6}
Au_{55}	2.5×10^{-5}	1.6×10^{-5}
Au_{58}	2.3×10^{-5}	4.4×10^{-5}
Au_{64}	2.2×10^{-3}	7.7×10^{-3}
Au_{70}	4.4×10^{-3}	9.9×10^{-3}

diction of anisotropy in polarizability, reinforcing the superiority of ANN and GPR models. The validation of ANN weights against a local minimum structure of gold nanoclusters confirmed the model's accuracy in predicting polarizabilities, with outcomes closely resembling those obtained from DFT.

Chapter 6

Conclusion and Future Perspective

6.1 Conclusion

This chapter presents a concise overview of the thesis to develop a robust and efficient ML framework for modeling the energy and its derivatives for metal nanoclusters. Specifically, the research focuses on leveraging ANN to accurately capture the intricate interactions between atomic configurations, enabling the precise prediction of energy, forces, and response properties. This work aims to address the computational challenges associated with traditional DFT methods, which become increasingly impractical for studying larger metallic nanoclusters due to their high resource demands and complexity, particularly when calculating first- and second-order derivatives. By employing a data-driven approach that integrates high-quality DFT data with ANN modeling, the thesis seeks to enhance the understanding of the structural, dynamic, and electronic properties of metal nanoclusters.

The major findings are summarized as follows:

1. The ANN potentials developed in this study have shown a remarkable ability to accurately predict energy and its derivatives. By effec-

tively capturing the complex interactions between atoms, these potentials operate with high precision while significantly reducing computational costs. The time required for accurate energy and force calculations using ANN is much faster than DFT, which typically takes hours. This efficiency not only accelerates simulations but also opens avenues for exploring larger systems and longer timescales in MD simulations.

2. The proposed approach for metal nanoalloys is 'transferable' because its parameters are based on interatomic distances, effective nuclear charges, and the reduced mass of the bonds within the system. This flexibility allows it to be applied to various chemical systems.
3. Our geometric analysis shows that the most stable isomers of Ag-Pt nanoalloys have a core-shell structure. In these structures, platinum atoms prefer to stay in the core, while silver atoms are on the surface. This study helps to understand the arrangement of atoms in these nanoalloys and how it affects their catalytic efficiency. By optimizing this structure, I can potentially develop more effective catalysts for industrial use.
4. By studying how Ag-Pt nanoalloys interact with small gas molecules like O_2 and CO, I gained insights into how these molecules are adsorbed. Our results show that the Pt atoms in the core have a limited effect on the adsorption of these gases, while Pt atoms located on the surface have a much greater influence. This emphasizes the importance of the surface composition and structure in determining catalytic activity, indicating potential ways to improve catalyst designs.
5. By incorporating bispectrum coefficients as inputs to the ANN, I successfully fitted the second-order derivatives with respect to the electric field, enabling the calculation of polarizability for gold nanoclusters. This demonstrates the ANN's capacity to predict higher-order derivatives based on local atomic environments, further establishing its versatility in capturing complex material properties. This capa-

bility is essential for understanding the responses of materials under varying external fields.

6. In our study of different ML models for predicting isotropic and anisotropic polarizability, the ANN performed better than the other models, showing strong reliability and accuracy in its predictions. This success highlights how effective ANNs can be in modeling complex material properties and their potential use in energy-related applications.

6.2 Future Aspects of this Work

The work that can be taken forward from this thesis can be summarized as:

1. It's important to explore ways to build accurate ANN potentials that rely on fewer data points. Since ANN potentials depend heavily on the amount of data used to train them, reducing data requirements without losing accuracy could make them more practical and efficient to use.
2. The method for creating the training dataset can be modified by utilizing DFT data obtained from different functionals. This adjustment can enhance the accuracy of the fitted energy, thereby improving the PES.
3. The ANN-based method developed here for Ag-Pt nanoalloys can be applied to other bimetallic or multi-metallic systems, such as Au-Pt or Pd-Pt, enabling broader exploration of nanoalloys with tunable catalytic properties.
4. The present study focuses on the adsorption of CO and O_2 on Ag-Pt nanoalloys and will now extend to the complete CO oxidation reaction to further investigate the catalytic mechanisms and optimize the performance of Ag-Pt nanoalloys.
5. ML methods can be employed to study catalysis by analyzing reactions such as the reduction of carbon dioxide using Ag-Pt nanoalloys,

leading to improved catalyst design and performance.

6. Expanding the model to include third and higher-order derivatives with respect to external fields could yield insights into complex response properties, such as hyperpolarizability, enhancing the understanding of materials behaviour under diverse external conditions.
7. The ANN method could be advanced by creating more sophisticated approaches that adjust the number of hidden layers and neurons based on real-time analysis. This would help the networks better adapt to complex problems and reduce the chances of overfitting and underfitting.

Bibliography

[1] Paul Mulvaney. Nanoscale materials (eds l. liz-marzán and pv kamat), 2003.

[2] A Paul Alivisatos. Semiconductor clusters, nanocrystals, and quantum dots. *science*, 271(5251):933–937, 1996.

[3] Riccardo Ferrando, Julius Jellinek, and Roy L Johnston. Nanoalloys: from theory to applications of alloy clusters and nanoparticles. *Chemical reviews*, 108(3):845–910, 2008.

[4] Rongchao Jin. Atomically precise metal nanoclusters: stable sizes and optical properties. *Nanoscale*, 7(5):1549–1565, 2015.

[5] Zhen Hua Li and Donald G Truhlar. Nanothermodynamics of metal nanoparticles. *Chemical Science*, 5(7):2605–2624, 2014.

[6] Sujit Kumar Ghosh and Tarasankar Pal. Interparticle coupling effect on the surface plasmon resonance of gold nanoparticles: from theory to applications. *Chemical reviews*, 107(11):4797–4862, 2007.

[7] Rajib Ghosh Chaudhuri and Santanu Paria. Core/shell nanoparticles: classes, properties, synthesis mechanisms, characterization, and applications. *Chemical reviews*, 112(4):2373–2433, 2012.

[8] Ashish Kumar Singh and Qiang Xu. Synergistic catalysis over bimetallic alloy nanoparticles. *ChemCatChem*, 5(3):652–676, 2013.

[9] Jinlong Gong. Structure and surface chemistry of gold-based model catalysts. *Chemical reviews*, 112(5):2987–3054, 2012.

[10] A Stephen K Hashmi and Graham J Hutchings. Gold catalysis. *Angewandte Chemie International Edition*, 45(47):7896–7936, 2006.

[11] Manolis Stratakis and Hermenegildo Garcia. Catalysis by supported gold nanoparticles: beyond aerobic oxidative processes. *Chemical Reviews*, 112(8):4469–4506, 2012.

[12] Marie-Christine Daniel and Didier Astruc. Gold nanoparticles: assembly, supramolecular chemistry, quantum-size-related properties, and applications toward biology, catalysis, and nanotechnology. *Chemical reviews*, 104(1):293–346, 2004.

[13] Claire M Cobley, Jingyi Chen, Eun Chul Cho, Lihong V Wang, and Younan Xia. Gold nanostructures: a class of multifunctional materials for biomedical applications. *Chemical Society Reviews*, 40(1):44–56, 2011.

[14] WD Knight, Keith Clemenger, Walt A De Heer, Winston A Saunders, MY Chou, and Marvin L Cohen. Electronic shell structure and abundances of sodium clusters. *Physical review letters*, 52(24):2141, 1984.

[15] René Fournier and Satya Bulusu. Closed-shell metal clusters. *Metal Clusters and Nanoalloys*, pages 81–103, 2013.

[16] Thomas Patrick Martin. Shells of atoms. *Physics Reports*, 273(4):199–241, 1996.

[17] Taizo Mori and Torsten Hegmann. Determining the composition of gold nanoparticles: a compilation of shapes, sizes, and calculations using geometric considerations. *Journal of Nanoparticle Research*, 18:1–36, 2016.

[18] Matthias Brack. The physics of simple metal clusters: self-consistent jellium model and semiclassical approaches. *Reviews of modern physics*, 65(3):677, 1993.

[19] Walt A De Heer. The physics of simple metal clusters: experimental aspects and simple models. *Reviews of Modern Physics*, 65(3):611, 1993.

[20] Keith Clemenger. Ellipsoidal shell structure in free-electron metal clusters. *Physical Review B*, 32(2):1359, 1985.

[21] Michael I Baskes. Modified embedded-atom potentials for cubic materials and impurities. *Physical review B*, 46(5):2727, 1992.

[22] Masatake Haruta, Tetsuhiko Kobayashi, Hiroshi Sano, and Nobumasa Yamada. Novel gold catalysts for the oxidation of carbon monoxide at a temperature far below 0 c. *Chemistry Letters*, 16(2):405–408, 1987.

[23] Siva Chiriki, Shweta Jindal, and Satya S Bulusu. Neural network potentials for dynamics and thermodynamics of gold nanoparticles. *The Journal of chemical physics*, 146(8), 2017.

[24] Edoardo Aprà, Riccardo Ferrando, and Alessandro Fortunelli. Density-functional global optimization of gold nanoclusters. *Physical Review B—Condensed Matter and Materials Physics*, 73(20):205414, 2006.

[25] IL Garzón, K Michaelian, MR Beltrán, A Posada-Amarillas, P Ordejón, E Artacho, D Sánchez-Portal, and JM Soler. Lowest energy structures of gold nanoclusters. *Physical review letters*, 81(8):1600, 1998.

[26] Faye Pittaway, Lauro Oliver Paz-Borbón, Roy L Johnston, Haydar Arslan, Riccardo Ferrando, Christine Mottet, Giovanni Barcaro, and Alessandro Fortunelli. Theoretical studies of palladium- gold nanoclusters: Pd- au clusters with up to 50 atoms. *The Journal of Physical Chemistry C*, 113(21):9141–9152, 2009.

[27] Wei Huang, Satya Bulusu, Rhitankar Pal, Xiao Cheng Zeng, and Lai-Sheng Wang. Structural transition of gold nanoclusters: from

the golden cage to the golden pyramid. *ACS nano*, 3(5):1225–1230, 2009.

[28] Hannu Häkkinen, Bokwon Yoon, Uzi Landman, Xi Li, Hua-Jin Zhai, and Lai-Sheng Wang. On the electronic and atomic structures of small au n-(n= 4- 14) clusters: a photoelectron spectroscopy and density-functional study. *The Journal of Physical Chemistry A*, 107(32):6168–6175, 2003.

[29] Satya Bulusu, Xi Li, Lai-Sheng Wang, and Xiao Cheng Zeng. Evidence of hollow golden cages. *Proceedings of the National Academy of Sciences*, 103(22):8326–8330, 2006.

[30] Jun Li, Xi Li, Hua-Jin Zhai, and Lai-Sheng Wang. Au20: a tetrahedral cluster. *Science*, 299(5608):864–867, 2003.

[31] CD Dong and XG Gong. Gold cluster beyond hollow cage: A double shell structure of au58. *The Journal of chemical physics*, 132(10), 2010.

[32] B Palpant, B Prével, J Lermé, E Cottancin, M Pellarin, M Treilleux, A Perez, JL Vialle, and M Broyer. Optical properties of gold clusters in the size range 2–4 nm. *Physical Review B*, 57(3):1963, 1998.

[33] Gregory A Bishea and Michael D Morse. Spectroscopic studies of jet-cooled agau and au.

[34] Haiko Handschuh, Gerd Ganteför, Paul Siegfried Bechthold, and Wolfgang Eberhardt. A comparison of photoelectron spectroscopy and two-photon ionization spectroscopy: Excited states of au2, au3, and au4. *The Journal of chemical physics*, 100(10):7093–7100, 1994.

[35] Jie Zheng, Philip R Nicovich, and Robert M Dickson. Highly fluorescent noble-metal quantum dots. *Annu. Rev. Phys. Chem.*, 58(1):409–431, 2007.

[36] Michael Faraday. X. the bakerian lecture.—experimental relations of gold (and other metals) to light. *Philosophical transactions of the Royal Society of London*, (147):145–181, 1857.

[37] Damien Alloyeau, Christine Mottet, and Christian Ricolleau. *Nanoalloys: Synthesis, structure and properties*. Springer Science & Business Media, 2012.

[38] Xin Lian, Wenlong Guo, Feila Liu, Yang Yang, Peng Xiao, Yunhuai Zhang, and WeiQuan Tian. Dft studies on pt3m (m= pt, ni, mo, ru, pd, rh) clusters for co oxidation. *Computational Materials Science*, 96:237–245, 2015.

[39] Song-Lin Peng, Li-Yong Gan, Ren-Yu Tian, and Yu-Jun Zhao. Theoretical study of co adsorption and oxidation on the gold–palladium bimetal clusters. *Computational and Theoretical Chemistry*, 977(1-3):62–68, 2011.

[40] Weiting Yu, Marc D Porosoff, and Jingguang G Chen. Review of pt-based bimetallic catalysis: from model surfaces to supported catalysts. *Chemical reviews*, 112(11):5780–5817, 2012.

[41] Krishnakanta Mondal, Arup Banerjee, and Tapan K Ghanty. Structural and chemical properties of subnanometer-sized bimetallic au19pt cluster. *The Journal of Physical Chemistry C*, 118(22):11935–11945, 2014.

[42] Mauricio J Piotrowski, Paulo Piquini, and Juarez LF Da Silva. Platinum-based nanoalloys pt n tm55–n (tm= co, rh, au): a density functional theory investigation. *The Journal of Physical Chemistry C*, 116(34):18432–18439, 2012.

[43] Chunrong Song, Qingfeng Ge, and Lichang Wang. Dft studies of pt/au bimetallic clusters and their interactions with the co molecule. *The Journal of Physical Chemistry B*, 109(47):22341–22350, 2005.

[44] Diego Guedes-Sobrinho, Ricardo K Nomiyama, Anderson S Chaves, Maurício J Piotrowski, and Juarez LF Da Silva. Structure, electronic, and magnetic properties of binary pt n tm55–n (tm= fe, co, ni, cu, zn) nanoclusters: A density functional theory investigation. *The Journal of Physical Chemistry C*, 119(27):15669–15679, 2015.

[45] PL Rodríguez-Kessler, A Muñoz-Castro, PA Alonso-Dávila, F Aguilera-Granja, and AR Rodríguez-Domínguez. Structural, electronic and catalytic properties of bimetallic ptnagn (n= 1–7) clusters. *Journal of Alloys and Compounds*, 845:155897, 2020.

[46] Joanna Wisniewska, Hazar Guesmi, Maria Ziolek, and Frederik Tielens. Stability of nanostructured silver-platinum alloys. *Journal of Alloys and Compounds*, 770:934–941, 2019.

[47] Paulo CD Mendes, Stella G Justo, Johnatan Mucelini, Marinalva D Soares, Krys EA Batista, Marcos G Quiles, Mauricio J Piotrowski, and Juarez LF Da Silva. Ab initio insights into the formation mechanisms of 55-atom pt-based core–shell nanoalloys. *The Journal of Physical Chemistry C*, 124(1):1158–1164, 2019.

[48] Dora J Borbón-González, Alessandro Fortunelli, Giovanni Barcaro, Luca Sementa, Roy L Johnston, and Alvaro Posada-Amarillas. Global minimum pt13m20 (m= ag, au, cu, pd) dodecahedral core–shell clusters. *The Journal of Physical Chemistry A*, 117(51):14261–14266, 2013.

[49] Giovanni Barcaro, Luca Sementa, Alessandro Fortunelli, and Mauro Stener. Optical properties of pt and ag–pt nanoclusters from tddft calculations: Plasmon suppression by pt poisoning. *The Journal of Physical Chemistry C*, 118(48):28101–28108, 2014.

[50] Lei Deng, Huiqiu Deng, Shifang Xiao, Jianfeng Tang, and Wangyu Hu. Morphology, dimension, and composition dependence of thermodynamically preferred atomic arrangements in ag–pt nanoalloys. *Faraday Discussions*, 162:293–306, 2013.

[51] Kayoung Yun, Yong-Hun Cho, Pil-Ryung Cha, Jaegab Lee, Ho-Seok Nam, Jung Soo Oh, Jung-Hae Choi, and Seung-Cheol Lee. Monte carlo simulations of the structure of pt-based bimetallic nanoparticles. *Acta Materialia*, 60(12):4908–4916, 2012.

[52] Fabio R Negreiros, Avik Halder, Chunrong Yin, Akansha Singh, Giovanni Barcaro, Luca Sementa, Eric C Tyo, Michael J Pellin, Stephan Bartling, Karl-Heinz Meiwes-Broer, et al. Bimetallic ag-pt subnanometer supported clusters as highly efficient and robust oxidation catalysts. *Angewandte Chemie International Edition*, 57(5):1209–1213, 2018.

[53] Fabian Mares-Briones, América Higareda, Jose Luis Lopez-Miranda, Rubén Mendoza-Cruz, and Rodrigo Esparza. Bimetallic agpt nanoalloys as an electrocatalyst for ethanol oxidation reaction: synthesis, structural analysis, and electro-catalytic activity. *Nanomaterials*, 13(8):1396, 2023.

[54] I Karakaya and WT Thompson. The ag-pt (silver-platinum) system. *Bulletin of alloy phase diagrams*, 8(4):334–340, 1987.

[55] Ph Durussel and P Feschotte. A revision of the binary system ag pt. *Journal of alloys and compounds*, 239(2):226–230, 1996.

[56] FR Negreiros, F Taherkhani, G Parsafar, A Caro, and A Fortunelli. Kinetics of chemical ordering in a ag-pt nanoalloy particle via first-principles simulations. *The Journal of chemical physics*, 137(19), 2012.

[57] Gustavo E Ramírez-Caballero, Yuguang Ma, Rafael Callejas-Tovar, and Perla B Balbuena. Surface segregation and stability of core–shell alloy catalysts for oxygen reduction in acid medium. *Physical Chemistry Chemical Physics*, 12(9):2209–2218, 2010.

[58] C Becker and CR Henry. Cluster size dependent kinetics for the oxidation of co on a pdmgo (100) model catalyst. *Surface science*, 352:457–462, 1996.

[59] Yizhong Lu and Wei Chen. Sub-nanometre sized metal clusters: from synthetic challenges to the unique property discoveries. *Chemical Society Reviews*, 41(9):3594–3623, 2012.

[60] Chuanyi Jia, Xijun Wang, Wenhui Zhong, Zhunzhun Wang, Oleg V Prezhdo, Yi Luo, and Jun Jiang. Catalytic chemistry predicted by a charge polarization descriptor: synergistic o2 activation and co oxidation by au–cu bimetallic clusters on tio2 (101). *ACS applied materials & interfaces*, 11(9):9629–9640, 2019.

[61] Daojian Cheng, Haoxiang Xu, and Alessandro Fortunelli. Tuning the catalytic activity of au–pd nanoalloys in co oxidation via composition. *Journal of catalysis*, 314:47–55, 2014.

[62] Hüseyin Yıldırım and Haydar Arslan. Oxygen adsorption in ag (m)@ x (n)(x= pd, pt) core-shell nanoalloys (m+ n= 55), structural and energetic properties: A dft study. *Physica B: Condensed Matter*, 673:415494, 2024.

[63] Ali Kemal Garip, Haydar Arslan, Daniele Rapetti, and Riccardo Ferrando. A dft study of chemical ordering and oxygen adsorption in auptpd ternary nanoalloys. *Materials Today Communications*, 25:101545, 2020.

[64] Daojian Cheng and Wenchuan Wang. Tailoring of pd–pt bimetallic clusters with high stability for oxygen reduction reaction. *Nanoscale*, 4(7):2408–2415, 2012.

[65] Weiwei He, Xiaochun Wu, Jianbo Liu, Ke Zhang, Weiguo Chu, Lili Feng, Xiaona Hu, Weiya Zhou, and Sishen Xie. Formation of agpt alloy nanoislands via chemical etching with tunable optical and catalytic properties. *Langmuir*, 26(6):4443–4448, 2010.

[66] Weiwei He, Xiaochun Wu, Jianbo Liu, Ke Zhang, Weiguo Chu, Lili Feng, Xiaona Hu, Weiya Zhou, and Sishen Xie. Pt-guided formation of pt- ag alloy nanoislands on au nanorods and improved

methanol electro-oxidation. *The Journal of Physical Chemistry C*, 113(24):10505–10510, 2009.

[67] Chien-Liang Lee and Chun-Ming Tseng. Ag- pt nanoplates: Galvanic displacement preparation and their applications as electrocatalysts. *The Journal of Physical Chemistry C*, 112(35):13342–13345, 2008.

[68] Jian Gao, Xichun Luo, Fengzhou Fang, and Jining Sun. Fundamentals of atomic and close-to-atomic scale manufacturing: a review. *International Journal of Extreme Manufacturing*, 4(1):012001, 2021.

[69] John C Slater. A simplification of the hartree-fock method. *Physical review*, 81(3):385, 1951.

[70] Pierre Hohenberg and Walter Kohn. Inhomogeneous electron gas. *Physical review*, 136(3B):B864, 1964.

[71] John Edward Lennard-Jones. On the determination of molecular fields.—ii. from the equation of state of a gas. *Proceedings of the Royal Society of London. Series A, Containing Papers of a Mathematical and Physical Character*, 106(738):463–477, 1924.

[72] Louis A Girifalco and Victor G Weizer. Application of the morse potential function to cubic metals. *Physical Review*, 114(3):687, 1959.

[73] Raju P Gupta. Lattice relaxation at a metal surface. *Physical Review B*, 23(12):6265, 1981.

[74] John N Murrell and Rachel E Mottram. Potential energy functions for atomic solids. *Molecular physics*, 69(3):571–585, 1990.

[75] Murray S Daw and Michael I Baskes. Embedded-atom method: Derivation and application to impurities, surfaces, and other defects in metals. *Physical Review B*, 29(12):6443, 1984.

[76] SM Foiles, MI Baskes, and Murray S Daw. Embedded-atom-method functions for the fcc metals cu, ag, au, ni, pd, pt, and their alloys. *Physical review B*, 33(12):7983, 1986.

[77] MW Finnis and JE Sinclair. A simple empirical n-body potential for transition metals. *Philosophical Magazine A*, 50(1):45–55, 1984.

[78] Kimberly Chenoweth, Adri CT Van Duin, and William A Goddard. Reaxff reactive force field for molecular dynamics simulations of hydrocarbon oxidation. *The Journal of Physical Chemistry A*, 112(5):1040–1053, 2008.

[79] Thomas P Senftle, Sungwook Hong, Md Mahbubul Islam, Sudhir B Kylasa, Yuanxia Zheng, Yun Kyung Shin, Chad Junkermeier, Roman Engel-Herbert, Michael J Janik, Hasan Metin Aktulga, et al. The reaxff reactive force-field: development, applications and future directions. *npj Computational Materials*, 2(1):1–14, 2016.

[80] BWH Van Beest, Gert Jan Kramer, and RA Van Santen. Force fields for silicas and aluminophosphates based on ab initio calculations. *Physical review letters*, 64(16):1955, 1990.

[81] Kenno Vanommeslaeghe, Elizabeth Hatcher, Chayan Acharya, Sibsankar Kundu, Shijun Zhong, Jihyun Shim, Eva Darian, Olgun Guvench, P Lopes, Igor Vorobyov, et al. Charmm general force field: A force field for drug-like molecules compatible with the charmm all-atom additive biological force fields. *Journal of computational chemistry*, 31(4):671–690, 2010.

[82] Géza Fogarasi and Péter Pulay. Ab initio vibrational force fields. *Annual Review of Physical Chemistry*, 35(1):191–213, 1984.

[83] NF Lane. The theory of electron-molecule collisions. *Reviews of Modern Physics*, 52(1):29, 1980.

[84] Alberto Vela and Jose L Gazquez. A relationship between the static dipole polarizability, the global softness, and the fukui function. *Journal of the American Chemical Society*, 112(4):1490–1492, 1990.

[85] Sanchita Hati and Dipankar Datta. Hardness and electric dipole polarizability. atoms and clusters. *The Journal of Physical Chemistry*, 98(41):10451–10454, 1994.

[86] Fivos Perakis, Luigi De Marco, Andrey Shalit, Fujie Tang, Zachary R Kann, Thomas D Kuhne, Renato Torre, Mischa Bonn, and Yuki Nagata. Vibrational spectroscopy and dynamics of water. *Chemical reviews*, 116(13):7590–7607, 2016.

[87] Xin Zhang, Qing-Hai Tan, Jiang-Bin Wu, Wei Shi, and Ping-Heng Tan. Review on the raman spectroscopy of different types of layered materials. *Nanoscale*, 8(12):6435–6450, 2016.

[88] Norman Colthup. *Introduction to infrared and Raman spectroscopy.* Elsevier, 2012.

[89] Robert W Boyd, Alexander L Gaeta, and Enno Giese. Nonlinear optics. In *Springer Handbook of Atomic, Molecular, and Optical Physics*, pages 1097–1110. Springer, 2008.

[90] Georges Henry Wagnière. *Linear and nonlinear optical properties of molecules.* 1993.

[91] Julius Jellinek. *Theory of atomic and molecular clusters: with a glimpse at experiments.* Springer Science & Business Media, 1999.

[92] Lien Ai Nguyen, Hua He, and Chuong Pham-Huy. Chiral drugs: an overview. *International journal of biomedical science: IJBS*, 2(2):85, 2006.

[93] Michael JS Dewar, Eve G Zoebisch, Eamonn F Healy, and James JP Stewart. Development and use of quantum mechanical molecular models. 76. am1: a new general purpose quantum mechanical molecular model. *Journal of the American Chemical Society*, 107(13):3902–3909, 1985.

[94] James JP Stewart. Optimization of parameters for semiempirical methods ii. applications. *Journal of computational chemistry*, 10(2):221–264, 1989.

[95] Jörg Behler and Michele Parrinello. Generalized neural-network representation of high-dimensional potential-energy surfaces. *Physical review letters*, 98(14):146401, 2007.

[96] Warren S McCulloch and Walter Pitts. A logical calculus of the ideas immanent in nervous activity. *The bulletin of mathematical biophysics*, 5:115–133, 1943.

[97] Frank Rosenblatt. The perceptron: a probabilistic model for information storage and organization in the brain. *Psychological review*, 65(6):386, 1958.

[98] Paul John Werbos. *The roots of backpropagation: from ordered derivatives to neural networks and political forecasting*, volume 1. John Wiley & Sons, 1994.

[99] John J Hopfield. Neural networks and physical systems with emergent collective computational abilities. *Proceedings of the national academy of sciences*, 79(8):2554–2558, 1982.

[100] J. Ross Quinlan. Induction of decision trees. *Machine learning*, 1:81–106, 1986.

[101] Corinna Cortes. Support-vector networks. *Machine Learning*, 1995.

[102] Yoav Freund and Robert E Schapire. A desicion-theoretic generalization of on-line learning and an application to boosting. In *European conference on computational learning theory*, pages 23–37. Springer, 1995.

[103] Leo Breiman. Random forests. *Machine learning*, 45:5–32, 2001.

[104] C Edward Rasmussen and Christopher KI Williams. Gaussian processes for machine learning cambridge. *MA: the MIT Press.[Google Scholar]*, 2006.

[105] Jerome Friedman. The elements of statistical learning: Data mining, inference, and prediction. *(No Title)*, 2009.

[106] Yann LeCun, Léon Bottou, Yoshua Bengio, and Patrick Haffner. Gradient-based learning applied to document recognition. *Proceedings of the IEEE*, 86(11):2278–2324, 2002.

[107] Sepp Hochreiter and Jürgen Schmidhuber. Long short-term memory. *Neural computation*, 9(8):1735–1780, 1997.

[108] Franco Scarselli, Marco Gori, Ah Chung Tsoi, Markus Hagenbuchner, and Gabriele Monfardini. The graph neural network model. *IEEE transactions on neural networks*, 20(1):61–80, 2008.

[109] Diederik P Kingma, Max Welling, et al. An introduction to variational autoencoders. *Foundations and Trends® in Machine Learning*, 12(4):307–392, 2019.

[110] Ian Goodfellow, Jean Pouget-Abadie, Mehdi Mirza, Bing Xu, David Warde-Farley, Sherjil Ozair, Aaron Courville, and Yoshua Bengio. Generative adversarial networks. *Communications of the ACM*, 63(11):139–144, 2020.

[111] Tian Xie, Xiang Fu, Octavian-Eugen Ganea, Regina Barzilay, and Tommi Jaakkola. Crystal diffusion variational autoencoder for periodic material generation. *arXiv preprint arXiv:2110.06197*, 2021.

[112] Dong C Liu and Jorge Nocedal. On the limited memory bfgs method for large scale optimization. *Mathematical programming*, 45(1):503–528, 1989.

[113] Simon Haykin. *Kalman filtering and neural networks*. John Wiley & Sons, 2004.

[114] Jorge J Moré. The levenberg-marquardt algorithm: implementation and theory. In *Numerical analysis: proceedings of the biennial Conference held at Dundee, June 28–July 1, 1977*, pages 105–116. Springer, 2006.

[115] Robert Hecht-Nielsen. Theory of the backpropagation neural network. In *Neural networks for perception*, pages 65–93. Elsevier, 1992.

[116] Martin Fodslette Møller. A scaled conjugate gradient algorithm for fast supervised learning. *Neural networks*, 6(4):525–533, 1993.

[117] Diederik P Kingma. Adam: A method for stochastic optimization. *arXiv preprint arXiv:1412.6980*, 2014.

[118] Bobby G Sumpter and Donald W Noid. Potential energy surfaces for macromolecules. a neural network technique. *Chemical physics letters*, 192(5-6):455–462, 1992.

[119] Jörg Behler. Neural network potential-energy surfaces in chemistry: a tool for large-scale simulations. *Physical Chemistry Chemical Physics*, 13(40):17930–17955, 2011.

[120] Jörg Behler. Constructing high-dimensional neural network potentials: a tutorial review. *International Journal of Quantum Chemistry*, 115(16):1032–1050, 2015.

[121] Nongnuch Artrith, Tobias Morawietz, and Jörg Behler. High-dimensional neural-network potentials for multicomponent systems: Applications to zinc oxide. *Physical Review B—Condensed Matter and Materials Physics*, 83(15):153101, 2011.

[122] Kristof T Schütt, Farhad Arbabzadah, Stefan Chmiela, Klaus R Müller, and Alexandre Tkatchenko. Quantum-chemical insights from deep tensor neural networks. *Nature communications*, 8(1):13890, 2017.

[123] Kristof T Schütt, Huziel E Sauceda, P-J Kindermans, Alexandre Tkatchenko, and K-R Müller. Schnet–a deep learning architecture for

molecules and materials. *The Journal of Chemical Physics*, 148(24), 2018.

[124] Linfeng Zhang, Jiequn Han, Han Wang, Roberto Car, and Weinan E. Deep potential molecular dynamics: a scalable model with the accuracy of quantum mechanics. *Physical review letters*, 120(14):143001, 2018.

[125] Justin Gilmer, Samuel S Schoenholz, Patrick F Riley, Oriol Vinyals, and George E Dahl. Neural message passing for quantum chemistry. In *International conference on machine learning*, pages 1263–1272. PMLR, 2017.

[126] Jie Zhou, Ganqu Cui, Shengding Hu, Zhengyan Zhang, Cheng Yang, Zhiyuan Liu, Lifeng Wang, Changcheng Li, and Maosong Sun. Graph neural networks: A review of methods and applications. *AI open*, 1:57–81, 2020.

[127] Thomas N Kipf and Max Welling. Semi-supervised classification with graph convolutional networks. *arXiv preprint arXiv:1609.02907*, 2016.

[128] Thomas Hofmann, Bernhard Schölkopf, and Alexander J Smola. A review of kernel methods in machine learning. *Mac-Planck-Institute Technical Report*, 156(1), 2006.

[129] Thomas Hofmann, Bernhard Schölkopf, and Alexander J Smola. Kernel methods in machine learning. 2008.

[130] Matthias Rupp, Alexandre Tkatchenko, Klaus-Robert Müller, and O Anatole Von Lilienfeld. Fast and accurate modeling of molecular atomization energies with machine learning. *Physical review letters*, 108(5):058301, 2012.

[131] Katja Hansen, Franziska Biegler, Raghunathan Ramakrishnan, Wiktor Pronobis, O Anatole Von Lilienfeld, Klaus-Robert Muller, and Alexandre Tkatchenko. Machine learning predictions of molecular

properties: Accurate many-body potentials and nonlocality in chemical space. *The journal of physical chemistry letters*, 6(12):2326–2331, 2015.

[132] Felix A Faber, Luke Hutchison, Bing Huang, Justin Gilmer, Samuel S Schoenholz, George E Dahl, Oriol Vinyals, Steven Kearnes, Patrick F Riley, and O Anatole Von Lilienfeld. Prediction errors of molecular machine learning models lower than hybrid dft error. *Journal of chemical theory and computation*, 13(11):5255–5264, 2017.

[133] Anders S Christensen, Lars A Bratholm, Felix A Faber, and O Anatole von Lilienfeld. Fchl revisited: Faster and more accurate quantum machine learning. *The Journal of chemical physics*, 152(4), 2020.

[134] Albert P Bartók, Risi Kondor, and Gábor Csányi. On representing chemical environments. *Physical Review B—Condensed Matter and Materials Physics*, 87(18):184115, 2013.

[135] Volker L Deringer, Albert P Bartók, Noam Bernstein, David M Wilkins, Michele Ceriotti, and Gábor Csányi. Gaussian process regression for materials and molecules. *Chemical Reviews*, 121(16):10073–10141, 2021.

[136] Tak-San Ho and Herschel Rabitz. A general method for constructing multidimensional molecular potential energy surfaces from ab initio calculations. *The Journal of chemical physics*, 104(7):2584–2597, 1996.

[137] Oliver T Unke and Markus Meuwly. Toolkit for the construction of reproducing kernel-based representations of data: Application to multidimensional potential energy surfaces. *Journal of chemical information and modeling*, 57(8):1923–1931, 2017.

[138] Albert P Bartók and Gábor Csányi. G aussian approximation potentials: A brief tutorial introduction. *International Journal of Quantum Chemistry*, 115(16):1051–1057, 2015.

[139] Michael A Collins. Molecular potential-energy surfaces for chemical reaction dynamics. *Theoretical Chemistry Accounts*, 108:313–324, 2002.

[140] Peter Lancaster and Kes Salkauskas. Surfaces generated by moving least squares methods. *Mathematics of computation*, 37(155):141–158, 1981.

[141] Reinhard Farwig. Multivariate interpolation of arbitrarily spaced data by moving least squares methods. *Journal of computational and applied mathematics*, 16(1):79–93, 1986.

[142] Jason D Bender, Sriram Doraiswamy, Donald G Truhlar, and Graham V Candler. Potential energy surface fitting by a statistically localized, permutationally invariant, local interpolating moving least squares method for the many-body potential: Method and application to n4. *The Journal of chemical physics*, 140(5), 2014.

[143] Bastiaan J Braams and Joel M Bowman. Permutationally invariant potential energy surfaces in high dimensionality. *International Reviews in Physical Chemistry*, 28(4):577–606, 2009.

[144] Florbela Pereira and João Aires-de Sousa. Machine learning for the prediction of molecular dipole moments obtained by density functional theory. *Journal of cheminformatics*, 10:1–11, 2018.

[145] Max Veit, David M Wilkins, Yang Yang, Robert A DiStasio, and Michele Ceriotti. Predicting molecular dipole moments by combining atomic partial charges and atomic dipoles. *The Journal of chemical physics*, 153(2), 2020.

[146] Xiangyue Liu, Gerard Meijer, and Jesús Pérez-Ríos. A data-driven approach to determine dipole moments of diatomic molecules. *Physical Chemistry Chemical Physics*, 22(42):24191–24200, 2020.

[147] Carsten G Staacke, Simon Wengert, Christian Kunkel, Gábor Csányi, Karsten Reuter, and Johannes T Margraf. Kernel charge equilibra-

tion: efficient and accurate prediction of molecular dipole moments with a machine-learning enhanced electron density model. *Machine Learning: Science and Technology*, 3(1):015032, 2022.

[148] David M Wilkins, Andrea Grisafi, Yang Yang, Ka Un Lao, Robert A DiStasio Jr, and Michele Ceriotti. Accurate molecular polarizabilities with coupled cluster theory and machine learning. *Proceedings of the National Academy of Sciences*, 116(9):3401–3406, 2019.

[149] Chaoqiang Feng, Jin Xi, Yaolong Zhang, Bin Jiang, and Yong Zhou. Accurate and interpretable dipole interaction model-based machine learning for molecular polarizability. *Journal of Chemical Theory and Computation*, 19(4):1207–1217, 2023.

[150] Tran Tuan-Anh and Robert Zalesny. Predictions of high-order electric properties of molecules: Can we benefit from machine learning? *ACS omega*, 5(10):5318–5325, 2020.

[151] Alan R Katritzky, Liliana Pacureanu, Dimitar Dobchev, and Mati Karelson. Qspr modeling of hyperpolarizabilities. *Journal of molecular modeling*, 13:951–963, 2007.

[152] Andrea Grisafi, David M Wilkins, Gábor Csányi, and Michele Ceriotti. Symmetry-adapted machine learning for tensorial properties of atomistic systems. *Physical review letters*, 120(3):036002, 2018.

[153] Andrea Grisafi, David M Wilkins, Michael J Willatt, and Michele Ceriotti. Atomic-scale representation and statistical learning of tensorial properties. In *Machine Learning in Chemistry: Data-Driven Algorithms, Learning Systems, and Predictions*, pages 1–21. ACS Publications, 2019.

[154] Anders S Christensen, Felix A Faber, and O Anatole Von Lilienfeld. Operators in quantum machine learning: Response properties in chemical space. *The Journal of chemical physics*, 150(6), 2019.

[155] Brandon Anderson, Truong Son Hy, and Risi Kondor. Cormorant: Covariant molecular neural networks. *Advances in neural information processing systems*, 32, 2019.

[156] Grace M Sommers, Marcos F Calegari Andrade, Linfeng Zhang, Han Wang, and Roberto Car. Raman spectrum and polarizability of liquid water from deep neural networks. *Physical Chemistry Chemical Physics*, 22(19):10592–10602, 2020.

[157] M Born and R Oppenheimer. Zur quantentheorie der molekeln. *Annalen der Physik*, 389(20):457–484, 1927.

[158] Seymour H Vosko, Leslie Wilk, and Marwan Nusair. Accurate spin-dependent electron liquid correlation energies for local spin density calculations: a critical analysis. *Canadian Journal of physics*, 58(8):1200–1211, 1980.

[159] John P Perdew and Yue Wang. Accurate and simple analytic representation of the electron-gas correlation energy. *Physical review B*, 45(23):13244, 1992.

[160] John P Perdew, Kieron Burke, and Matthias Ernzerhof. Generalized gradient approximation made simple. *Physical review letters*, 77(18):3865, 1996.

[161] Axel D Becke. Density-functional exchange-energy approximation with correct asymptotic behavior. *Physical review A*, 38(6):3098, 1988.

[162] Axel D Becke. Density-functional thermochemistry. i. the effect of the exchange-only gradient correction. *The Journal of chemical physics*, 96(3):2155–2160, 1992.

[163] Chengteh Lee, Weitao Yang, and Robert G Parr. Development of the colle-salvetti correlation-energy formula into a functional of the electron density. *Physical review B*, 37(2):785, 1988.

[164] John A Pople, Martin Head-Gordon, Douglas J Fox, Krishnan Raghavachari, and Larry A Curtiss. Gaussian-1 theory: A general procedure for prediction of molecular energies. *The Journal of Chemical Physics*, 90(10):5622–5629, 1989.

[165] Sigeru Huzinaga, Jan Andzelm, E Radzio-Andzelm, Y Sakai, H Tatewaki, and M Klobukowski. *Gaussian basis sets for molecular calculations*. Elsevier, 2012.

[166] Georg Kresse and Jürgen Hafner. Ab initio molecular dynamics for liquid metals. *Physical review B*, 47(1):558, 1993.

[167] Georg Kresse and Jürgen Hafner. Ab initio molecular-dynamics simulation of the liquid-metal–amorphous-semiconductor transition in germanium. *Physical Review B*, 49(20):14251, 1994.

[168] Georg Kresse and Jürgen Furthmüller. Efficiency of ab-initio total energy calculations for metals and semiconductors using a plane-wave basis set. *Computational materials science*, 6(1):15–50, 1996.

[169] Georg Kresse and Jürgen Furthmüller. Efficient iterative schemes for ab initio total-energy calculations using a plane-wave basis set. *Physical review B*, 54(16):11169, 1996.

[170] Peter E Blöchl. Projector augmented-wave method. *Physical review B*, 50(24):17953, 1994.

[171] P Jeffrey Hay and Willard R Wadt. Ab initio effective core potentials for molecular calculations. potentials for the transition metal atoms sc to hg. *The Journal of chemical physics*, 82(1):270–283, 1985.

[172] MJ Frisch. Gaussian 09, revision d. 01/gaussian, 2009.

[173] J Tersoff. New empirical model for the structural properties of silicon. *Physical review letters*, 56(6):632, 1986.

[174] Frank H Stillinger and Thomas A Weber. Computer simulation of local order in condensed phases of silicon. *Physical review B*, 31(8):5262, 1985.

[175] Adrian P Sutton, Mike W Finnis, David G Pettifor, and Y Ohta. The tight-binding bond model. *Journal of Physics C: Solid State Physics*, 21(1):35, 1988.

[176] CM Goringe, DR Bowler, and E Hernández. Tight-binding modelling of materials. *Reports on Progress in Physics*, 60(12):1447, 1997.

[177] Shweta Jindal, Siva Chiriki, and Satya S Bulusu. Spherical harmonics based descriptor for neural network potentials: Structure and dynamics of au147 nanocluster. *The Journal of chemical physics*, 146(20), 2017.

[178] David F Shanno. Conditioning of quasi-newton methods for function minimization. *Mathematics of computation*, 24(111):647–656, 1970.

[179] Ian Goodfellow. Deep learning, 2016.

[180] Tijmen Tieleman. Lecture 6.5-rmsprop: Divide the gradient by a running average of its recent magnitude. *COURSERA: Neural networks for machine learning*, 4(2):26, 2012.

[181] Adam Paszke, Sam Gross, Francisco Massa, Adam Lerer, James Bradbury, Gregory Chanan, Trevor Killeen, Zeming Lin, Natalia Gimelshein, Luca Antiga, et al. Pytorch: An imperative style, high-performance deep learning library. *Advances in neural information processing systems*, 32, 2019.

[182] Carl Edward Rasmussen. Gaussian processes in machine learning. In *Summer school on machine learning*, pages 63–71. Springer, 2003.

[183] Bernhard Schölkopf, Ralf Herbrich, and Alex J Smola. A generalized representer theorem. In *International conference on computational learning theory*, pages 416–426. Springer, 2001.

[184] Shweta Jindal and Satya S Bulusu. A transferable artificial neural network model for atomic forces in nanoparticles. *The Journal of Chemical Physics*, 149(19), 2018.

[185] Albert P Bartók, Mike C Payne, Risi Kondor, and Gábor Csányi. Gaussian approximation potentials: The accuracy of quantum mechanics, without the electrons. *Physical review letters*, 104(13):136403, 2010.

[186] Shweta Jindal and Satya S Bulusu. An algorithm to use higher order invariants for modelling potential energy surface of nanoclusters. *Chemical Physics Letters*, 693:152–158, 2018.

[187] Risi Kondor. A novel set of rotationally and translationally invariant features for images based on the non-commutative bispectrum. *arXiv preprint cs/0701127*, 2007.

[188] Ramakrishna Kakarala. The bispectrum as a source of phase-sensitive invariants for fourier descriptors: a group-theoretic approach. *Journal of Mathematical Imaging and Vision*, 44:341–353, 2012.

[189] YC Kim and EJ Powers. Digital bispectral analysis of self-excited fluctuation spectra. *Physics of Fluids*, 21(8):1452–1453, 1978.

[190] Hans C Andersen. Molecular dynamics simulations at constant pressure and/or temperature. *The Journal of chemical physics*, 72(4):2384–2393, 1980.

[191] Martin J Field, Paul A Bash, and Martin Karplus. A combined quantum mechanical and molecular mechanical potential for molecular dynamics simulations. *Journal of computational chemistry*, 11(6):700–733, 1990.

[192] Helmut Grubmüller, Helmut Heller, Andreas Windemuth, and Klaus Schulten. Generalized verlet algorithm for efficient molecular dynamics simulations with long-range interactions. *Molecular Simulation*, 6(1-3):121–142, 1991.

[193] Amyand David Buckingham. Permanent and induced molecular moments and long-range intermolecular forces. *Advances in chemical physics: Intermolecular forces*, pages 107–142, 1967.

[194] Ahmed AK Mohammed, Peter A Limacher, and Benoit Champagne. Finding optimal finite field strengths allowing for a maximum of precision in the calculation of polarizabilities and hyperpolarizabilities. *Journal of computational chemistry*, 34(17):1497–1507, 2013.

[195] J Kobus, D Moncrieff, and S Wilson. Comparison of the polarizabilities and hyperpolarizabilities obtained from finite basis set and finite difference hartree-fock calculations for diatomic molecules. *Journal of Physics B: Atomic, Molecular and Optical Physics*, 34(24):5127, 2001.

[196] Xavier Gonze and J-P Vigneron. Density-functional approach to nonlinear-response coefficients of solids. *Physical Review B*, 39(18):13120, 1989.

[197] Xavier Gonze. Adiabatic density-functional perturbation theory. *Physical Review A*, 52(2):1096, 1995.

[198] Manoj K Harbola and Arup Banerjee. Perturbation theory in terms of electron density. *Physics Letters A*, 222(5):315–323, 1996.

[199] G Kresse, J Furthmüller, and JJPRB Hafner. Theory of the crystal structures of selenium and tellurium: the effect of generalized-gradient corrections to the local-density approximation. *Physical Review B*, 50(18):13181, 1994.

[200] Diego Guedes-Sobrinho, Rafael LH Freire, Anderson S Chaves, and Juarez LF Da Silva. Ab initio investigation of the role of co adsorption on the physical properties of 55-atom ptco nanoalloys. *The Journal of Physical Chemistry C*, 121(49):27721–27732, 2017.

[201] Andrés Aguado and José M López. Identifying structural and energetic trends in isovalent core-shell nanoalloys as a function of compo-

sition and size mismatch. *The Journal of chemical physics*, 135(13), 2011.

[202] Giovanni Barcaro, Luca Sementa, and Alessandro Fortunelli. A grouping approach to homotop global optimization in alloy nanoparticles. *Physical Chemistry Chemical Physics*, 16(44):24256–24265, 2014.

[203] Richard FW Bader. A quantum theory of molecular structure and its applications. *Chemical Reviews*, 91(5):893–928, 1991.

[204] Tian Lu and Feiwu Chen. Multiwfn: A multifunctional wavefunction analyzer. *Journal of computational chemistry*, 33(5):580–592, 2012.

[205] Oscar Alan Sanders-Gutierrez, Analila Luna-Valenzuela, Alvaro Posada-Borbón, J Christian Schön, and Alvaro Posada-Amarillas. Molecular dynamics and dft study of 38-atom coinage metal clusters. *Computational Materials Science*, 201:110908, 2022.

[206] Wei Zhang, Shiyao Shan, Jin Luo, Adrian Fisher, Jian-Feng Chen, Chuan-Jian Zhong, Jiqin Zhu, and Daojian Cheng. Origin of enhanced activities for co oxidation and o2 reaction over composition-optimized pd50cu50 nanoalloy catalysts. *The Journal of Physical Chemistry C*, 121(20):11010–11020, 2017.

[207] Omar Z Sharaf and Mehmet F Orhan. An overview of fuel cell technology: Fundamentals and applications. *Renewable and sustainable energy reviews*, 32:810–853, 2014.

[208] Leonard Jean Moriau, Armin Hrnjić, Andraž Pavlišič, Ana Rebeka Kamšek, Urša Petek, Francisco Ruiz-Zepeda, Martin Šala, Luka Pavko, Vid Simon Šelih, Marjan Bele, et al. Resolving the nanoparticles' structure-property relationships at the atomic level: a study of pt-based electrocatalysts. *IScience*, 24(2), 2021.

[209] Tina ukić, Luka Pavko, Primož Jovanovič, Nik Maselj, Matija Gatalo, and Nejc Hodnik. Stability challenges of carbon-supported pt-

nanoalloys as fuel cell oxygen reduction reaction electrocatalysts. *Chemical Communications*, 58(100):13832–13854, 2022.

[210] Julius Jellinek. Nanoalloys: tuning properties and characteristics through size and composition. *Faraday discussions*, 138:11–35, 2008.

[211] Jing Lu, Kazuya Ishimura, and Shigeyoshi Sakaki. Theoretical insight into core–shell preference for bimetallic pt-m (m= ru, rh, os, and ir) cluster and its electronic structure. *The Journal of Physical Chemistry C*, 122(16):9081–9090, 2018.

[212] Dianyong Tang, Zhongzhu Chen, Jianping Hu, Guofeng Sun, Shenzhuang Lu, and Changwei Hu. Co oxidation catalyzed by silver nanoclusters: mechanism and effects of charge. *Physical Chemistry Chemical Physics*, 14(37):12829–12837, 2012.

[213] BJKN Hammer and Jens K Nørskov. Electronic factors determining the reactivity of metal surfaces. *Surface science*, 343(3):211–220, 1995.

[214] Guoxiang Zhao, Weiyin Yan, Zirui Wang, Yao Kang, Zuju Ma, Zhi-Gang Gu, Qiao-Hong Li, and Jian Zhang. Predict the polarizability and order of magnitude of second hyperpolarizability of molecules by machine learning. *The Journal of Physical Chemistry A*, 127(29):6109–6115, 2023.

[215] Mario G Zauchner, Stefano Dal Forno, Gábor Cśanyi, Andrew Horsfield, and Johannes Lischner. Predicting polarizabilities of silicon clusters using local chemical environments. *Machine Learning: Science and Technology*, 2(4):045029, 2021.

[216] Hao Li, Xifeng Liu, Shuangjun Yang, Tianqi Yi, Zhi Yang, and Wen Yuan. Prediction of polarizability and absolute permittivity values for hydrocarbon compounds using artificial neural networks. *International Journal of Electrochemical Science*, 9(7):3725–3735, 2014.

[217] Thomas B Blank and Steven D Brown. Adaptive, global, extended kalman filters for training feedforward neural networks. *Journal of chemometrics*, 8(6):391–407, 1994.

[218] James B Witkoskie and Douglas J Doren. Neural network models of potential energy surfaces: Prototypical examples. *Journal of chemical theory and computation*, 1(1):14–23, 2005.

[219] Christopher KI Williams and Carl Edward Rasmussen. *Gaussian processes for machine learning*, volume 2. MIT press Cambridge, MA, 2006.

[220] Fabian Pedregosa, Gaël Varoquaux, Alexandre Gramfort, Vincent Michel, Bertrand Thirion, Olivier Grisel, Mathieu Blondel, Peter Prettenhofer, Ron Weiss, Vincent Dubourg, et al. Scikit-learn: Machine learning in python. *the Journal of machine Learning research*, 12:2825–2830, 2011.